YILDIRIM BEYAZIT UNIVERSITY
GRADUATE SCHOOL OF NATURAL AND APPLIED SCIENCES

MODELLING AND DESIGN OF TERAHERTZ

PHOTOCONDUCTIVE ANTENNAS AND PHOTOMIXERS

M.Sc. Thesis by

Kazım DEMİR

Department of Electrical and Electronics Engineering

January, 2016
ANKARA

MODELLING AND DESIGN OF TERAHERTZ PHOTOCONDUCTIVE ANTENNAS AND PHOTOMIXERS

**A Thesis Submitted to
the Graduate School of Natural and Applied Sciences of Yıldırım Beyazıt
University
In Partial Fulfillment of the Requirements for the Degree of Master of Science
in Electrical and Electronic Engineering, Department of Electrical and
Electronics Engineering**

by

Kazım DEMİR

January, 2016

ANKARA

M.Sc. THESIS EXAMINATION RESULT FORM

We have read the thesis entitled "**MODELLING AND DESIGN OF TERAHERTZ PHOTOCONDUCTIVE ANTENNAS AND PHOTOMIXERS**" completed by Kazım DEMİR under supervision of **Assist. Prof. Dr. Mehmet ÜNLÜ** and we certify that in our opinion it is fully adequate, in scope and in quality, as a thesis for the degree of Master of Science.

....

Assist. Prof. Dr. Mehmet ÜNLÜ

(Supervisor)

....

Assoc. Prof. Dr. Asaf Behzat ŞAHİN Assoc. Prof. Dr. Hakan ALTAN

(Jury Member)   (Jury Member)

....

Prof. Dr. Fatih V. ÇELEBİ

(Director)

Graduate School of Natural and Applied Sciences

ETHICAL DECLERATION

I have prepared this dissertation study in accordance with the Rules of Writing Thesis of Yıldırım Beyazıt University of Science and Technology Institute;

- Data I have presented in the thesis, information and documents that I obtained in the framework of academic and ethical rules,

- All information, documentation, assessment and results that I presented in accordance with scientific ethics and morals,

- I have gave references all the works that I were benefited in this dissertation by appropriate reference,

- I would not make any changes in the data that I were used,

- The work presented in this dissertation I would agree that the original,

I state, in the contrary case I declare that I accept the all rights losses that may arise against me.

MODELLING AND DESIGN OF TERAHERTZ PHOTOCONDUCTIVE ANTENNAS AND PHOTOMIXERS

ABSTRACT

DEMİR, Kazım

M.Sc., Department of Electrical and Electronics Engineering

Supervisor: Assoc. Prof. Dr. Mehmet ÜNLÜ

January 2016, 134 pages

In this thesis, the terahertz photoconductive antennas and photomixers have been modelled and designed for different antenna geometries.

Firstly, the equation for the conductance of the THz antenna gap region is derived and transient behaviour of the antenna gap conductance is observed for varying parameters of the antenna system. It is observed that the transient behaviour of the antenna gap conductance is dependent on the properties of the LT-GaAs semiconductor substrate, gap dimensions of the deposited antenna electrodes, and the properties of the laser beam which is incident onto the antenna gap surface between the arms of the deposited antenna. Due to the time varying conductance under a constant potential difference, a transient photocurrent is obtained through the electrodes of the antenna.

Secondly, an equivalent circuit model is used to obtain the temporal behaviour of the antenna gap voltage and the photocurrent. For the solution of the antenna gap voltage equation, a numerical solution technique is used to solve the differential equation which is called Runge Kutta Method.

Thirdly, the design of simple dipole antennas and spiral antenna are implemented on LT-GaAs substrate. While two different dipole antennas are designed to make a maximum raditation at 340 GHz and 550 GHz, the spiral antenna is designed to operate at 420 GHz.

Finally, reconfigurable THz antennas are designed. THz reconfigurable antenna operation is based on changing the resonance frequency of the antenna by

mechanically changing the antenna length with the help of MEMS switches. Two types of antenna shapes were used as reconfigurable antenna. First reconfigurable antenna type is a folded dipole antenna which was designed to operate at three different frequencies which are 200GHz, 450GHz, and 780 GHz. For the proper operation of the folded dipole antenna, design of a metal-insultor-metal capacitor was needed to isolate the arms of the DC bias lines. The second designed reconfigurable antenna type is a simple dipole which is operating at 290 GHz, and 550 GHz. It is observed that the use of folded dipoles are more advantageous due to their high antenna input resistances when compared to simple dipoles.

FOTOKARIŞTIRICILARIN VE TERAHERTZ FOTOİLETKEN ANTENLERİN MODELLENMESİ VE TASARIMI

ÖZET

DEMİR, Kazım

Yüksek Lisans Tezi, Elektrik ve Elektronik Mühendisliği Bölümü

Tez Yöneticisi: Yard. Doç. Dr. Mehmet ÜNLÜ

Ocak 2016, 134 sayfa

Bu yüksek lisans tezinde, lazer darbesiyle uyarılan fotoiletken antenlerin ve fotokarıştırıcıların farklı anten geometrileri için modellenmesi ve tasarımı gerçekleştirilmiştir.

İlk olarak, THz anten boşluğundaki iletkenlik değişimini ifade eden bir denklem elde edilmiş ve farklı parametrelere bağlı olarak nasıl bir değişiklik gözterdiği gözlemlenmiştir. Anten boşluğunda zamana bağlı olarak değişen iletkenlik, LT-GaAs yarıiletkeninin özelliklerine, yarıiletken üzerine serilmiş anten elektrotlarının arasındaki boşluğun ölçülerine ve anten boşluğu üzerine düşmekte olan ışınının özelliklerine bağlı olarak değişmektedir. Sonuç olarak, anten elektrotlarına sabit bir voltaj kaynağı uygulandığında, zamana bağlı olarak değişen bu iletkenlikten dolayı anten elektrotları üzerinde zamana bağlı olarak değişen bir fotoakım elde edilir.

İkinci olarak, anten boşluğununda meydana gelen voltaj düşümünün ve ortaya çıkan fotoakımın zamana bağlı olarak değişimini modelleyen bir eşdeğer devre modeli analiz edilmiştir. Devre analizi sonucu elde edilen anten boşluğu voltajı diferansiyel denkleminin çözümü için nümerik yöntemlere ihtiyaç duyulmuş ve Runge Kutta Metodu ile anten voltajı numerik olarak çözümlenmiştir.

Üçüncü olarak, basit çift kutuplu antenler için ve spiral antenler için LT-GaAs pul üzerine THz antenler tasarlanmıştır. 340 GHz ve 550 GHz'te maksimum güç yayılımı yapan iki çift kutuplu anten, 420 GHz'te maksimum yayılım yapan bir spiral anten tasarımı gerçekleştirilmiştir.

Son olarak, farklı frekanslara ayarlanabilen anten tasarımları gerçekleştirilmiştir. Frekansı ayarlanabilir antenlerin çalışması, MEMS anahtarlar yardımıyla anten boyunun kademeli olarak değiştirilmesine ve böylece maksimum yayılım yaptığı frekansın ayarlanması prensibine dayanmaktadır. Bu amaçla, ilk olarak üç farklı frekansa ayarlanabilen katlı çift kutuplu anten tasarımı gerçekleştirilmiştir. Bu frekanslar 200GHz, 450GHz ve 780 GHz'dir. Katlı çift kutuplu anten kollarının birleştiği noktadaki doğru akım besleme hatlarının kollarını birbirlerinden doğru akım olarak isole edebilmek için kolların antenna bağlı olduğu iki hat arasındaki anten üzerine metal-yalıtkan-metal kapasitör eklenilmesine ihtiyaç duyulmuştur. Frekansı ayarlanabilir olarak tasarlanan ikinci tip anten basit dipol antendir. Dipol anten 290 GHz ve 550 GHz olmak üzere iki ayrı frekansa ayarlanabilir şekilde tasarlanmıştır. Katlı dipol antenlerin giriş dirençlerinin dipol antenlere göre daha yüksek olmasından dolayı çok daha verimli oldukları gözlemlenmiştir.

Anahtar kelimeler: Foto-iletken Anten, Lazer Darbeli Uyarı, Foto-karıştırıcı, Frekansı Ayarlanabilir Anten, Anten Besleme Hattı.

ACKNOWLEDGMENTS

CONTENTS

LIST OF TABLES

LIST OF FIGURES

CHAPTER 1

INTRODUCTION

1.1 The Terahertz Spectrum and Terahertz Wave Generation

Terahertz (THz) waves are described by the electromagnetic spectrum in the frequency range 300 GHz-10 THz with wavelengts between 1 mm-30μm. Terahertz waves lie at the far end of the infrared frequency band, just before the start of the microwave frequency band as shown in Figure 1.1.
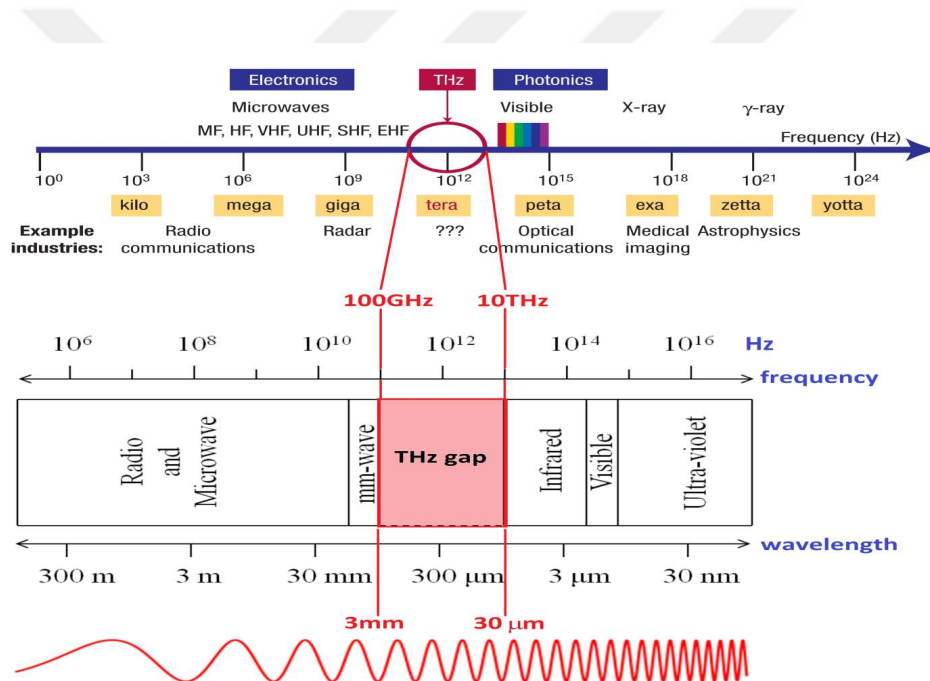
Figure 1.1 Schematic diagram of electromagnetic spectrum.

THz frequency band was one of the least explored region of the electromagnetic spectrum because of the absence of efficient THz signal generation sources and detectors.

Nowadays, THz frequency band attracts a lot of attention due to the new THz generation techniques was developed. One of the most commonly used sources for the THz generation is photoconductive antennas.

A photoconductive antenna is composed of three main parts:

- First part is a photoconductive material which is needed as the source of free carriers.
- Second part is a voltage biased antenna which should be deposited on the photoconductive substrate as the radiative element.
- Third part is a laser source which is used to release free carriers by the illumination of the gap region where the photoconductive material and antenna metallic part meets (antenna gap region).

Incident laser power causes very fast changing electric field on antenna gap region which causes rapidly moving free carriers to relese in the material.

There are two types of THz generation depending on the type of optical source [1]:

- THz photoconductive antennas in laser pulsed systems
- THz photomixer antennas in CW systems

In THz laser pulsed systems, laser pulses at a specific period and duration are hit onto the ground of the GaAs semiconductor substrate, and give rise to the optically induced photo-carriers in the photoconductive gap. As a result of the induced current pulses, THz electric pulses are radiated into the free space as EM waves. Ultrashort properties of the radiated electric field pulses lead to broadband frequency response

In CW systems, two monochromatic laser sources with slightly different optical frequencies (the difference is in the range of THz) are hit onto the substrate and a continuously changing THz radiation is obtained. Almost sinusoidal change of the radiated electric filed leads to a narrowband frequency response.

1.2 Research Motivations and Objectives

The main objectives of this research are as follows:

- To undertand the phenomena of photoconduction by modelling the parameters of the laser source, LT-GaAs layer, and the antenna geometry.
- To develop a methodology to design a photoconductive antenna at any desired operating frequency.

1.3 Thesis Overview

This research is organized as follows. A brief review of THz technology and CW THz photomixer sources with particular emphasis on photomixing theory and concept as well as important factors such as antenna and bias lines in the photomixer performance are presented in Chapter 1.

Chapter 2 will discuss a computational simulation method, such as High Frequency Structure Simulator (HFSS), to achieve a best result when simulating such a photomixer antenna. The effects of airbox size, port meshing, boundary condition, and choosing the proper size of a substrate will be discussed.

In Chapter 3, the characterization of bias lines will be given. Design parameters for each of bias lines will be given. Then, the bias lines will be treated as two port networks and the numerical studies will be carried out. Since the two-port network results of bias lines indicates the isolation between DC bias pads and antenna, the possible effects of each bias line on photomixer antennas will be discussed.

In Chapter 4, the design parameters of antennas that will be used for testing structures of bias lines will be discussed, and then different kind of planar antennas will be designed. The performance of antennas with each bias line will be compared in a perspective of radiation pattern and input impedance of antenna.

Finally, Chapter 5 concludes this research and suggests the future directions.

CHAPTER 2

THEORETICAL ANALYSIS AND MODELLING OF TERAHERTZ PHOTOCONDUCTIVE ANTENNAS AND PHOTOMIXERS

2.1   Introduction

The photoconductive antennas are used to generate THz signals by using femtosecond laser sources that create changes in the conduction of semiconductor materials where laser pulses are incident on. Due to this conductance change under dc biased voltage, a time varying current source is obtained at the gap region of planar antenna deposited on the substrate material. In this chapter, we will theoretically investigate the photoconductive antennas and model the effects of different parameters on the antenna conductance change and the output power. The modelling steps, that we will be following during this chapter is summarized in Figure 2.1.
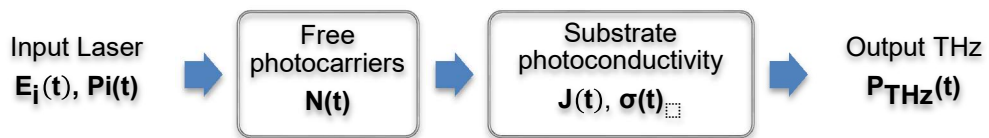
Figure 2.1 Modelling steps of photoconductive antenna.

A simplest equivalent circuit model for a photoconductive antenna for both pulsed and continuous wave excited system is shown in Figure 2.2.
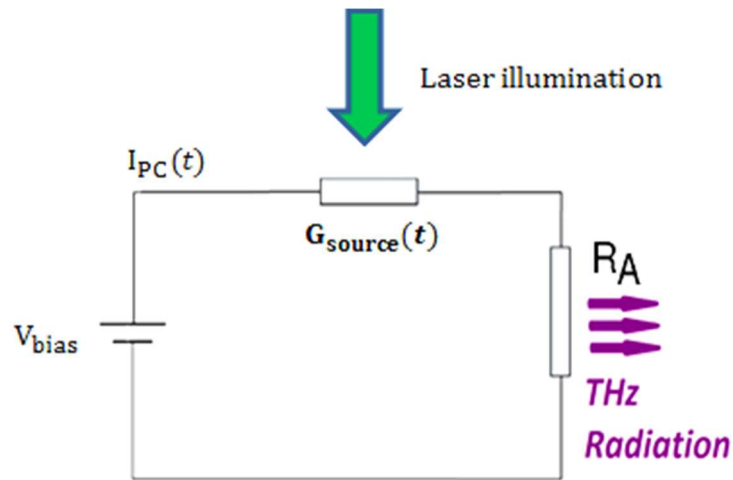
Figure 2.2 Equivalent circuit model for a photoconductive antenna.

In this model, $G_{source}(t)$ is the time-varying conductance of the antenna gap under laser illumination, $V_{bias}(t)$ is the DC voltage source applied between the antenna electrodes to move the free charges through the antenna metal parts, $I_{PC}(t)$ is the photoconductive current flowing through the gap as a result of applied voltage, R_A is the equivalent input resistance of the antenna deposited on the GaAs substrate. Values of antenna resistance, R_A does not change with time or frequency.

2.2 Modelling of a Terahertz Photoconductive Antennas in Pulsed Excitation System

The very first stage of a THz photoconductive antenna system is a laser excitation system which is responsible for being the high frequency energy source of a THz antenna. For a laser source to excite a single carrier through the energy gap of a photoconductive material, a photon should have a larger energy than the energy gap of the semiconductor. Generally, low-temperature-grown-GaAs is used as the photoconductive material due to its high mobility and short carrier lifetime. For LT-GaAs material used for photoconduction process, the incident photons should have energy at least 1.42 eV of band-gap energy in LT-GaAs layer. This much of energy corresponds to a photon whose wavelength is less than 867 nm. To better understand this phenomena, we need to understand the conduction process of carriers under

5

incident photons. Schematic view of THz photoconductive antenna with Gaussian pulsed model is in Figure 2.3. W and L are the length and width of the antenna gap, $t_{LT-GaAs}$ is the thickness of the LT-GaAs active layer that will be used for the modelling.

<div align="center">(a)   (b)</div>
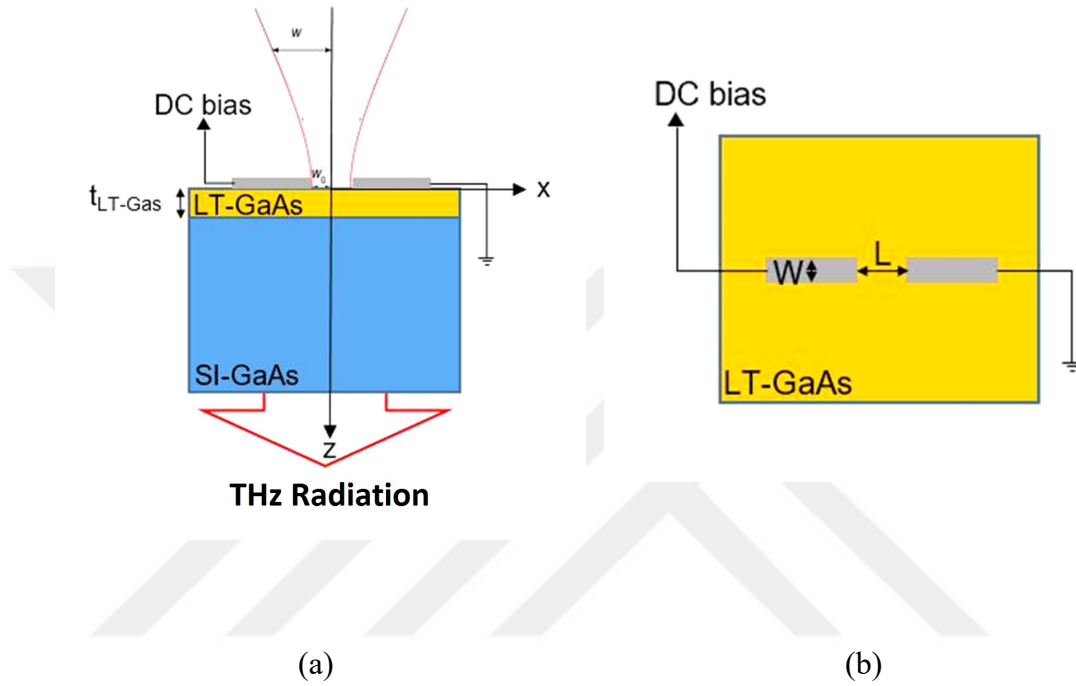
Figure 2.3 The basic schematic of a THz photoconductive antenna. (a) Side view. (b) Top view.

2.3 Modelling of the Laser Electric Field with Gauss Beam Model

Since the size of the wavelength (882μm in air) is comparable to the size of the optical components (300-500 μm for antenna structure), the diffraction effects become significant. So, the electric field distribution of the laser pulse is assumed to obey quasi optical approximation. The electric field at any point along the axis of propagation is [1]:

$$E_L(r, z) = \left(\frac{w_0}{w}\right) \exp\left(-\frac{r_1^2}{w_0^2} - jkz - \frac{j\pi r_1^2}{D\lambda} + j\Phi_0\right) \qquad \textbf{(2.1)}$$

$$D = z + \frac{1}{z}\left(\frac{\pi w_0^2}{\lambda}\right)^2 \qquad \textbf{(2.2)}$$

$$\Phi_0 = \tan^{-1}\left(\frac{\lambda z}{\pi w_0^2}\right) \qquad \textbf{(2.3)}$$

where

r_1	=	perpendicular distance from the z axis ($r_1 = w_0$)
w_0	=	beam waist (beam radius at z=0) on the gap
w	=	beam radius at any distance z
k	=	propagation constant
D	=	radius of curvature
Φ_0	=	Gaussian beam phase shift

Also, to include the time dependency of electric field on the laser pulse duration,τ_l, Eqn.(1) is modified as [1]:

$$E_L(r,t) = E_0 \exp\left(-\frac{r^2}{w_0^2}\right)\exp\left(-\frac{t^2}{\tau_l^2}\right)$$

$$\textbf{(2.4)}$$

$$= E_0 e^{-1}\exp(-\frac{t^2}{\tau_l^2}) \quad \text{on the gap surface with } \mathbf{r} = \mathbf{w_0}$$

For a single laser beam, the input optical pulse intensity can be calculated from the instantaneous power density vector (Poynting vector) as [2]:

$$\vec{P}_L(r,t) = \vec{E}(r,t)\text{x}\vec{H}(r,t) = \hat{a}_z\left[\frac{1}{\eta_0}E_0(r,t)^2\right] = \hat{a}_z\frac{E_0^2}{\eta_0}e^{-2}e^{-\frac{2t^2}{\tau_l^2}} \qquad \textbf{(2.5)}$$

Here we assumed the electric field is polarized in the x-direction, and magnetic field is polarized in the y-direction. So, the resulting power flow is in the z-direction. We can find the factor E_0 as:

$$E_0 = \sqrt{P_L \eta_0 e^2} \qquad\qquad\qquad (2.6)$$

Table 2.1 shows the E_0 factor that determines the amplitude of the laser beam, and the maximum value of the electric field which is incident onto the substrate for three different laser powers. Here, it is assumed that there is no loss of laser power between the laser source and the antenna.

Table 2.1 Values of the constant E_0 and maximum electric field density for the laser source.

Laser output power	E_0	Maximum electric field density of the laser wgixh is incident onto the antenna gap ($E_0 e^{-1}$), V/m
1W	52.78	19.42
500mW	37.32	13.73
250mW	26.39	9.7
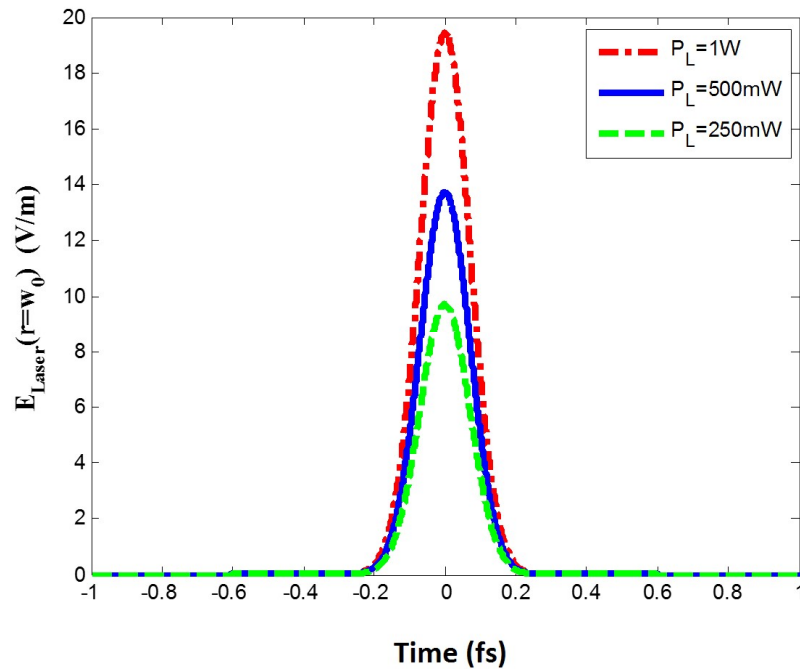
Figure 2.4 Modified Gauss laser electric field for three different laser output power levels.

By considering the optical reflection coefficient, R, at the air/LT-GaAs interface, we can write the transmitted optical power density by the substrate as:

$$\vec{P}_A = \hat{a}_z \frac{E_0^2}{\eta_0} (1 - R) \exp\left(-\frac{2r^2}{w_0^2}\right) \exp\left(-\frac{2t^2}{\tau_l^2}\right) \tag{2.7}$$

where

$$\eta_0 \quad = \quad \text{intrinsic impedance of free space}$$
$$R \quad = \quad \text{optical power reflection coefficient}$$

$$R_\perp = R_{TE} = \frac{\eta_{GaAs} \cos(\theta_i) - \eta_{air} \cos(\theta_t)}{\eta_{GaAs} \cos(\theta_i) + \eta_{air} \cos(\theta_t)} \quad \text{(a)}$$

$$R_{||} = R_{TM} = \frac{-\eta_{air} \cos(\theta_i) - \eta_{GaAs} \cos(\theta_t)}{\eta_{GaAs} \cos(\theta_t) + \eta_{air} \cos(\theta_i)} \quad \text{(b)} \tag{2.8}$$

2.4 Modelling of the Charge Density

When the laser beam with energy value greater than the bandgap energy of LT-Gas hits to the photoconductive surface (hv > 1.42eV / λ_L < 867nm), free electron-hole pairs are generated in the material. For simplicity we neglect the minor charge contribution from the holes since the effective mass of the hole is much greater than that of the electron in GaAs. The time dependent behavior of the carrier density is given by [3]:

$$\frac{dn(t)}{dt} = -\frac{n(t)}{\tau_c} + g(t) \tag{2.9}$$

where

$$\tau_c \quad = \quad \text{trapping time}$$
$$g(t) \quad = \quad \text{generation of free carriers by the laser pulse [1]}$$

The generated free carriers by the laser pulse is:

$$g(t) = \frac{\alpha}{hf_L} P_A(r, t) \tag{2.10}$$

where

$$hf_L \quad = \quad \text{photon energy}$$

$$\alpha \quad = \quad \text{attenuation constant of free carriers from substrate surface}$$
$$\text{into the z-direction}$$

Inserting the expression for $P_A(t)$ into the expression for $g(t)$ yields:

$$g(t) = \frac{\alpha}{hf_L} \frac{E_0^2}{\eta_0} (1 - R) \exp\left(-\frac{2r^2}{w_0^2}\right) \exp\left(-\frac{2t^2}{\tau_l^2}\right) \tag{2.11}$$

Substituting the current form of $g(t)$ into differential equation and solving for $n(t)$ gives a solution as[1]:

$$n(t) = C \frac{\alpha E_0^2}{\eta_0 hf_l} (1 - R) \exp\left(-\frac{2r^2}{w_0^2}\right)$$
$$e^{-t/\tau_C} \frac{\sqrt{2\pi}}{4} e^{\frac{\tau_L^2}{8\tau_C^2}} \tau_L \left(\text{erf}\left(\frac{\sqrt{2}}{\tau_L} t - \frac{\sqrt{2}\tau_L}{4\tau_C}\right) + 1\right) \tag{2.12}$$

where

$$\text{erf}(x) \quad = \quad \int_0^x e^{-t^2} dt$$
$$C \quad = \quad \text{Arbitrary constant}$$

Here, there are infinitely many differential solutions for $n(t)$, one for each choice of the "arbitrary" constant C. It alows us to use additional information to select from among all these solutions a particular one that fits the situation under study. In our

case, we should assign C to such a value that the initial conditions will match with the experimental results. In [3], it is reported that the source resistance for a pulsed excitation is in the range of some tens of ohms. So first, we need to find an expression for the source resistance for a pulsed excited dipole antenna, and then calculate the value of **C** by applying an appropriate initial value condition.

The current density in a semiconductor material is by [4]:

$$J(t) = \big(n(t)\mu_n + p(t)\mu_p\big)qE(t) = \sigma(t)E(t)$$
$$\approx (n\mu_n)qE(t)$$

(2.13)

where

$n(t)$	=	Time-dependent magnitude of free electron concentration
$p(t)$	=	Time-dependent magnitude of hole electron concentration

Since the effective mass of the hole is much higher than the effective mass of the electron, mobility of electrons is much higher than that of the holes, $\mu_e \gg \mu_h$, s we neglect the minor conductivity contribution from the holes in LT-GaAs. The approximated time dependent conductivity of the photoconductive material at the substrate surface [4] is:

$$\sigma(t) = \big(n(t)\mu_n + p(t)\mu_p\big)q \approx n(t)\mu_n q$$

(2.14)

However, the conductivity of $\sigma(t)$ shows space dependence as we go into the 1 μm thick LT-GaAs layer. Hence, $\sigma(t)$ was re-modeled as a function that exponentially decays with an attenuation of α in the z direction as [1]:

$$\sigma(z,t) = \sigma(t)e^{-\alpha z}$$

(2.15)

2.5 Modelling of the LT-GaAs Conductivity Change With Respect to Time

If the conductivity had no space dependence in z the direction, we could reach the gap conductance simply by using $G_s(t) = \sigma(t)\frac{Wt_{GaAs}}{L}$. However, we need to integrate the conductivity over the volume that is described by the antenna gap surface and the active layer thickness [5] which is shown in Figure 2.5.

$$
\begin{aligned}
G_s(t) &= \int_0^{t_{LT-GaAs}} \sigma(z,t)e^{-\alpha z}\frac{Wt_{GaAs}}{L}dz \\
&= \frac{Wt_{GaAs}}{L\alpha}\sigma(z)(1 - e^{-\alpha t_{LT-Ga}}) \\
&= \frac{Wt_{GaAs}}{L\alpha}n(t)\mu_n q(1 - e^{-\alpha t_{LT-GaAs}})
\end{aligned}
\tag{2.16}
$$

Here, it is assumed that the Gaussian beam radius ($r_1 = w_0$ at he surface) uniformly covers the whole gap area and all photo-carriers are generated in the volume determined by the depth of 1 μm thick LT-GaAs layer and the area of of dimensions W, and L as shown in Figure 2.5.
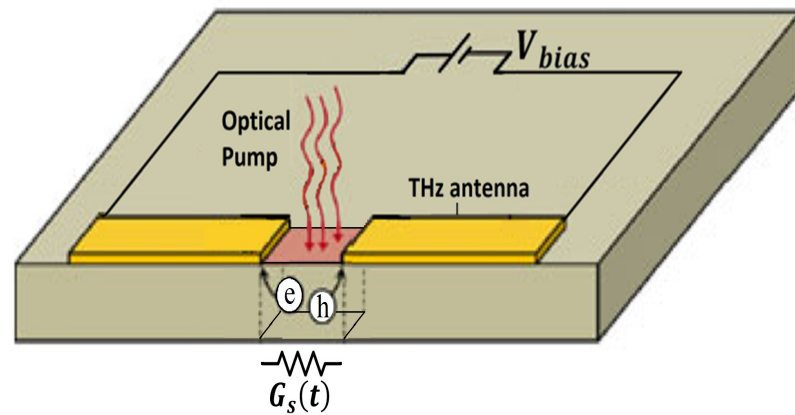
Figure 2.5 Geometrical parameters for the gap geometry of a photoconductive antenna.

Using (2.12) and (2.16), we obtain the source conductance $G_s(t)$ as:

$$G_s(t) = \frac{Wt_{GaAs}}{L\alpha}\sigma(z,t)(1 - e^{-\alpha t_{LT-GaAs}})$$

$$= \frac{Wt_{GaAs}}{L\alpha}n(t)\mu_n q(1 - e^{-\alpha t_{LT-GaAs}})$$

$$= \frac{C\sqrt{2\pi}\, t_{LT-GaAs}Wq\tau_L\mu_n}{(4L\eta_0 f_L h)}e^{\left(-\frac{t}{tC}\right)}e^{\left(\frac{\tau_L^2}{8\tau_C^2}\right)}e^{-\frac{(2r^2)}{w0^2}}e^{-\alpha t_{GAs}} \qquad \textbf{(2.17)}$$

$$\left(\text{erf}\left(\frac{\sqrt{2}t}{\tau_L} - \frac{(\sqrt{2}\tau_L)}{4\tau_C}\right) + 1\right)(R - 1)(1 - e^{t_{LT-GaAs}\,\alpha}))$$

where the typical values for the parameters for a THz system are listed in Table 2.2.

Table 2.2 Typical values for a THz system

Notation		Value	Parameter	
τ_L	=	20fs – 100 fs	Laser pulse duration	Laser
P_L	=	1 W	Laser power	
f_{REP}	=	80MHz – 120 MHz	Laser pulse repetition rate as depicted in Figure 2.6.	
f_L / λ_L	=	375 THz / (800 nm)	Laser frequency	
W	=	10 μm	Gap width	Antenna
L	=	10 μm	Gap length (along the antenna)	
$t_{LT-GaAs}$	=	1.3 μm	LT-GaAs layer thickness	

Table 2.3 *Continued*

τ_C	=	1 ps	Carrier lifetime	
μ_n	=	$1000 \frac{cm^2}{V.s}$	Electron mobility	PC Material
α	=	$6000 cm^{-1}$	Absorbtion coefficient for LT-GaAs	

According to the experimental results obtained from [6], 2.4 mA of photocurrent value was measured under a potential difference of 38 volts being applied to the arms of the dipole antenna deposited on a LT-GaAs substrate. They have used a laser pulse with a repetition time period of $T_{REP} = 12.5$ ns (1/80 MHz), and assumed a rectangular current pulse of 2ps width as shown in Figure 2.6. Finally, they have estimated a source resistance of 2.53 Ω by using the following approximate formula:

$$R_{s,sqaure} = R_{av} * \left(\frac{T_{current}}{T_{REP}} \right)$$
$$= \left(\frac{V_{bias}}{I_{PC,measured}} \right) * \left(\frac{T_{current}}{T_{REP}} \right)$$

(2.18)

(a)

(b)
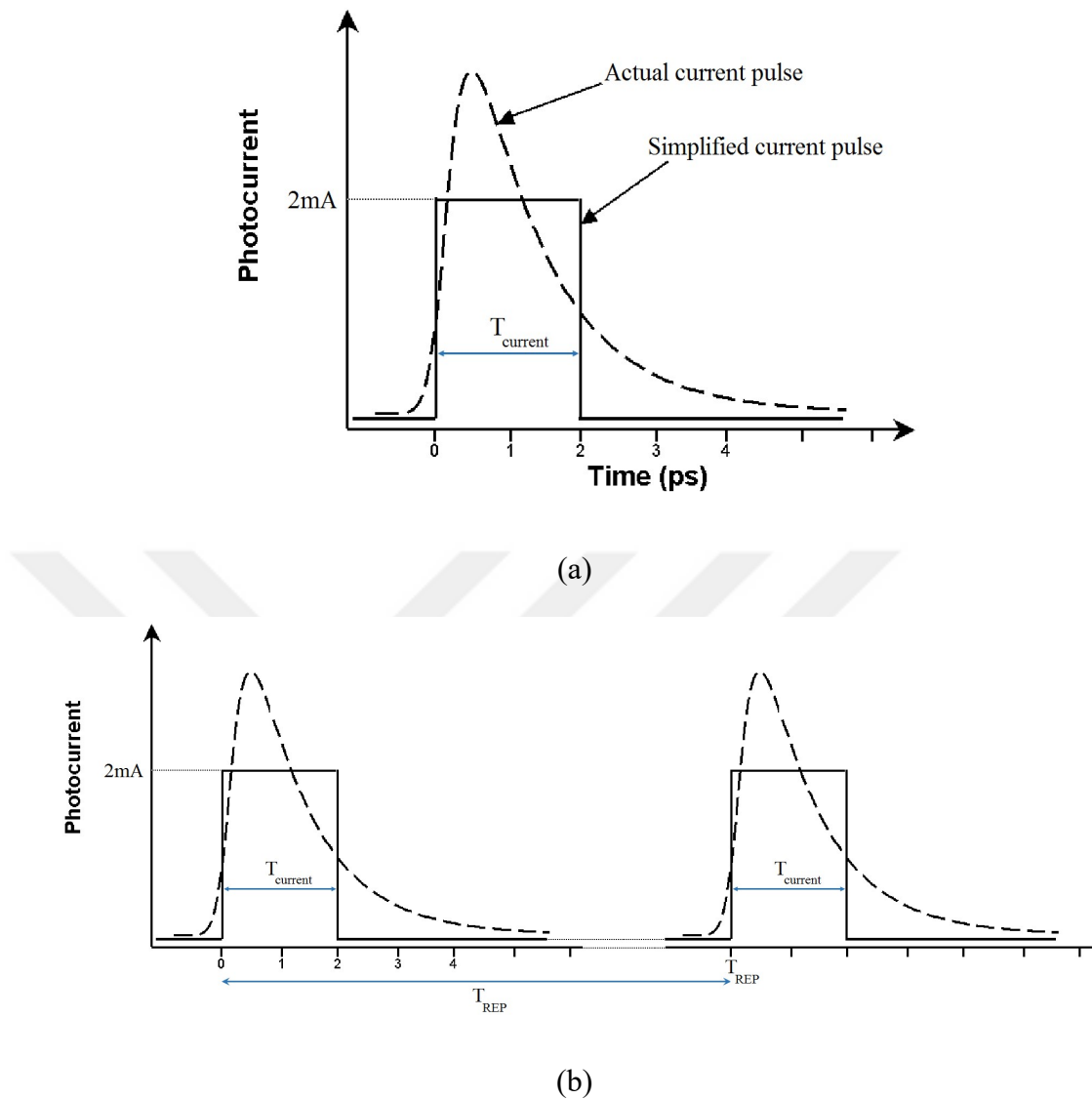
Figure 2.6 (a) Actual and simplified current pulses [6]. (b) Consecutive pulses with a laser pulse perios of $T_{REP} = 1/f_{REp}$

In a pulsed excited system, a resistance value is obtained as a result of the calculation $V_{bias}/I_{PC, measured}$. This resistance value gives a resistance in which the ON and OFF durations are taken into account. Due to the reason that the OFF time (12.5ns) is much larger than the ON time (2ps), this calculated average resistance is expected to be much larger than the instantaneous resistance at the antenna gap.

We can obtain a waveform which represents a more realistic response instead of a square wave approximation. The expected waveform can be profiled as follows:

- The photocurrent continuous to increase up to its peak value as the laser pulse is also increasing its amplitude up to the peak.
- After the moment that the laser pulse starts to decay, the expected photocurrent also decays due to the fact that the generated charges are grapped by the deficiencies located in the LT-GaAs layer on the antenna gap.

The maximum conductivity value which is calculated by square wave approximation is $0.4\ \Omega^{-1}$ $(1/2.53\Omega)$. If the value of C in (17) is adjusted to give a maximum resistance value of 2.5Ω, the obtained conductance change with time can be observed in Figure 2.7 with the parameter values are chosen as in Table 2.2.
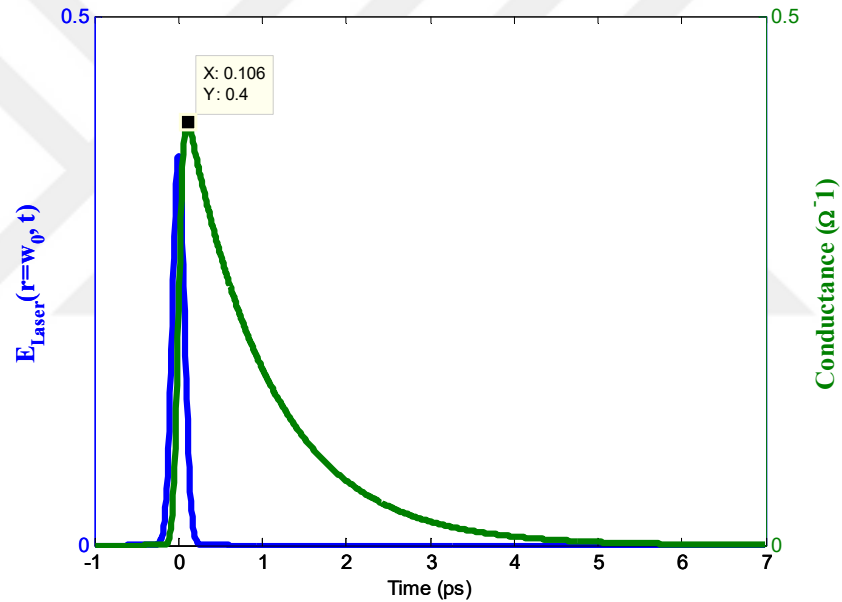
Figure 2.7 Time dependent behaviour of the incident E-field of the laser pulse and the conductance change with the applied field.
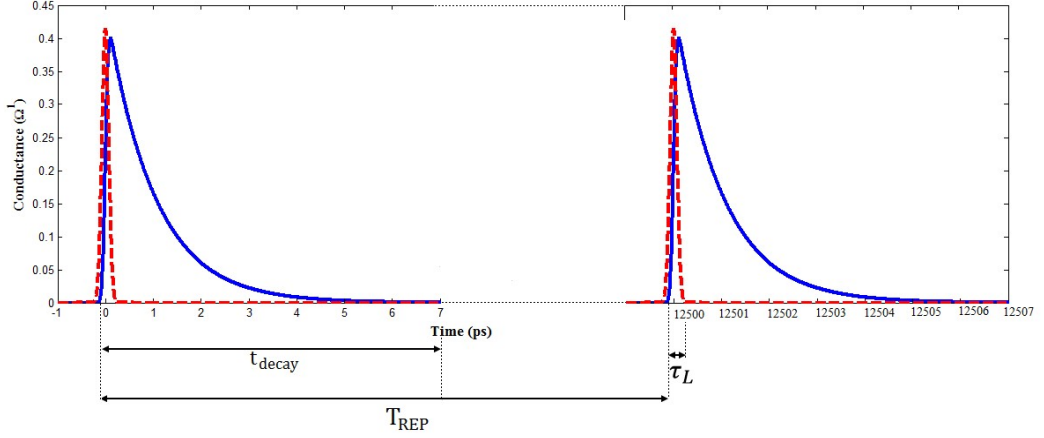
Figure 2.8 Two consecutive laser pulses and the resulting conductance change at the antenna gap.

$$(\tau_L = 0.1 \text{ ps}, \tau_C = 1\text{ps}, \quad t_{decay}=7\text{ps}, \quad T_{REP} = \frac{1}{f_{REP}} = 12500\text{ps})$$

Here, the calculated value of average resistance $R_{av} = V_{bias}/I_{PC,measured}$ gives the average value of the resistance, taking on and off times for pulse excitations into account. It is expected that the gap conductance makes a peak at the instant of the laser pulse incident onto gap and increases the number of free carriers to its peak number. So, we need a way to obtain instantaneous peak value of conductance from the measured average source resistance. This can be accomplished by the following equality:

$$G_{s,measured} = \vec{G}_s$$
$$\frac{I_{PC,measured}}{V_{bias}} = f_{REP} \int_0^{T_{REP}} G_S(t)dt \qquad (2.19)$$

where $\vec{G}_s$ is the average value for the source conductance over the laser on and off time period, $1/f_{REP,}$ is given by:

$$\vec{G}_s = f_{REP} \int_0^{T_{REP}} G_S(t)dt \qquad (2.20)$$

17

For the calculation of the above integral equations which are given in (2.19) and (2.20), numerical integration techniques were used for the calculation of the area under the integrated curve as depicted in Figure 2.9.
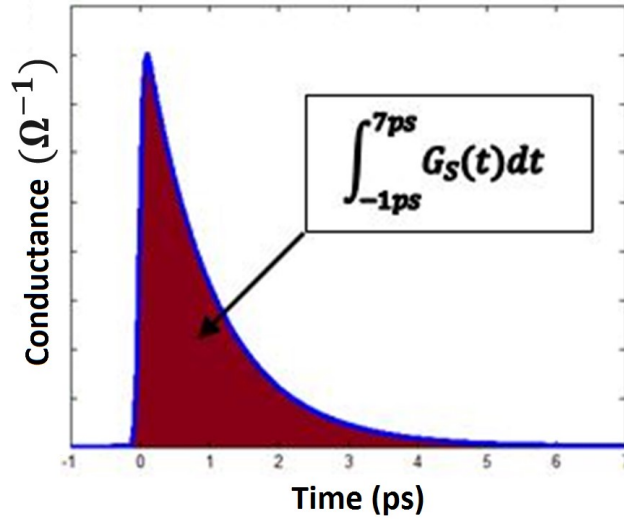
Figure 2.9 The area under the curve of the time-dependent antenna gap conductance.

First, it is assumed an approximate square current response and the constant number C is adjusted to give a peak conductance value of $0.4\Omega^{-1}$. The resultant time dependent behavior of the conductance is shown in Figure 2.10. The parameters were chosen as given in Table 2.2.
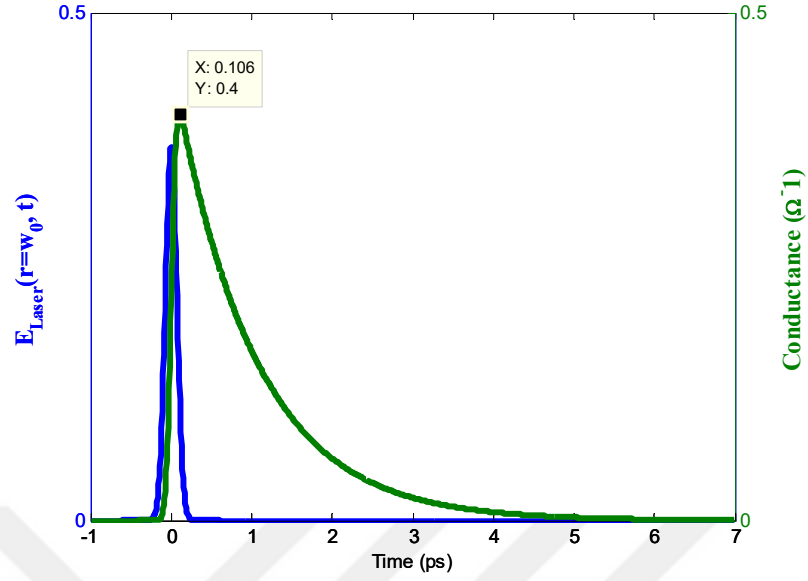
Figure 2.10 Time dependent behaviour of the incident E-field of the laser pulse and the conductance change with the applied field

As we can see in Figure 2.10, the decay time for the conductance is about 7 ps. This means that all the generated photocarriers recombined and there was no free carriers left in the LT-GaAs until a second pulse comes and hits onto the photoconductive surface. By using this natural result of the photoconductive material, we can take the lower and upper limits for the integral as -1ps and, 7 ps, respectively. The average source conductance integral can be calculated simply by calculating the area under the conductance curve and dividing it by the pulse repetition period. This way, we can obtain a more accurate value for constant C, which makes the average source resistance fits with the measurement without a square current approximation:

$$C = \frac{\frac{I_{PC,measured}}{V_{bias}}}{f_{REP} \int_{-1ps}^{7ps} G_S(t, C = 1)dt} \qquad (2.21)$$

where

$$\text{erf}(x) \quad = \quad \int_0^x e^{-t^2} dt \qquad \text{is called error function.}$$

Using numerical integration techniques for calculating the area under the conductance curve and solving (2.21) gives a **C** value of 6.3552×10^{20}. Using the current value of constant C, we obtain the conductance change as in Figure 2.11. It is noticed from the figure that the peak value of the conductance curve is increased from 0.4 S to 0.7 S from square approximation to the more accurate calculation. This much of conductance corresponds to an antenna instantaneous resistance of $\sim 1.43\,\Omega$.
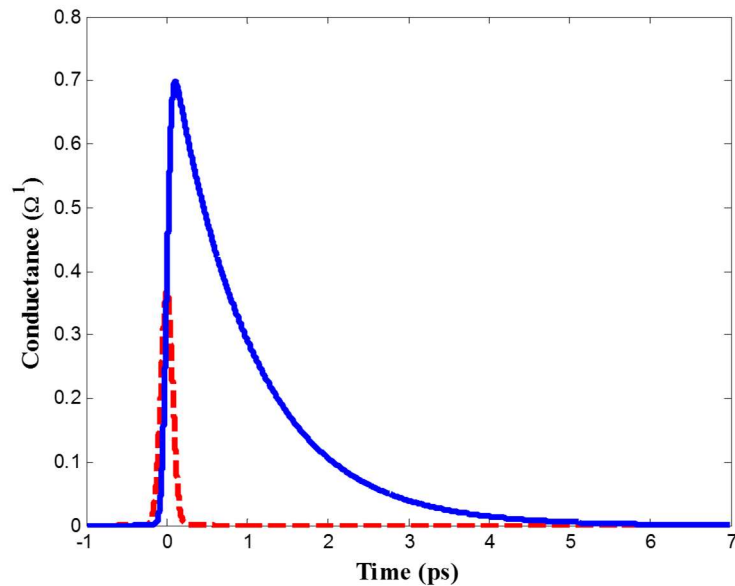
Figure 2.11 Time-dependent conductance change at the antenna gap for the current value of C.

2.6 Parametric Analysis of the Instantaneous and Average Source Conductance of the Photoconductive Antenna Excited By Laser Pulses
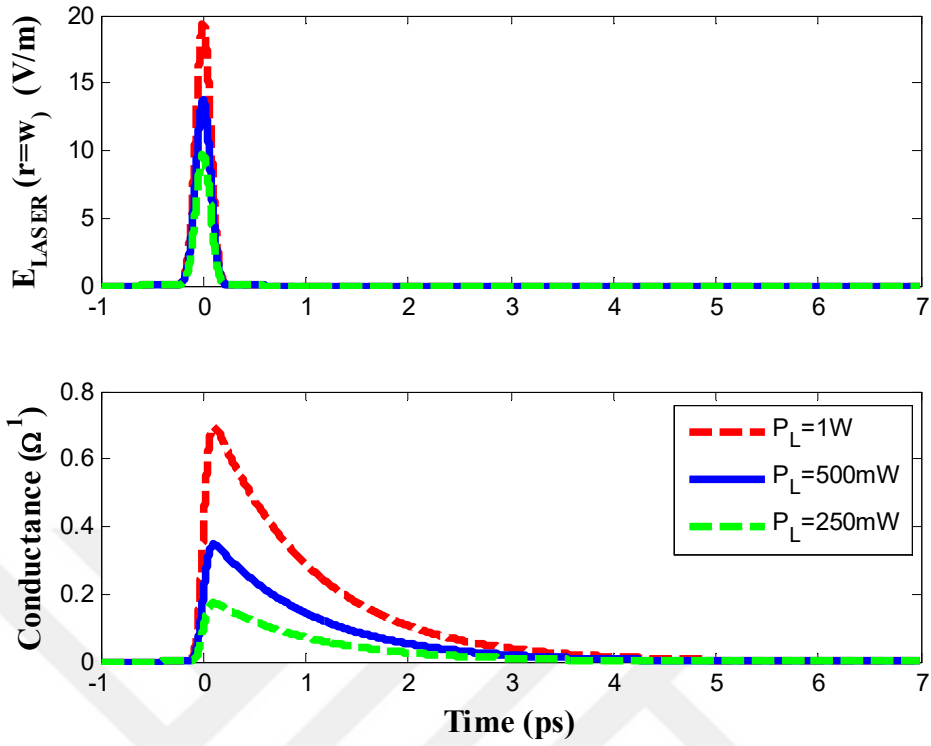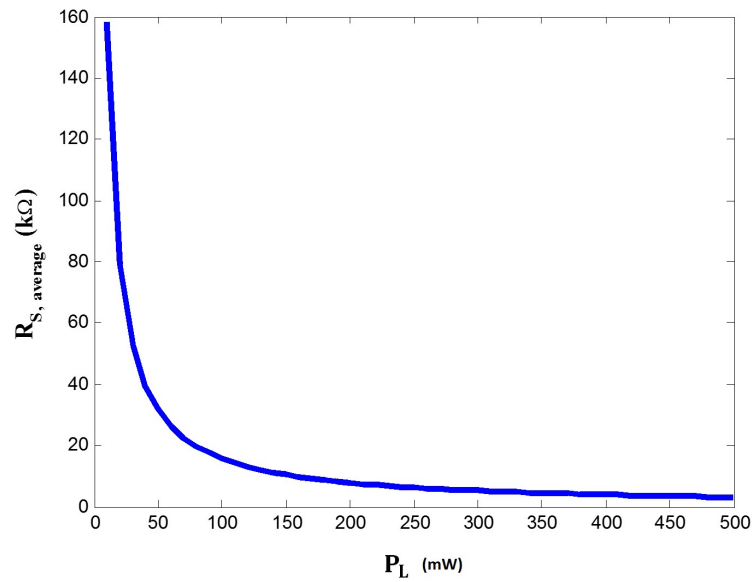
Figure 2.12 (a) Variation of the time-dependant conductance of photoconductive material by the average optical power. (b) Variation of the average source resistance of photoconductive material by the average optical power. ($\tau_L = 100$ fs, $f_{REP} = 80$ MHz $L = W = 10\ \mu m, t_{GaAs} = 1\ \mu m, , \tau_C = 1$ ps, $\mu_n = 1000 \frac{cm^2}{Vs}, \alpha = 6000\ cm^{-1}$)
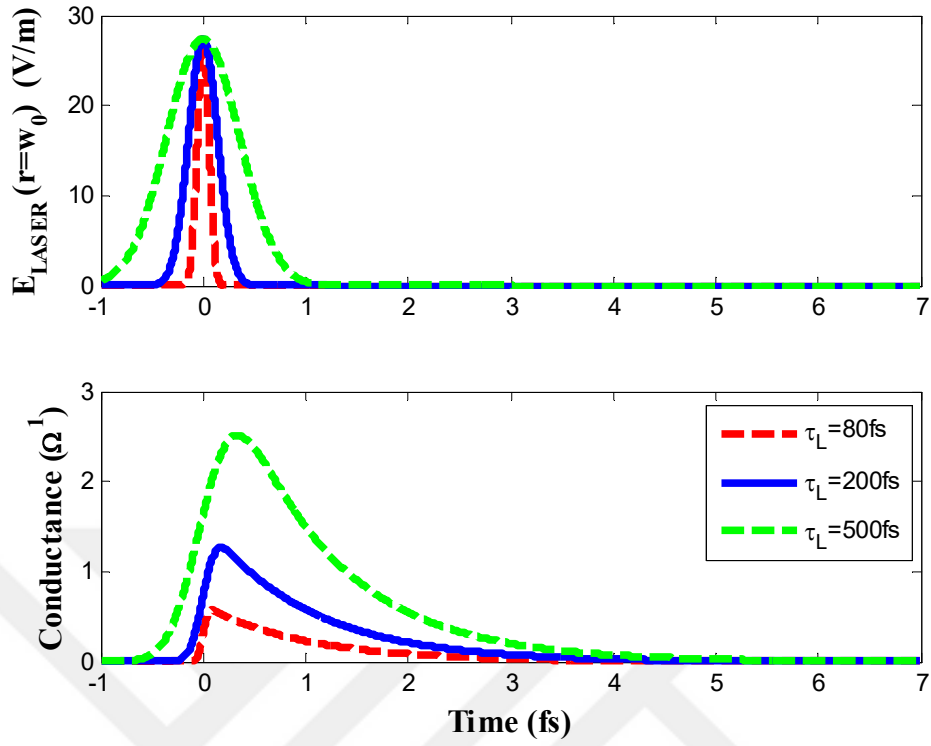
(a)
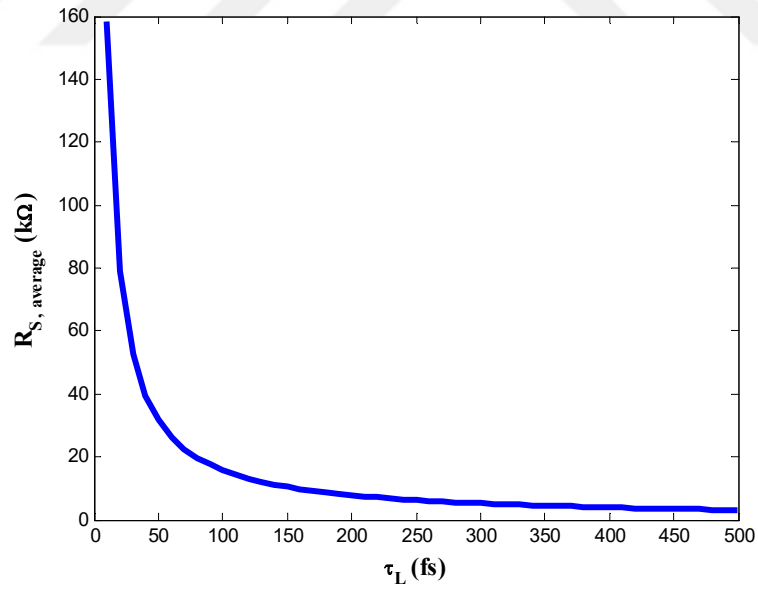
(b)

Figure 2.13 (a) Variation of the average source resistance of photoconductive material by the laser pulse duration. (b) Variation of the average source resistance of photoconductive material by the average optical power. (P_L=1 W, $f_{REP} = 80$ MHz $L = W = 10\ \mu m, t_{GaAs} = 1\ \mu m,, \tau_C = 1$ ps, $\mu_n = 1000\frac{cm^2}{Vs}, \alpha = 6000\ cm^{-1}$)
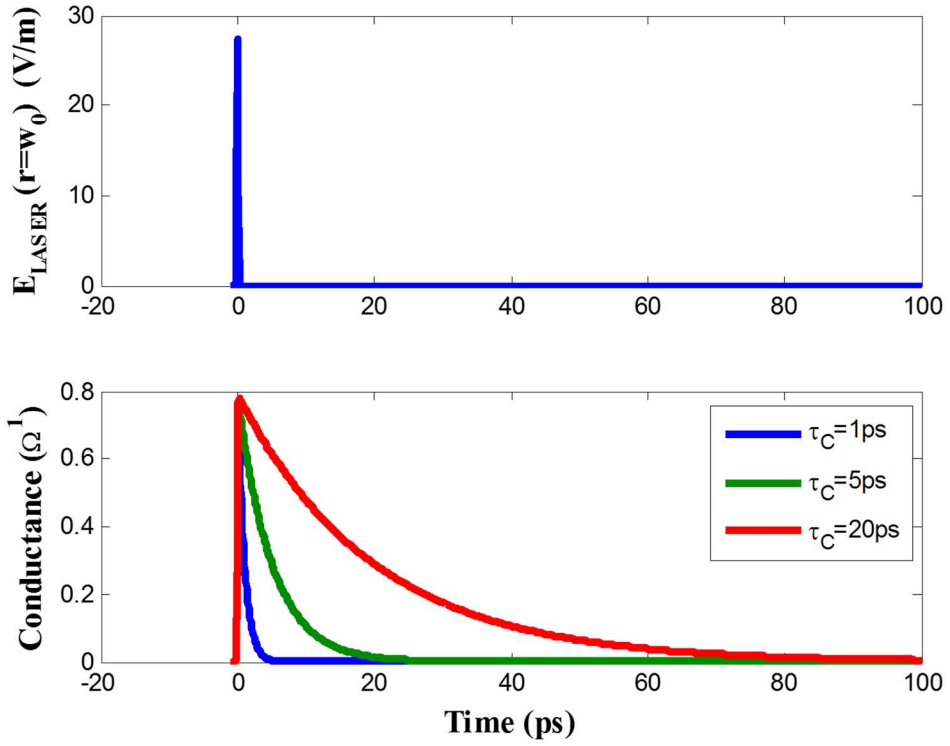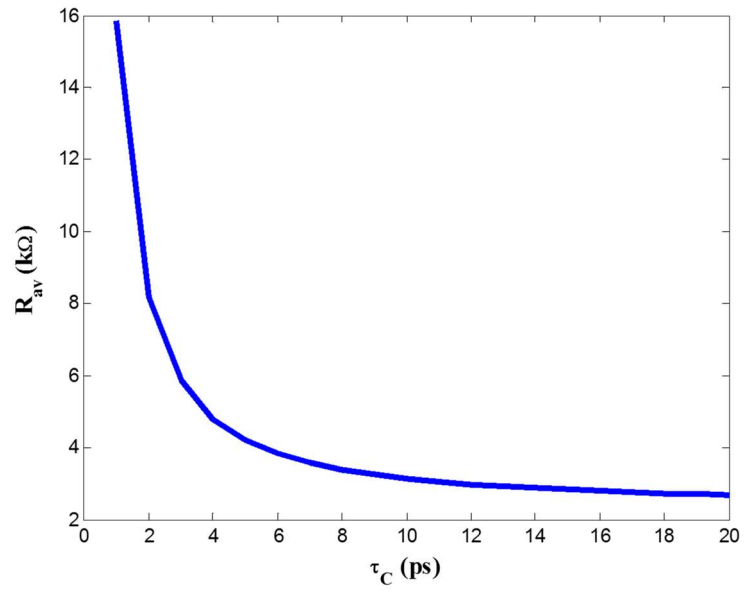
Figure 2.14 (a) Variation of the time-dependant conductance of photoconductive material by the carrier lifetime. (b) Variation of the average source resistance of photoconductive material by the carrier lifetime. ($P_L = 1\ W,\ f_{REP} = 80MHz, \tau_L = 100\ fs, L = W = 10\ \mu m, t_{GaAs} = 1\ \mu m, \mu_n = 1000 \frac{cm^2}{Vs},\ \alpha = 6000\ cm^{-1}$)
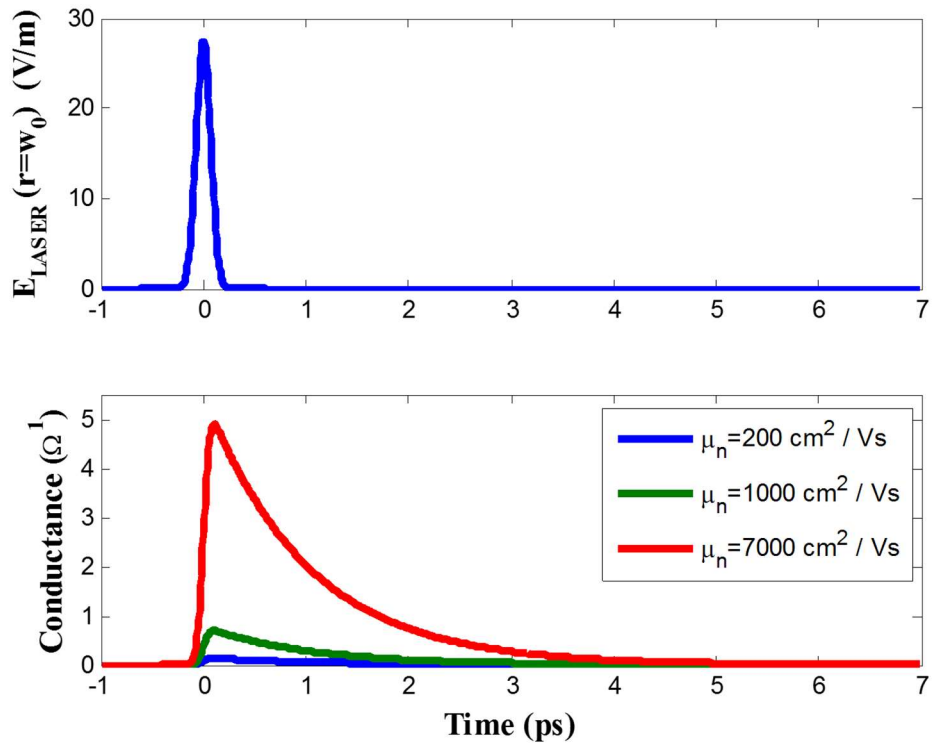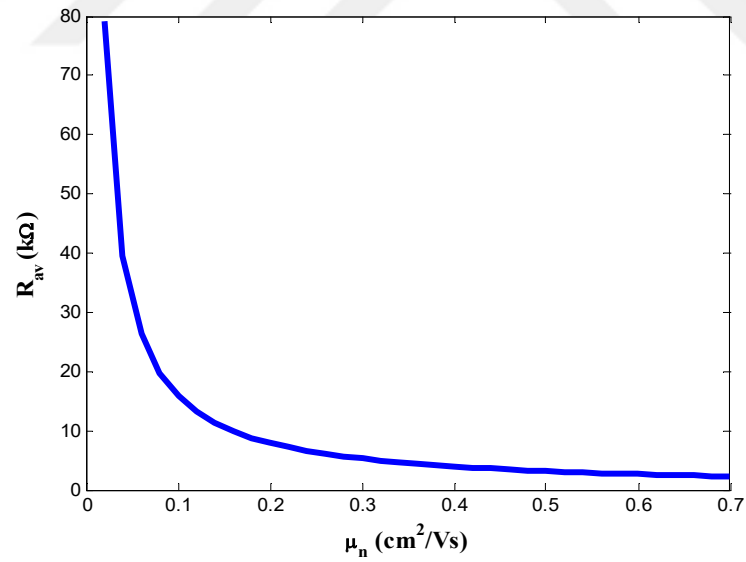
Figure 2.15 (a) Variation of the time-dependant conductance of photoconductive material by the electron mobility. (b) Variation of the average source resistance of photoconductive material by the carrier lifetime. ($P_L = 1\,W$, $f_{REP} = 80MHz$, $\tau_L = 100\,fs$, $L = W = 10\,\mu m$, $t_{GaAs} = 1\,\mu m$, $\alpha = 6000\,cm^{-1}$, $\tau_C = 1ps$)
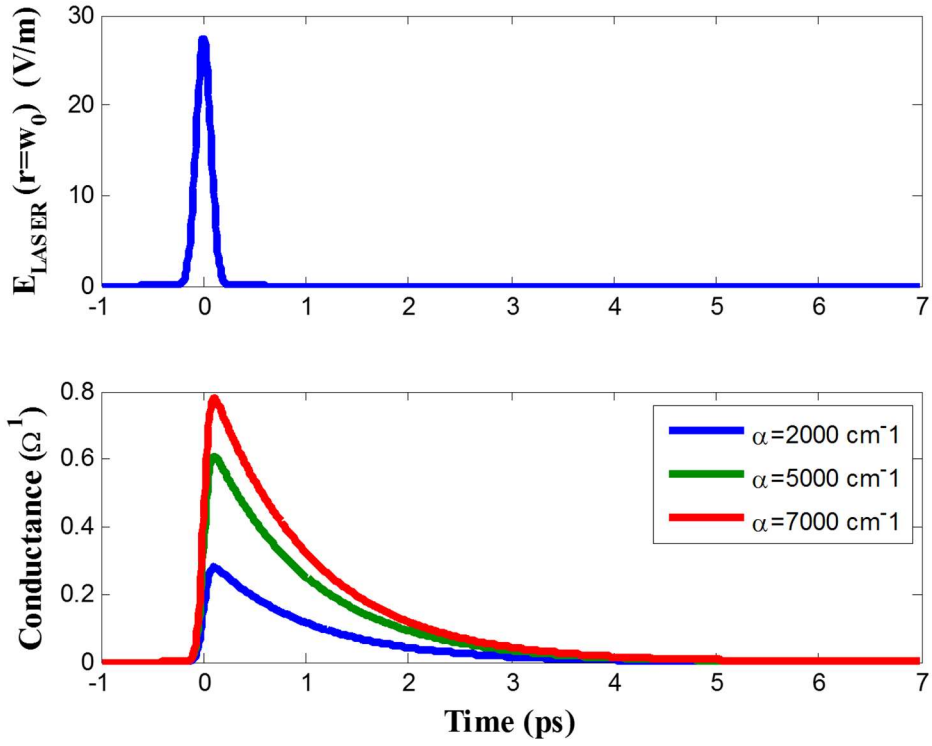
(a)
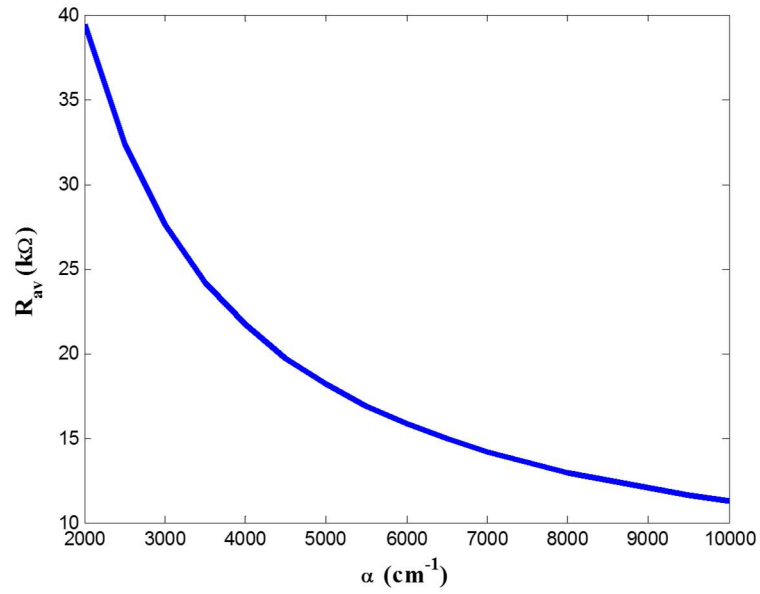
(b)

Figure 2.16 (a) Variation of the time-dependant conductance of photoconductive material by the absorbtion coefficient of the PC material. (b) Variation of the average source resistance of photoconductive material by the carrier lifetime. ($P_L = 1$ W, $f_{REP} = 80$MHz, $\tau_L = 100$ fs, L = W = 10 µm, $t_{GaAs} = 1$ µm, τ_C=1ps, $\mu_n = 1000 \frac{cm^2}{Vs}$)
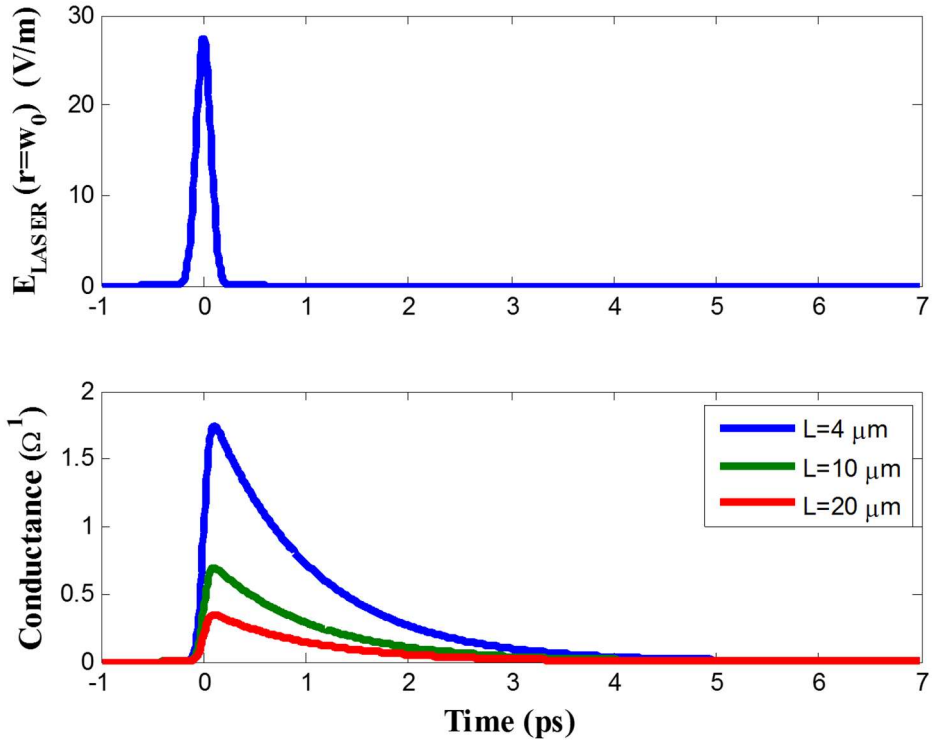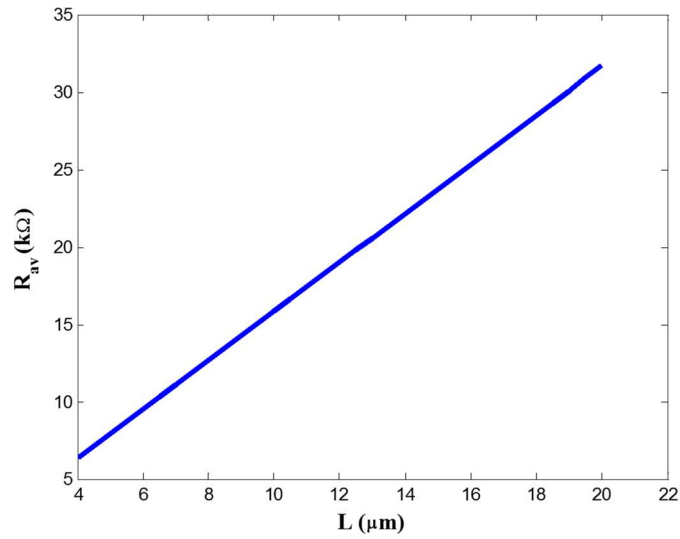
Figure 2.17 (a) Variation of the time-dependant conductance of photoconductive material by the antenna gap length. (b) Variation of the average source resistance of photoconductive material by the antenna gap length. ($P_L = 1$ W, $f_{REP} = 80$ MHz, $\tau_L = 100$ fs, $W = 10$ μm, $t_{GaAs} = 1$ μm, $\tau_C = 1$ ps, $\mu_n = 1000 \frac{cm^2}{Vs}$, $\alpha = 6000$ cm^{-1})

(a)

(b)
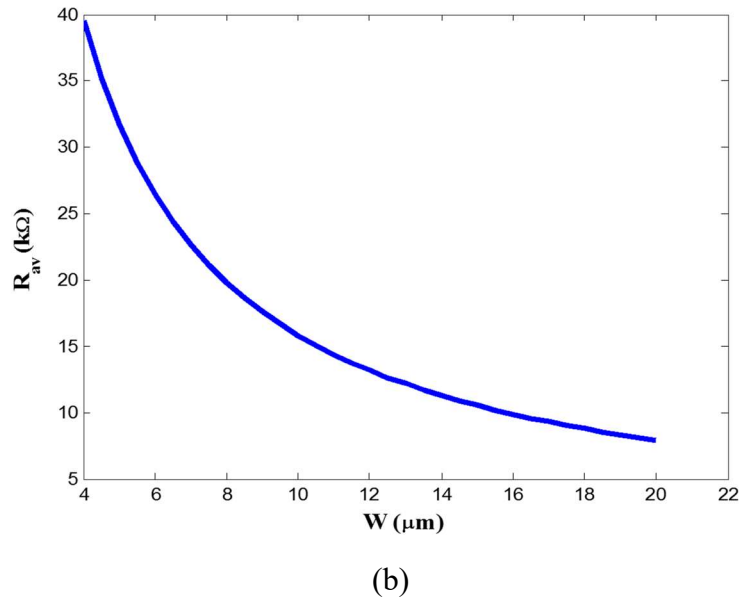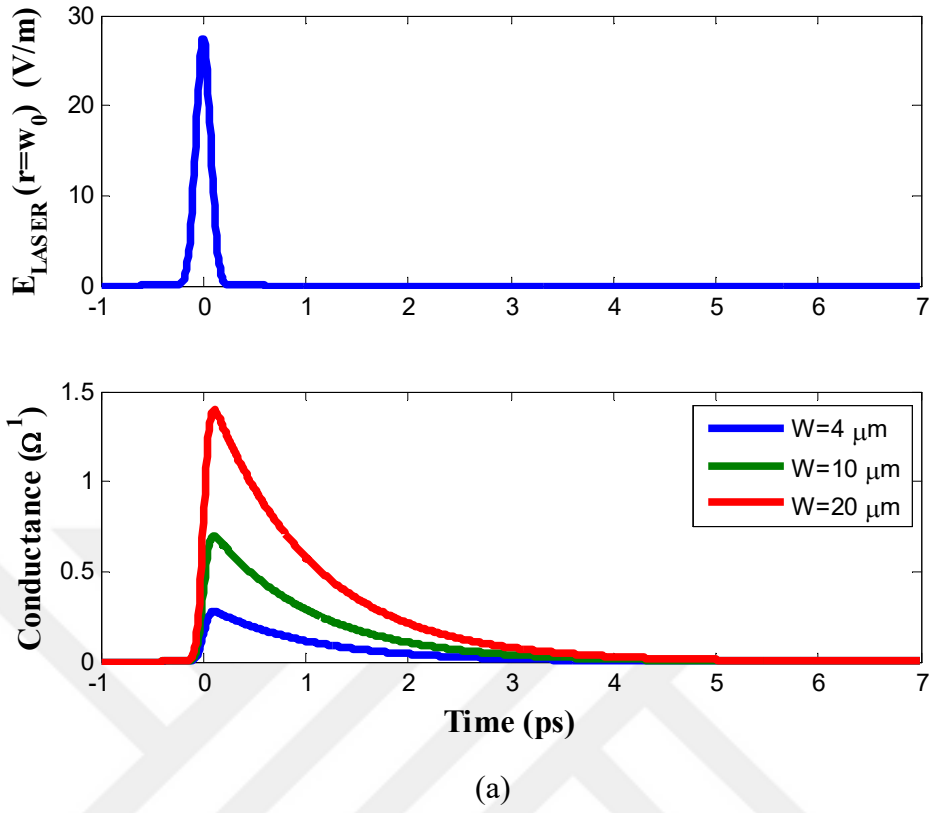
Figure 2.18 (a) Variation of the time-dependant conductance of photoconductive material by the antenna gap witdh. (b) Variation of the average source resistance of photoconductive material by the antenna gap width. (P_L= 1 W, f_{REP} = 80 MHz, τ_L= 100 fs, t_{GaAs}=1 μm, τ_C = 1 ps, μ_n= 1000 $\frac{cm^2}{Vs}$, α = 6000 cm^{-1}, L = 10 μm)
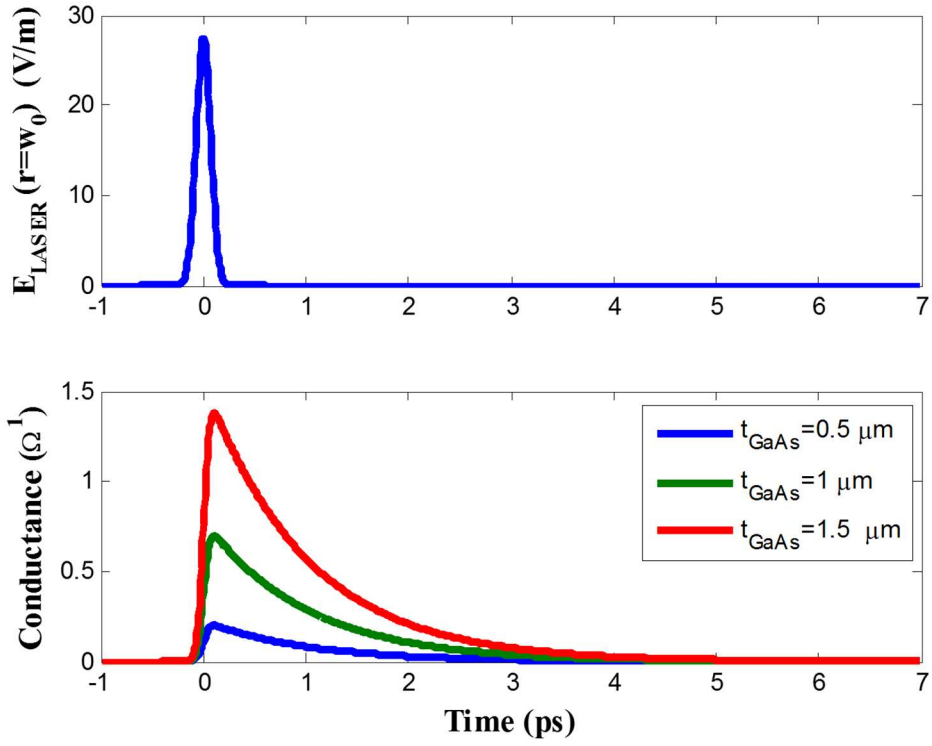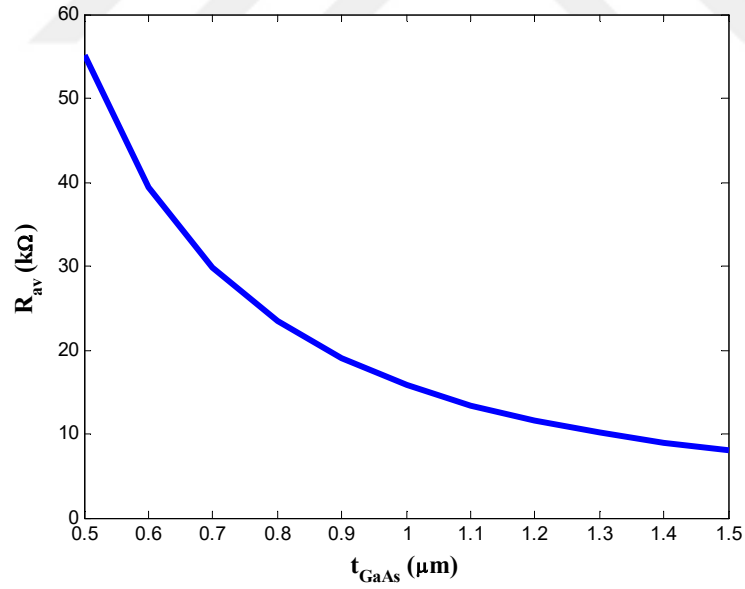
Figure 2.19 (a) Variation of the time-dependant conductance of photoconductive material by the thickness of the LT-GaAs layer. (b) Variation of the average source resistance of photoconductive material by the LT-GaAs thickness. (P_L= 1 W, f_{REP} = 80MHz, τ_L= 100 fs, L = 10 μm, t_{GaAs} = 1 μm, τ_C = 1 ps, μ_n= 1000 $\frac{cm^2}{Vs}$, α = 6000 cm^{-1})

The effects of the laser source, antenna geometry and photoconductive material parameters on the variation of the antenna gap conductance is observed from Figure 2.12 to Figure 2.19. These parameters can make variations depending on the type of the antenna, sensitive measurement environment, or even the unstable properties of the materials used for both antenna material or measurement setup. So, the constant number C should be adjusted after for each different measurement of the antennas.

Photoconductive antennas are generally deposited on LT-GaAs which is grown on SI-GaAs wafer at relativeşy low temperatures. The gap size of the antenna is10 µm x 10 µm. For pulsed excitation, a laser source of 10mW maximum power, 75 MHz laser pulse repetition rate and, 100 fs laser pulse duration is used. 35-40 V is applied to the arms of the photoconductive antenna. The thickness of the GaAs wafer is 635 μm of which 1.3μm LT-GaAs epi layer is grown on the SI-GaAs wafer.

2.7 The Equivalent Circuit Model for the Photoconductive Antenna System under Pulsed Excitation

In this section, the time-dependent voltage and current values under the voltage applied to the arms of the antenna will be derived. The equivalent circuit model for the photoconductive antenna in pulsed excited system is given in Figure 2.20.
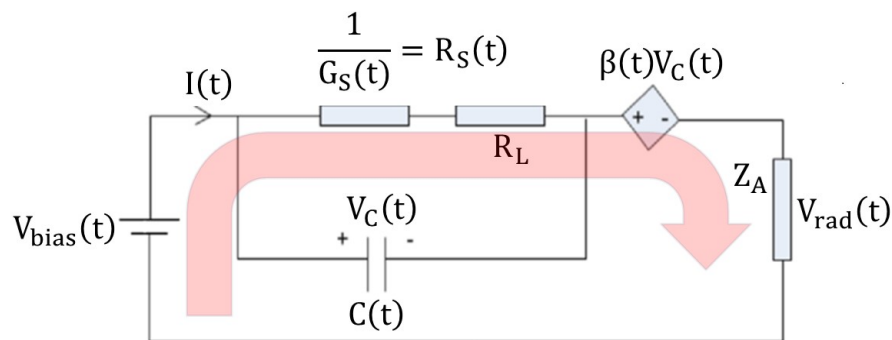
Figure 2.20 The equivalent antenna model for THz antennas [1]

The schematic view of the THz antenna is shown in Figure 2.21. When a laser pulse of photon energy greater than the energy band of the LT-GaAs is incident onto the

antenna hap region, free electron-hole pairs are released in the material. The applied voltage, $V_{bias}(t)$, creates an electric field, E_{bias}, through the gap of the antenna, and this field accelerates free carriers. While the electrons move through the positively biased electrode, holes move through the negatively biased arm. The number of the defect sites in the active region determines carrier lifetime.
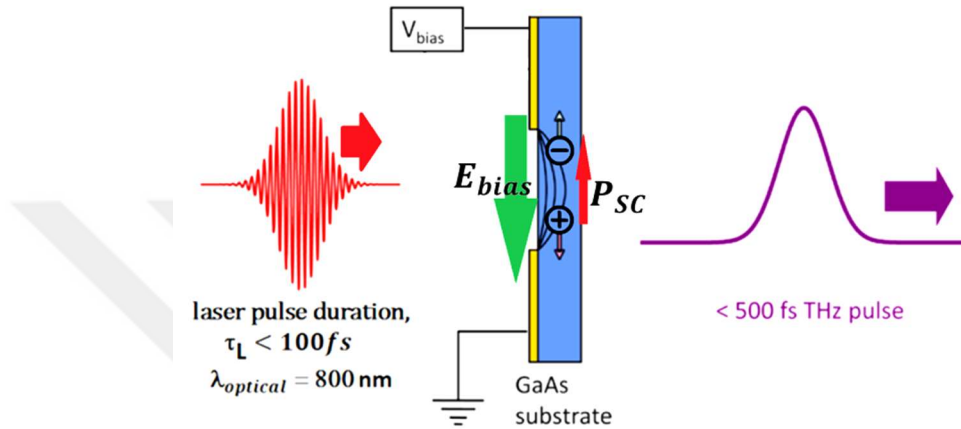
Figure 2.21 The schematic view of the THz photoconductive antenna in pulsed system

Due to the speration of positive and negative charges in the direciton oppsite to the E_{bias}, reduction of the effective electric field is observed at the gap antenna. This effect is taken into account in the circuit by $\beta(t)V_C(t)$. As the induced elektric field increases at the antenna gap, more separation of charges take place.

R_L represents the electrode loss resistance

Z_A represents the antenna input impedance. This value only changes by the antenna geometry.It does not show dependence on the operation frequency.

When the wavelength of the generated THz wave is considered to be much greater than the size of the antenna gap, the instantaneous change of the electric field through the gap of the antenna, $E_C(t)$, can be viewed to be same directional and constant over the gap surface. The radiated electric filed is proportional to the time derivative of the antenna cuuretn, I_{PC}, as [1]:

$$E_{THz} \sim \frac{\partial I_{PC}(t)}{\partial t} \sim \frac{\partial J_{PC}(t)}{\partial t} \qquad \textbf{(2.22)}$$

The current density at the active regions is [1]:

$$J_{PC}(t) = qn(t)v(t) \qquad \textbf{(2.23)}$$

where

q	=	Elementary charge
$n(t)$	=	Time-dependent free charge
$v(t)$	=	Speed of the charge

The average charge speed is:

$$v(t) = \mu_n E_C(t) \qquad \textbf{(2.24)}$$

where

$E_c(t)$	=	Electric field at the antenna gap
μ_n	=	Mobility of the electrons

The electric field at the antenna gap with the uniform field assumption is approximated by:

$$E_C(t) = \frac{V_C(t)}{L} \qquad \textbf{(2.25)}$$

where

L	=	The length of the antenna gap through the induced electric field.

Combining the above equation into a singe equation gives the current density of the form:

$$J_{PC}(t) = qn(t)\mu_n \frac{V_C(t)}{L} \qquad (2.26)$$

The current density across the antenna is:

$$\begin{aligned} I_{PC}(t) &= J_{PC}(t)S \\ &= qn(t)\mu_n \frac{V_C(t)}{L} W t_{GaAs} \end{aligned} \qquad (2.27)$$

To be able to obtain the voltage which is responsible for the radiation, V_{rad}, we use the following voltage drop equation:

$$\begin{aligned} V_{rad}(t) &= I_{PC}(t)Z_A \\ &= qn(t)\mu_n \frac{V_C(t)}{L} W t_{GaAs} Z_A \end{aligned} \qquad (2.28)$$

As it can be seen from the derived equations, all the parameters in the equivalent model can be expressed as a function of antenna gap voltage, $V_C(t)$. So, obtaining a solution for $V_C(t)$, also makes it available to obtain the other parameters in the model. Now, the method for obtaining an expression for $V_C(t)$ will be explained.

2.8 Derivation of the Antenna Gap Voltage

From the equivalent ciruit model, the current flowing through the main branch of the circuit, $I_{PC}(t)$, is expressed as a function of the antenna gap votage, $V_C(t)$ as:

$$I_{PC}(t) = V_C(t)\left[\cfrac{1}{\cfrac{1}{G_S(t)} + R_L}\right] + \frac{d}{dt}[V_C(t)C(t)] \qquad \text{(2.29)}$$

where

$$R_L \quad = \quad \text{Electrode loss resistance}$$

R_L may be ignored since antenna electrodes are good conductors. So the simplified photocurrent is:

$$I_{PC}(t) = V_C(t)G_S(t) + \frac{dV_C(t)}{dt}C(t) + \frac{dC(t)}{dt}V_C(t) \qquad \text{(2.30)}$$

Taking $\frac{dV_C(t)}{dt}$ term to the left hand side of the equation gives:

$$\frac{dV_C(t)}{dt} = \frac{1}{C(t)}\left[I_{PC}(t) - V_C(t)G_S(t) - \frac{dC(t)}{dt}V_C(t)\right] \qquad \text{(2.31)}$$

Now, the only term that does not change by $V_C(t)$ is $I_{PC}(t)$. Applying KVL gives:

$$\begin{aligned}
V_{bias} - V_C(t) - \beta(t)V_C(t) + V_{RAD}(t) &= 0 \\
V_{bias} - V_C(t)[1 + \beta(t)] + I_{pc}(t)Z_A &= 0 \\
\rightarrow I_{PC}(t) = \frac{V_{bias}}{Z_A} - V_C(t)\frac{1 + \beta(t)}{Z_A} &
\end{aligned} \qquad \text{(2.32)}$$

Substituting $I_{PC}(t)$ into **(2.32)** gives a final equation which is only expressed in terms of function $V_C(t)$:

$$\frac{dV_C(t)}{dt} = \frac{1}{C(t)}\left[\frac{V_{bias}}{Z_A} - V_C(t)\frac{1}{Z_A} - V_C(t)\frac{\beta(t)}{Z_a} - V_C(t)G_S(t) - \frac{dC(t)}{dt}V_C(t)\right]$$

(2.33)

Dividing both sides of the equation by $V_C(t)$ gives an equation in terms of function $E_C(t)$. The reason for this variable change is due to the reason that in [7], there is an an expression for $E_C(t)$ and so we will be able to equate the terms of the two equations and find time dependent expressions for the functions $\beta(t)$ and $C(t)$. Dividing both sides by L gives:

$$\frac{dE_C(t)}{dt} = \frac{1}{C(t)}\left[\frac{V_{bias}}{Z_A L} - E_C(t)\frac{1}{Z_A} - E_C(t)\frac{\beta(t)}{Z_A} - E_C(t)G_S(t) - \frac{dC(t)}{dt}E_C(t)\right]$$

(2.34)

The equation for $E_C(t)$ which is given in [7] is:

$$\frac{dE_C(t)}{dt}$$
$$= \frac{1}{\left[1 + \frac{q\mu_n Z_A S}{L}n(t)\right]}\left[-\frac{1}{\tau_R}E_C(t) - \left(\frac{q\mu_n Z_A S}{\tau_R L} + \frac{q\mu_n}{\kappa\epsilon}\right)n(t)E_C(t) - \frac{q\mu_n Z_A S}{L}\frac{dn(t)}{dt}E_C(t) + \frac{V_{bias}}{\tau_R}\right]$$

(2.35)

where

κ	=	Screening effect coefficient
ϵ	=	Dielectric constant (12.9 for GaAs [8])

Matching the terms of the two equations gives expressions for $C(t)$ and $\beta(t)$ in terms of n(t) [1]:

$$C(t) = \frac{\tau_R}{Z_A}\left(1 + \frac{q\mu_n Z_A Sn(t)}{L}\right)$$

(2.36)

$$\beta(t) = \frac{q\mu_n \tau_R n(t)}{\zeta \epsilon}$$

(2.37)

Substituting $C(t)$ and $\beta(t)$ in the differential equation gives:

$$\frac{dV_C(t)}{dt} = \frac{1}{\frac{\tau_R}{Z_A}\left(1 + \frac{q\mu_n Z_A Sn(t)}{L}\right)}\left[\begin{array}{c}\frac{V_{bias}}{Z_A} - V_C(t)\frac{1}{Z_A} - \frac{V_C(t)\frac{q\mu_n \tau_R n(t)}{\zeta \epsilon}}{Z_A}\\ -V_C(t)G_S(t) - \frac{dC(t)}{dt}V_C(t)\end{array}\right]$$

(2.38)

When the prefoud expression for n(t) in (2.12) is put in the differential equation, we obtain the final equation that we need to solve. Since the known forms of the solution techniques for differential equations do not work for the obtained equation in (2.38), numerical techniques will be used to solve this differential equation.

2.9 Solution of the 1st Order Differential Equation by Runge-Kutta Method [8]

To solve the differential equation given in (2.38) with the open expression of n(t) is substituted, Runge-Kutta method will be used. The solution steps for this method are:

- First, calculate k_1, k_2, k_3, k_4 by assuming an addition of h is made to the x in the first order dferential equation ($y' = f(x, y)$):

$$k_1 = hf(x, y)$$

$$k_2 = hf\left(x + \frac{1}{2}h, \quad y + \frac{1}{2}k_1\right)$$

$$k_3 = hf\left(x + \frac{1}{2}h, \quad y + \frac{1}{2}k_2\right) \tag{2.39}$$

$$k_4 = hf\left(x + \frac{1}{2}h, \quad y + k_3\right)$$

- Then, find the change in y by calculating the linear combination of k_1, k_2, k_3, k_4 as:

$$y(x + h) \cong y(x) + \frac{1}{6}(k_1 + 2k_2 + 2k_3 + k_4) \tag{2.40}$$

To understand the accuracy of the solution of differential equation, decrease the value of h, and solve the same equation for the new values of h. If both solutions are close enough, the solution is accepted to be okay.

In our case, y(x) function corresponds to $V_C(t)$, x variable corresponds to t vaiable.

The initial value condition of the differeantial equation is $V_C(t = -1\text{ps}) = 30$ V. Because, the antenna gap is assumed to be an open circuit when it is not illuminated by the laser source. As a result, the antenna gap voltage is equal to the voltage applied to the antenna arms. In fact, there is a high value of resistance at the gap when it is not illuminated. This resistance is called 'dark resistance'.

With the given initial value condition, the flow chart of the Runge-Kutta method is shown in Figure 2.22.
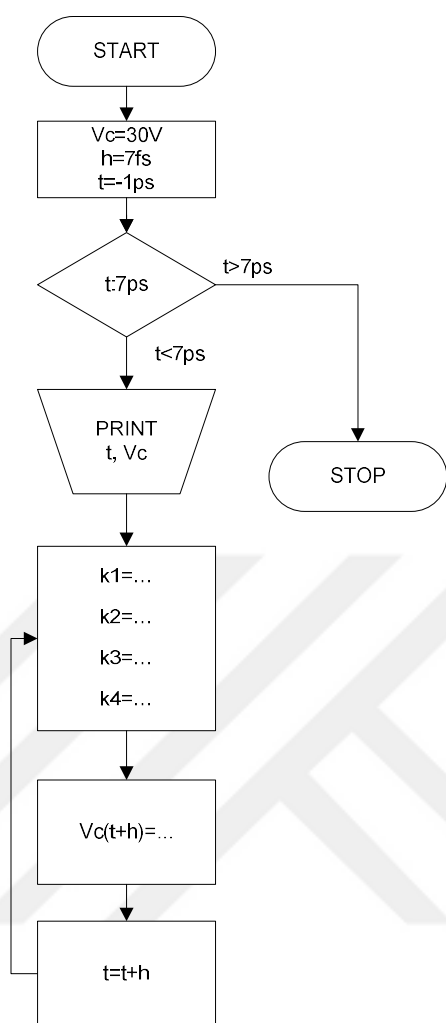
Figure 2.22 Runge-Kutte flow chart

When this algorithm is applied in MATLAB, the time-dependent antenna gap voltage change is plotted in Figure 2.23.
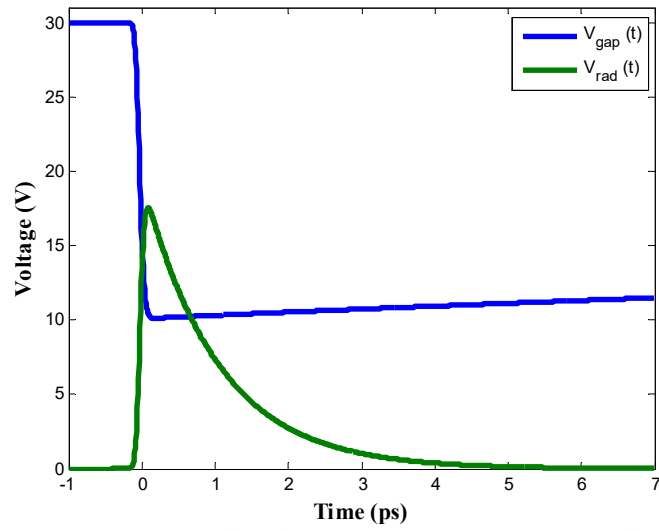
(a)
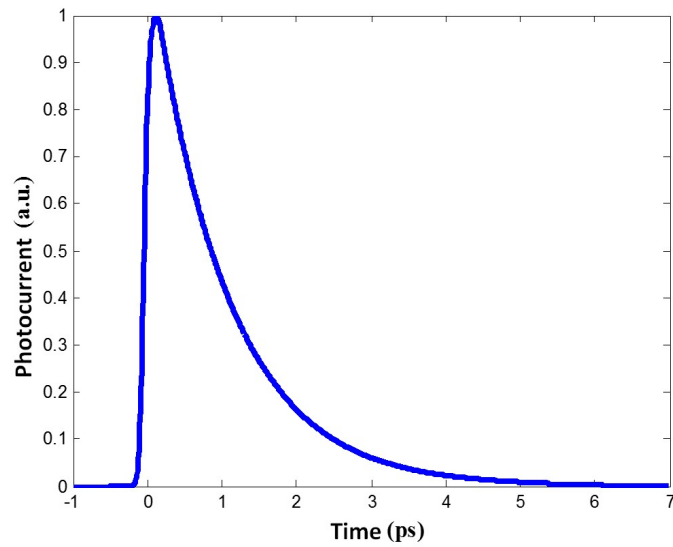
(b)

Figure 2.23 Time-dependent behaviour of the (a) gap and raiation voltage (b) Photocurrent
(arbitrary unit).

2.10 Theoretical Modelling of the THz Photoconductive Antennas Driven by Photomixer

To be able to understand the the mechanism of the antennas driven by the photomixers, we first need to understand the theoretical modelling of the photomixer process. A

schematic representation of the antennas operating with photomixer is shown in Figure 2.24. A photoconductive material is illuminated by two laser beams at the same direction and polarization at slightly different frequencies. One of the laser is fixed to a constant frequency and the other is tuned to a frequency which makes a difference ffrequency at the desired THz radiation. The antenna gap is illuminated with these two mixed laser beams. When the two beams are aligned on the same line with same polarization and direction they are modulated in air before they are incident on to the gap. It can clearly be understood by a simple example. It is assumed two beams have electric fields E_1 and E_2 are polarized in the x direction with frequencies of ω_1 and ω_2. When they are perfecty overlapped in the air, the resultant total electric field can be written in phasor form as:
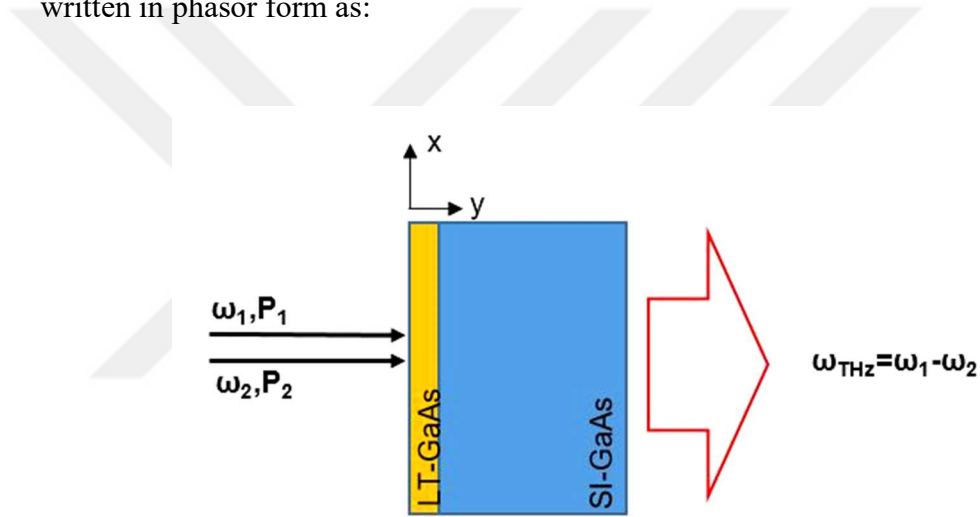
Figure 2.24 Schematic view of the generated THz frequency by photomixing process

$$E(t) = \hat{a}_x E_1 e^{(i\omega_1 t)} + \hat{a}_x E_2 e^{(i\omega_2 t)}$$

$$= \hat{a}_x E_1 e^{j\left(\omega_0 + \frac{\omega_{THz}}{2}\right)t} + \hat{a}_x E_2 e^{j\left(\omega_0 - \frac{\omega_{THz}}{2}\right)t} \tag{1}$$

$$= \hat{a}_x e^{(j\omega_0 t)} \left[(E_1 + E_2) \cos\left(\frac{\omega_{THz}}{2}\right) + j(E_1 - E_2) \sin\left(\frac{\omega_{THz}}{2}\right) \right]$$

where

$$\omega_0 \quad = \quad \frac{\omega_1 + \omega_2}{2}$$

$$\omega_{THz} \quad = \quad \omega_1 - \omega_2$$

Then, we can analyse the total power which is incident onto the antenna by calculating the average power density (Poynting vector) as:

$$\vec{P}_L = \vec{P}_L(r,t) = \vec{E}(r,t) \times \vec{H}(r,t)$$

$$= \hat{a}_z \left[\frac{1}{\eta_0} E_0(r,t)^2 \right]$$

$$= \hat{a}_z \frac{1}{2\eta_0} \mathrm{Re} \left[(E_1 + E_2)^2 \cos^2 \left(\frac{\omega_{THz}}{2} t \right) \right.$$

$$+ (E_1 - E_2)^2 \sin^2 \left(\frac{\omega_{THz}}{2} t \right) \qquad (2.41)$$

$$\left. - 2j(E_1^2 - E_2^2) \cos \left(\frac{\omega_{THz}}{2} t \right) \sin \left(\frac{\omega_{THz}}{2} t \right) \right]$$

$$= \hat{a}_z \frac{1}{2\eta_0} [E_1^2 + E_2^2 + 2E_1 E_2 \cos(\omega_{THz} t)]$$

$$= P_1 + P_2 + 2\sqrt{P_1 P_2} \cos(\omega_{THz} t)$$

The expression for the total power shows a resultant power with totally mixed signals which means there is no any slight difference between the polarizations, phases of the two waves and the directions of the wave propagations. Here, P_1 and P_2 terms are eliminated when they are incident onto the LT-Gas layer. Because the semiconductor can not respond to such high frequencies. In the other words, the lementary dipoles in the material can not align themselves with the electric field varying with a speed much greater than their resonance frequency.

This mixing phenomena is formulized by assuming a factor called 'mixing efficieny' in front of the right-most term of eqn. (2.41) with a value of 1. If there was a difference

between the phases, polarization directions, or propagation directions of the two waves, they would not be perfectly overlapping and the mixing efficiency would have a value lower than unity. So the total modulated power would be smaller. So, the the power equation for perfect mixing can be arranged as:

$$P_L = P_0 + 2\sqrt{mP_1P_2}\cos(\omega_{THz}t) \tag{2.42}$$

where

P_0	$=$	P_1+P_2	is the total incident power
m	$=$	$\left(\dfrac{E_1 \cdot E_2}{|E_1||E_2|}\right)^2$	is the mixing efficieny changing between 0 and 1.

This is focused onto the gap between the arms of the dipole antenna. For free electron-hole pairs to release in the substrate, the photon energies of the two waves, hf_1, ve hf_2, should be greater than the room temperature band gap energy of the GaAs (1.42 eV).

At the air-LT-GaAs boundary, there is a reflection due to the change in the dielectric properties between the two medias. Taking this reflection coefficient in to account, we can write the accepted power at the boundary as:

$$P_A = P_0(1 - R)\left[1 + \frac{2\sqrt{mP_1P_2}}{P_0}\cos(\omega_{THz}t)\right] \tag{2.43}$$

This power is the power that is responsible for free electron-hole pairs to release in the materail. For further simplifying the calculations, we ignore the contribution of hoes on the photocurrent due to their high effective mass and low mobility with respect to electrons. ($\mu_e \gg \mu_h$)

As in the pulsed excited system, we will use the equation given in (2.9) to obtain the time-dependent change of carrier density simply by inserting the accepted power expression for CW excitation case:

$$\frac{dn(t)}{dt} + \frac{n(t)}{\tau_c} = \frac{\alpha}{hf_L} P_A(r, t)$$

$$\frac{dn(t)}{dt} + \frac{n(t)}{\tau_c} = \frac{\alpha}{hf_L} P_0(1 - R)\left[1 + \frac{2\sqrt{mP_1P_2}}{P_0}\cos(\omega_{THz}t)\right]$$

(2.44)

where

τ_c	=	Trapping time (carrier lifetime)
$g(t)$	=	Generated carrier density [1]
hf_L	=	Photon energy
α	=	The absorption coefficient which shows the dependence of the carrier density as going inside the depth of the LT-GaAs layer in to the z-direction. ($e^{-\alpha t_{GaAs}}$)

The solution of equation in (2.44) for n(t) gives:

$$n_{CW}(t) = C1e^{-\frac{t}{\tau_c}}$$
$$+ C2\left[\frac{\alpha\tau_c(1 - R)}{hf_L(\tau_C^2\omega_{THz}^2 + 1)}\right]\left[P_0(1 + \tau_C^2\omega_{THz}^2)\right.$$
$$\left. + 2P_2\sqrt{m}\{\cos(t\omega_{THz}) + \tau_C\omega_{THz}\sin(t\omega_{THz})\}\right]$$

(2.45)

In this equation, while the term in the right hand side of n(t) is continupusly change by time, the term in the left hand side, $C1e^{-\frac{t}{\tau_c}}$, is transient and decays in a very short time period of 5 psas shown in Figure 2.25. For the sake of simplicity, this transient term is neglectedand $n_{CW}(t)$ is accepted as:

$$n_{CW}(t) = \left[\frac{\alpha\tau_c(1-R)}{hf_L(\tau_C^2\omega_{THz}^2 + 1)}\right]\left[P_0(1 + \tau_C^2\omega_{THz}^2)\right.$$
$$\left. + 2P_2\sqrt{m}\{\cos(t\omega_{THz}) + \tau_C\omega_{THz}\sin(t\omega_{THz})\}\right] \qquad \textbf{(2.46)}$$
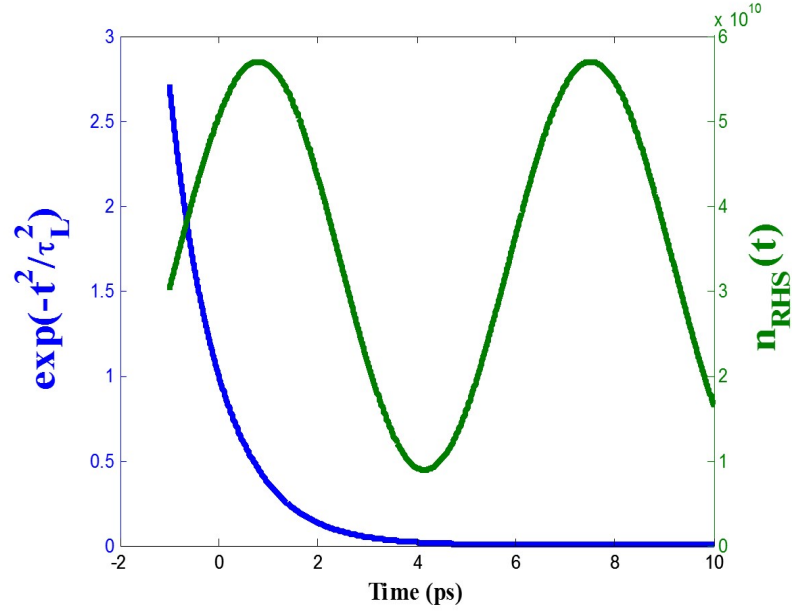
Figure 2.25 Time-dependent behaviour of the transient and continuous terms of $n_{CW}(t)$ ($f_{THz} = 340\ GHz, m = 1, L = W = 10\ \mu m, t_{GaAs} = 1\ \mu m,\ \tau_C = 1ps, \mu_n = 1000\frac{cm^2}{Vs}, \alpha = 6000\ cm^{-1}$, C1 = C2 = 1).

By using the equation in (2.15), the instantaneous change of the conductivity which is dependent on the LT-GaAs layer thickness can be expressed as [1]:

$$\sigma_{CW}(z, t) = \sigma(t)e^{-\alpha z}$$
$$\approx n_{CW}(t)\mu_n q e^{-\alpha z}$$
$$\approx C2\left[\frac{\alpha\tau_c(1-R)}{hf_L(\tau_C^2\omega_{THz}^2 + 1)}\right]\left[P_0(1 + \tau_C^2\omega_{THz}^2)\right. \qquad \textbf{(2.47)}$$
$$+ 2P_2\sqrt{m}\{\cos(t\omega_{THz})$$
$$\left. + \tau_C\omega_{THz}\sin(t\omega_{THz})\}\right]\mu_n q e^{-\alpha z}$$

The change of conductivity with time at different LT-GaAs layer depths is given in Figure 2.26. The more the depth is, the less number of free carriers take place and the conductivity is lower.
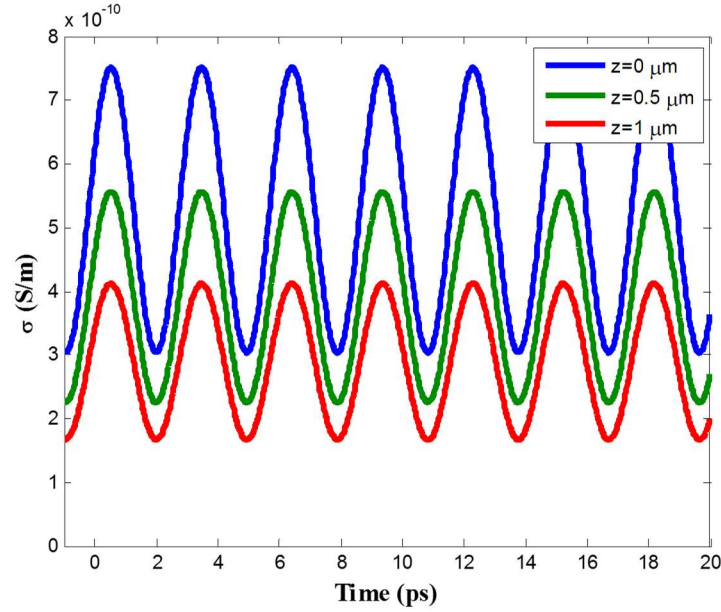
Figure 2.26 Variation of the time-dependant conductivity of photoconductive material by the antenna gap thickness. ($f_{THz} = 340\ GHz, m = 1, L = W = 10\ \mu m, t_{GaAs} = 1\ \mu m,\ \tau_C = 1ps, \mu_n = 1000\ \frac{cm^2}{Vs}$, $\alpha = 6000\ cm^{-1}$)

If we take the integral of the layer conductivity found in (2.47) over the depth of the LT-GaAs layer, we can find the total conductivity of the antenne gap active region. Here, it is assumed that the antenna gap is illuminated homogeneously.

If the number of free charges was constant through the depth of 1 μm LT-GaAs layer, the total conductivity could be calculated by the simple equation of the form $G_s(t) = \sigma(t)\frac{Wt_{GaAs}}{L}$. However, the value of the conductance is dependent on the depth of the layer in the z-direction. So, the integral over the volume of the antenna gap region determined by the Lt-GaAs layer thickness is [5]:

44

$$G_{sCW}(t) = \int_0^{t_{LT-GaAs}} \sigma(z,t)e^{-\alpha z}\frac{Wt_{GaAs}}{L}\,dz$$

$$G_{sCW}(\omega_{THz},t) = C2\frac{TWq\tau_C\mu_n e^{-t_{GaAs}\alpha}(1-R)}{Lf_Lh(\tau_C^2 w_{THz}^2 + 1)}(e^{t_{GaAs}\alpha} - 1) \qquad \textbf{(2.48)}$$

$$\begin{aligned}[P_0(1 + \tau_C^2\omega_{THz}^2) \\ + 2P_2\sqrt{m}\{\cos(t\omega_{THz}) + \tau_C\omega_{THz}\sin(t\omega_{THz})\}]\end{aligned}$$

The equivalent circuit model for the phoroconductive antenna is shown in Figure 2.17.
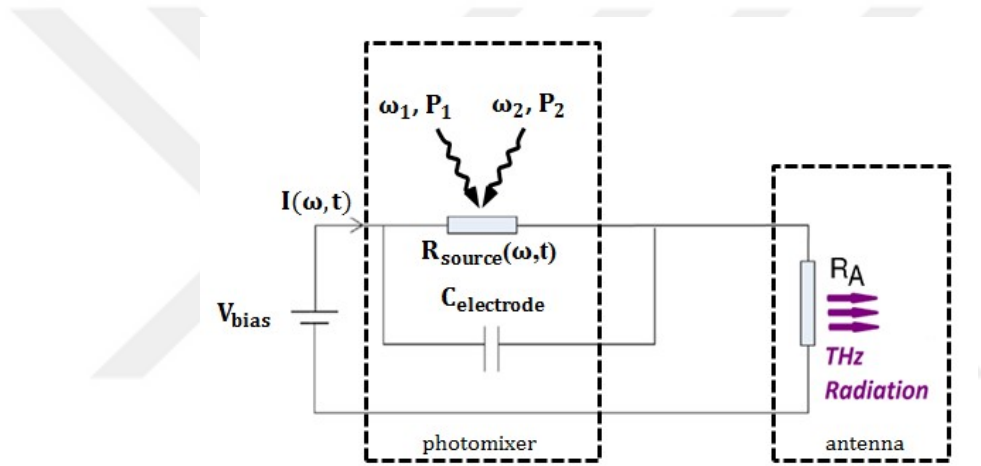
Figure 2.27 Equivalent circuit model for photomixer and antenna.

As it was also the case for the pulsed excitation system, we again need to assign a proper value for the factor of C2. For this to be applied, we first need to obtain measurement results which are applied DC voltage and the average current passing through the antenna arms. By using these values, we obtain the average resistance of the antenna gap under illumination. We use the following equlities to confirm a obtain C2 value:

$$G_{sCW,measured} = \vec{G}_{sCW}$$

$$\frac{I_{PC,measured}}{V_{bias}} = f_{THz} \int_0^{T_{THz}} G_{sCW}(t)dt \qquad (2.49)$$

$$C2 = \frac{\dfrac{I_{PC,measured}}{V_{bias}}}{f_{THz} \int_{T_{THz}}^{2T_{THz}} G_{sCW}(t, C2 = 1)dt} \qquad (2.50)$$

It is reported in [6] that for a dipole antenna driven by photomixer which is deposited on LT-GaAs layer, a 30 V DC bias is applied to the arms of the dipole, and an average current value of 70 µA was measured. By using these values we obtain and average antenna gap resistance of $\frac{30V}{70\mu A} = 430$ kΩ. When we put this value in the numerator of the equation (2.50) and and find the C2 value for the correct parameters substituted, we obtain a C2 value of $5,5254 x 10^{15}$. By using the obtained C2 in the equation (2.48), time-dependent behavior of the antenna gap conductance is obtaine as in Figure 2.28. As it can be seen in the figure, the maximum and minimum values of the conductivity are 3.122 $\mu\Omega^{-1}$ (320 kΩ) and 1.263 $\mu\Omega^{-1}$ (792 kΩ), respectively.
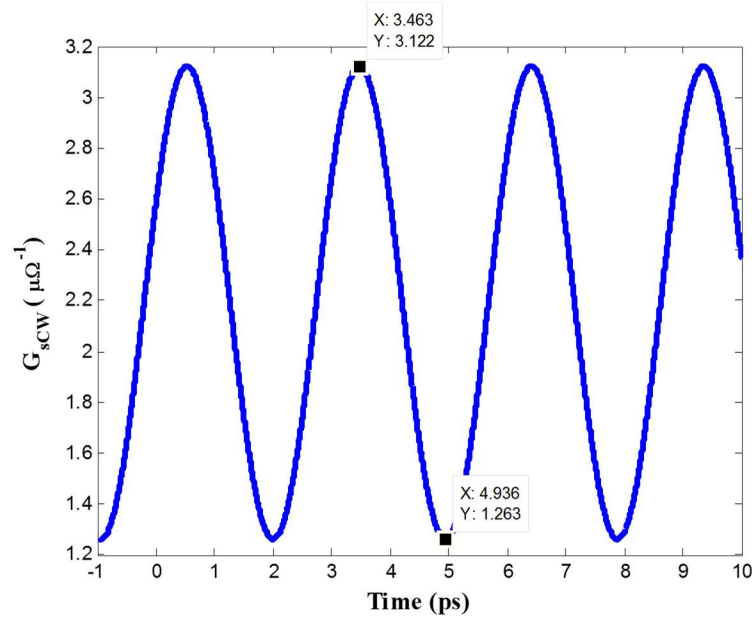
Figure 2.28 Variation of the time-dependant conductance of the photomixer antenna gap.

2.11 Tuning of the Laser Frequencies for Heterodyning

For photomixing process, two laser sources are overlapped at slightly different frequencies to obtain a difference frequency in the THz region. As a result, two laser beams are modulated in a way that the total incident laser power includes ω_1, ω_2, and $\omega_1 - \omega_2$ components. After these components hit to the surface of the LT-GaAs layer and excited the carriers in the material, higher frequency components are naturally filtered due to the intrinsic properties of the material itself. So, we expect to obtain a radiation at the difference frequency at the output. For this to happen systematically, one of the laser frequency is fixed at about 800 nm (375 THz), and the other is tuned to give a desired difference as an ouput. By using the simple formulation given below, the tuned laser beam should be adjusted to radiate at a wavelength of 800,7 nm to obtain 340 GHz at he output.

$$f_{THz} = f_2 - f_1 = \frac{c(\lambda_2 - \lambda_1)}{\lambda_2 + \lambda_1}$$

$$\lambda_2 = \frac{c\lambda_1}{c - \lambda_1 f_{THz}}$$

(2.51)

The simple equation in (2.51) gives the wavelength of the tuned laser beam for three different THz frequencies.

Table 2.4 Possible laser frequencies for three different frequencies

λ_1 (nm) Wavelength of the constant frequency laser	f_{THz} (THz) Generated THz frequency	λ_2 (nm) Wavelenth of the tuned laser	f_2 (THz) Frequecy of the tuned laser
	1	802.1	374.66
800	550	801.2	374.45
	340	800.7	374.66

2.12 Parametric Analysis of the Instantaneous and Average Source Conductance of the Photoconductive Antenna Driven By Photomixer

The high value of photomixer source resistance (430 kΩ) when it is compared to the antenna input resitance of a dipole antenna (27 Ω) results in severe mismatch between the antenna input and the source. This severe mismatch reduces effectively the power transmitted from source to the antenna arms. It is concluded that the proximity of the antenna input resistance and the source resistance should be high as much as possible. There are two possible ways to obtain a high proximity between the antenna and the source:

- Trying new antenna geometries other than the dipoles so that the input resistance of the antenna should be in the orter of KΩs.

- Looking for a new laser, antenna gap, and the semiconductor parameters as formulated in (2.48) that dereases the source resistance as much as possible.

In this section, the effect of the parameters which are formulated in (2.48) on the instantaneous and average conductance will be examined.

(a)

(b)
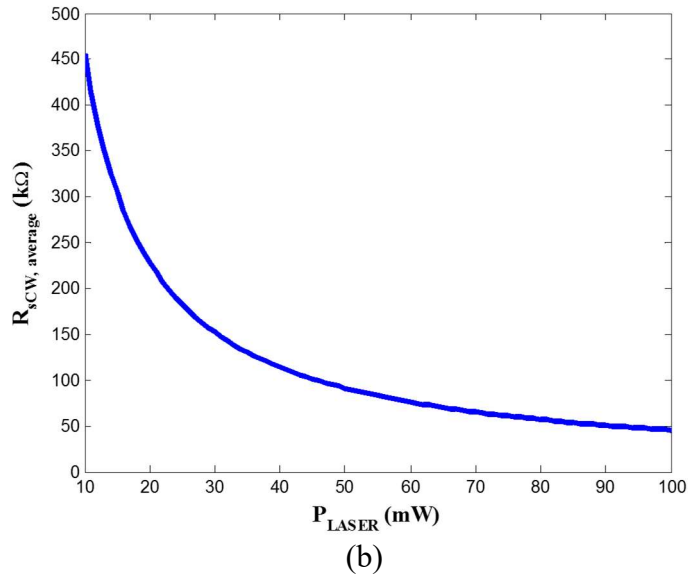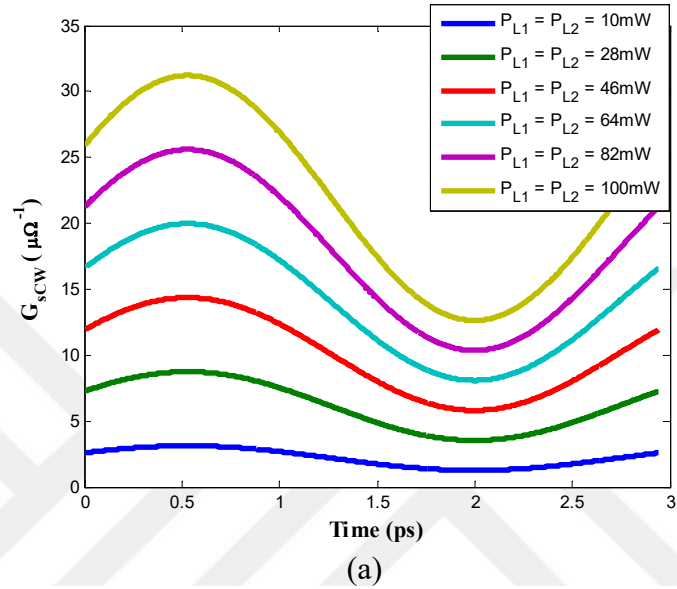
Figure 2.29 For varying laser output power levels (a) time-dependent behavior of the antenna conductance over one period at 340 GHz, (b) average source resistance change. ($f_{THz} = 340\ GHz\ L = W = 10\ \mu m, t_{GaAs} = 1\ \mu m, \tau_C = 1\ ps, \mu_n = 1000\frac{cm^2}{Vs}, m = 1$)
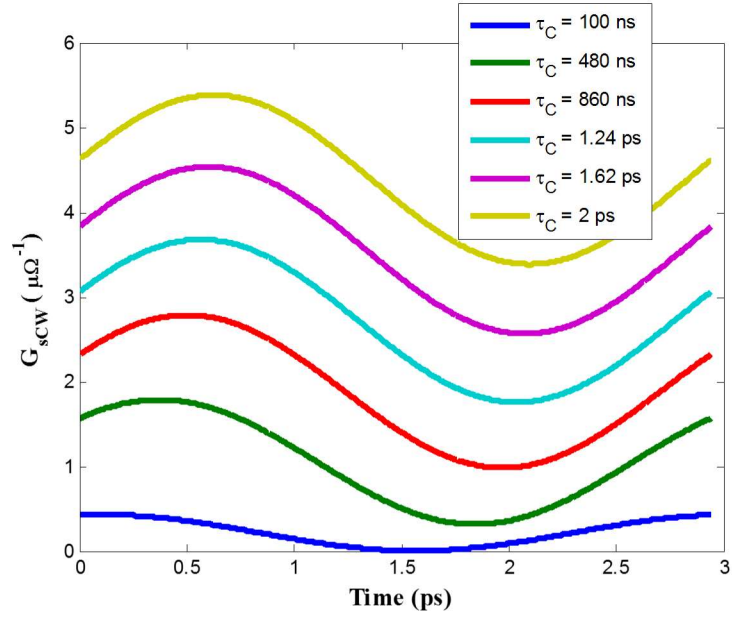
(a)
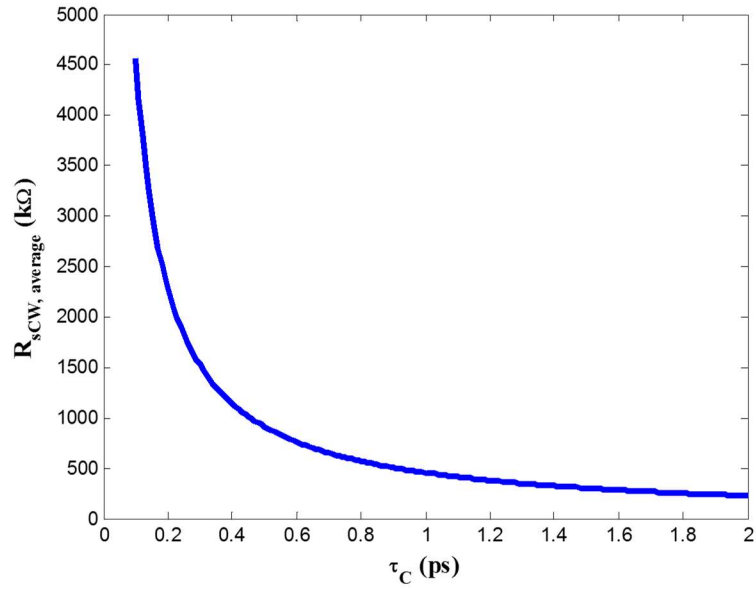
(b)

Figure 2.30 For varying carrier lifetime (a) time-dependent behavior of the antenna conductance over one period at 340 GHz, (b) average source resistance change. ($P_{L1} = P_{L2} = 10$ mW, $f_{THz} = 340$ GHz, $L = W = 10$ μm, $t_{GaAs} = 1$ μm, $\mu_n = 1000 \frac{cm^2}{Vs}$, $\alpha = 6000$ cm^{-1}, $m = 1$)
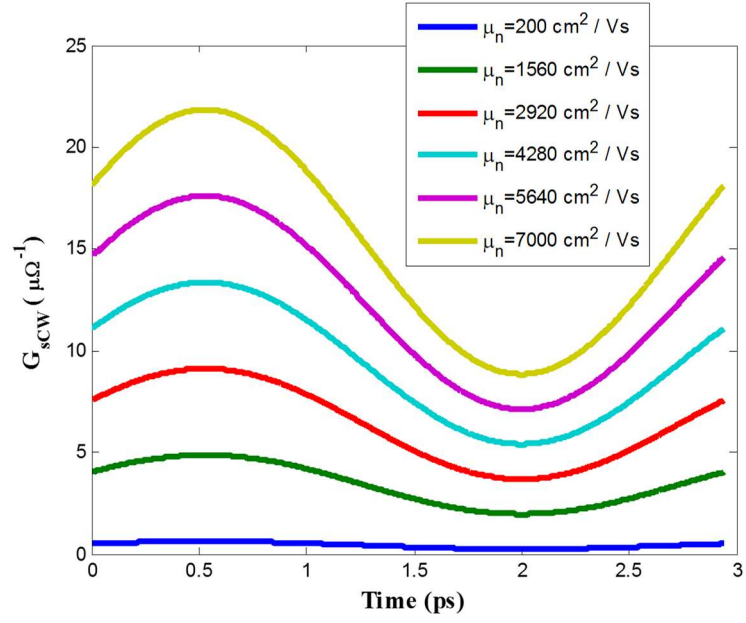
(a)
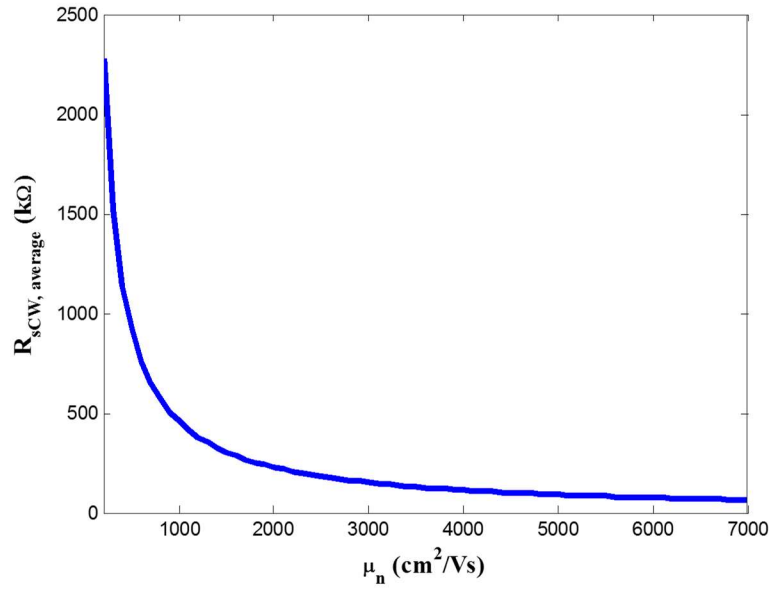
(b)

Figure 2.31 For varying electron mobility (a) time-dependent behavior of the antenna conductance over one period at 340 GHz. (b) average source resistance change. ($P_{L1} = P_{L2} = 10$ mW, $f_{THz} =$ 340 GHz, $L = W = 10$ μm, $t_{GaAs} = 1$ μm, $\mu_n = 1000 \frac{cm^2}{Vs}$, $\alpha = 6000$ cm^{-1}, m = 1)

(a)

(b)

Figure 2.32 For varying absorbtion coefficient of PC material (a) time-dependent behavior of the antenna conductance over one period at 340 GHz. (b) average source resistance change. ($P_{L1} = P_{L2} = 10$ mW, $f_{THz} = 340$ GHz, $L = W = 10$ μm, $t_{GaAs} = 1$ μm, $\tau_C = 1$ ps, $\mu_n = 1000 \frac{cm^2}{Vs}$, $m = 1$)

(a)

(b)

Figure 2.33 For varying length of the antenna gap (a) time-dependent behavior of the antenna conductance over one period at 340 GHz. (b) average source resistance change. ($P_{L1} = P_{L2} = 10$ mW, $f_{THz} = 340$ GHz, $W = 10$ μm, $t_{GaAs} = 1$ μm, $\tau_C = 1$ ps, $\alpha = 6000$ cm^{-1}, $\mu_n = 1000 \frac{cm^2}{Vs}$, $m = 1$)
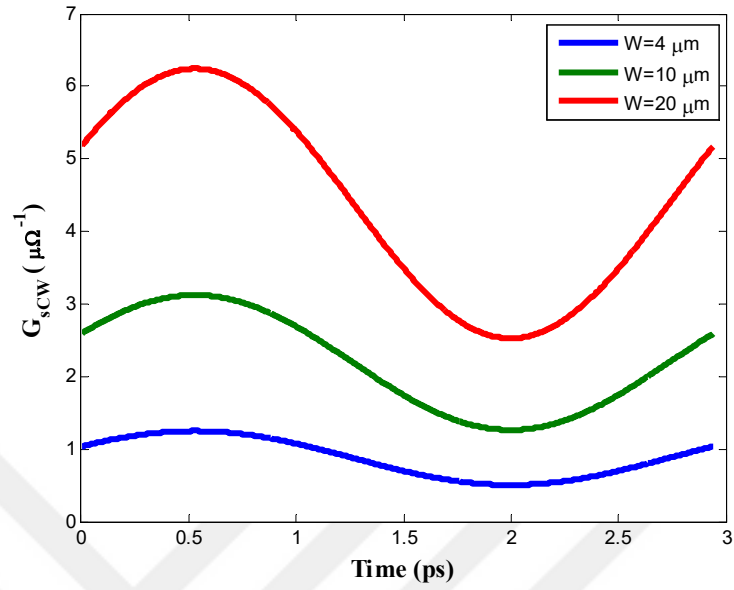
(a)
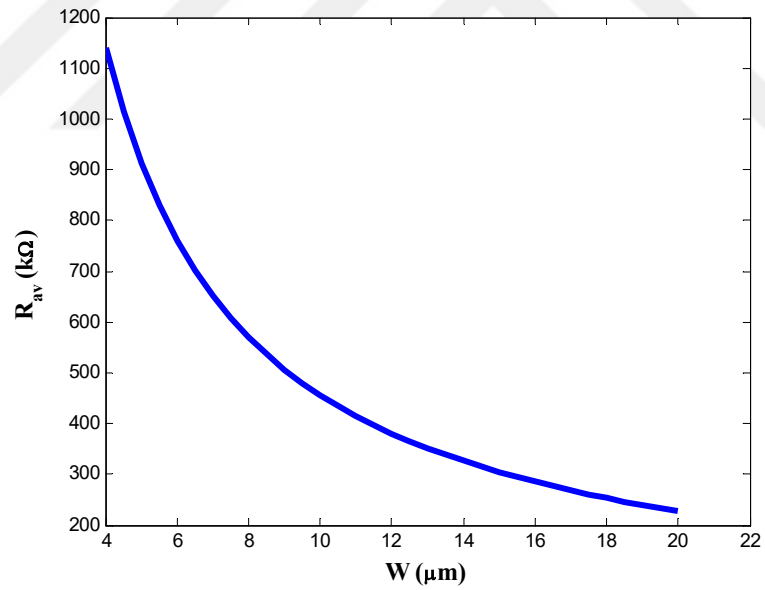
(b)

Figure 2.34 For varying antenna gap width (a) time-dependent behavior of the antenna conductance over one period at 340 GHz. (b) average source resistance change. ($P_{L1} = P_{L2} = 10$ mW, $f_{THz} = 340$ GHz, $L = 10$ μm, $t_{GaAs} = 1$ μm, $\tau_C = 1$ ps, $\alpha = 6000$ cm^{-1}, m = 1)
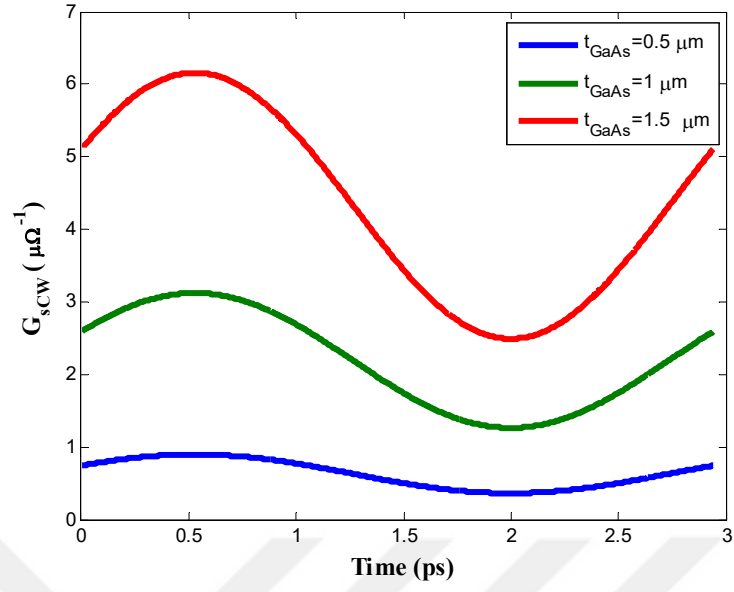
(a)
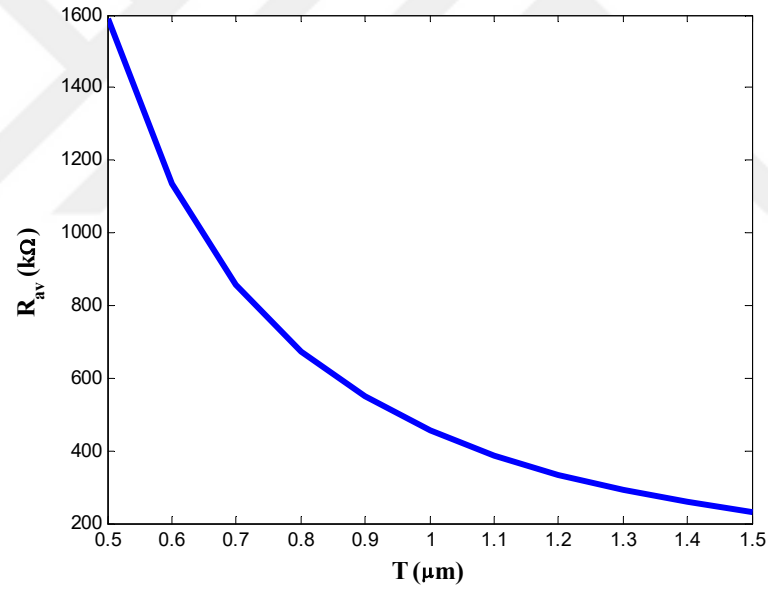
(b)

Figure 2.35 For varying LT-GaAs thickness (a) time-dependent behavior of the antenna conductance over one period at 340 GHz. (b) average source resistance change. ($P_{L1} = P_{L2} = 10$ mW, $f_{THz} = 340$ GHz, $L = W = 10$ μm, $\tau_C = 1$ ps, $\alpha = 6000$ cm^{-1}, $\mu_n = 1000 \frac{cm^2}{Vs}$, $m = 1$)
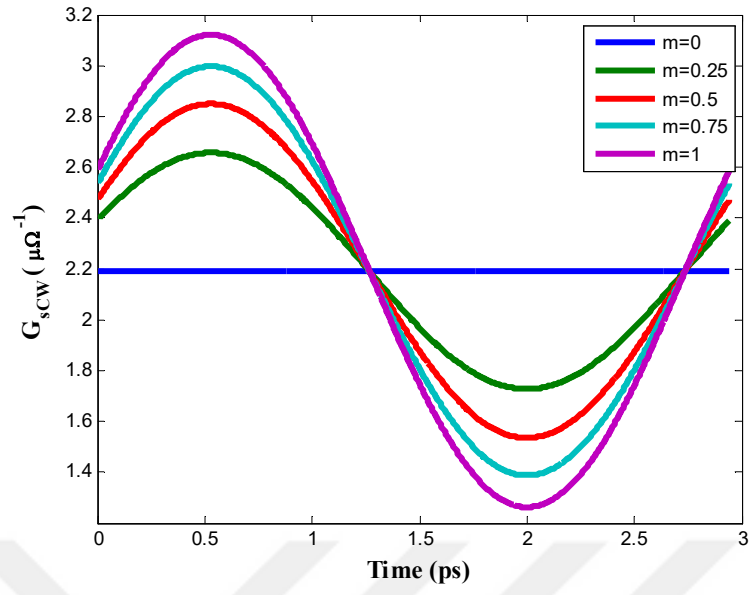
(a)
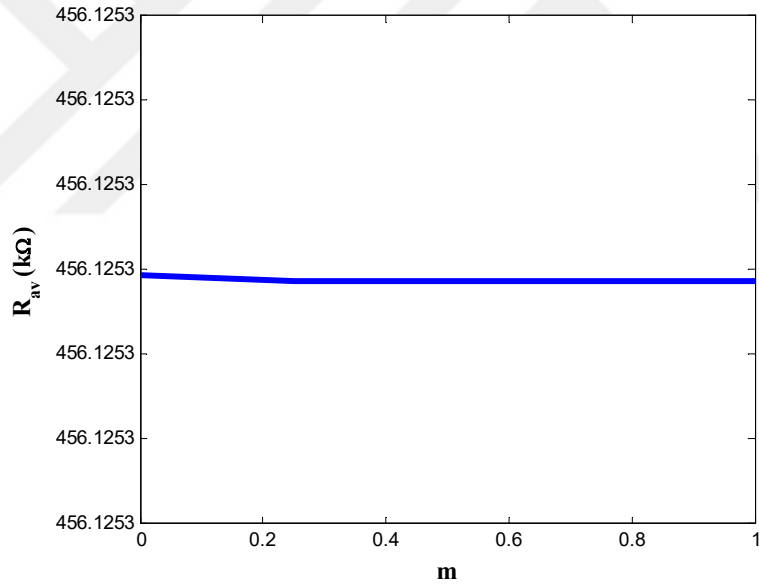
(b)

Figure 2.36 For varying mixing efficiency (a) time-dependent behavior of the antenna conductance over one period at 340 GHz. (b) average source resistance change. ($P_{L1} = P_{L2} = 10$ mW, $f_{THz} = 340$ GHz, $L = W = 10$ μm, $t_{GaAs} = 1$ μm, $\tau_C = 1$ ps, $\alpha = 6000$ cm^{-1}, $m = 1$)

CHAPTER 3

DESIGN OF TERAHERTZ ANTENNAS

3.1 Design of the Antenna Geometry

In this section, photoconductive antennas operating at 340 ve 550 GHz will be designed. For a design starting point for the dipole antenna implemented on a substrate of dielectric constant, ϵ_r, we need an effective wavelength, λ_{eff}, to decide the dipole length at a specific frequency of operation. First, we need the effective dielectric constant of the medium as [9]:

$$\epsilon_{eff} = \left(\frac{\lambda}{\lambda_g}\right)^2 \tag{3.1}$$

where λ is the free space wavelength, and λ_g is the guided wavelength of the medium. If we know the operation frequency and the effective guided wavelength obtained either by the simulations or from the experimental results, we can obtain the effective permeability of the medium. Here, running a simulation is a good starting point as a design point of view. However, before starting the simulations we need an initial value for the antenna geometry that gives a resonance frequency around the desired frequency, so we can optimize these geometrical parameters later by tuning the structure. So, to design a half-wavelength dipole antenna, we need the guided wavelength from (3.1), and guided wavelength needs the knowledge of effective dielectric constant of the medium. In this regard, quasi-static approach gives an estimate number about the initial dielectric constant of the medium and an exact interval in which the antenna length will be taking during the optimization [10].

$$\epsilon_{eff} = \frac{1 + \epsilon_r}{2} \tag{3.2}$$

Since we are using GaAs as the antenna substrate, we have $\epsilon_r = 12.9$, So, from equation (3.2) we get an effective dielectric constant, $\epsilon_{eff} = 6.95$.

As the design specification, we are aiming two different antennas operating at frequencies, 340 GHz and 550 GHz. So, using the above expressions, we can obtain Table 3.1. Then, we run a simulation using these values. However, the simulation results have shown that there was a difference between the calculated and simulated resonant frequencies. While we have calculated a half-wave dipole antenna length of 167 μm at 340 GHz, it was found in simulations that we had a resonance frequency of 295 GHz for this length as seen in Figure 3.1. As we will see in the following sections quasi-static wavelength calculations just give an idea about the initial length but does not satisfy the calculated frequencies and needs to be optimized. But, now we will continue to analyze the antenna with the current values calculated for the quasi-static case until deciding what to do to, to design a photoconductive antenna at an exact demanded frequency of operation.

Table 3.1 Physical lengths of half-wavelength dipole antennas by using quasi-static approach for 340 GHz, and 550 GHz.

f_0(GHz)	ϵ_{eff} ($\epsilon_q = 6.95$)	λ_0 (μm)	$\lambda_{eff,GaAs}$ (μm)	$\dfrac{\lambda_{eff,GaAs}}{2}$ (μm)
340	6.95	882.4	334.7	167.3
550	6.95	545.5	206.9	103.5

The initial values of the dipole antenna lengths were given in Table 3.1. The length of the antenna metal part is the result of quasi static approximation. The depth of the antenna metal part were decided by the general knowledge obtained from the papers. But, we should know that, the width has an important effect on the antenna input resistance. As we make the width of the antenna narrower, resonance value of the input resistance becomes sharper and higher. The metal thickness was chosen so as to be feasible for an antenna production under the clean room facilities.

Antenna metal part	$167\mu m \; x \; 10\mu m \; x \; 0.2\mu m$
Photoconductive gap	$10\mu m \; x \; 10\mu m$
GaAs substrate	$900\mu m \; x \; 900\mu m \; x \; 500\mu m$

The simplest antenna structure which is designed to be operated at 340 GHz is shown in Figure 3.1.
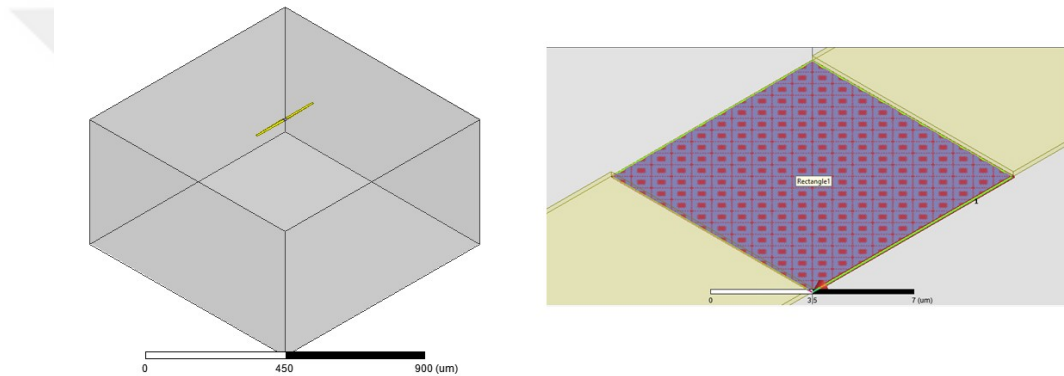
Figure 3.1 The simulated antenna structure and close view of the lumped port excitation

As Figure 3.2 also confirms that the current density distribution is in the form of a half wavelength which makes a peak at the center decreases through the ends of the dipole.
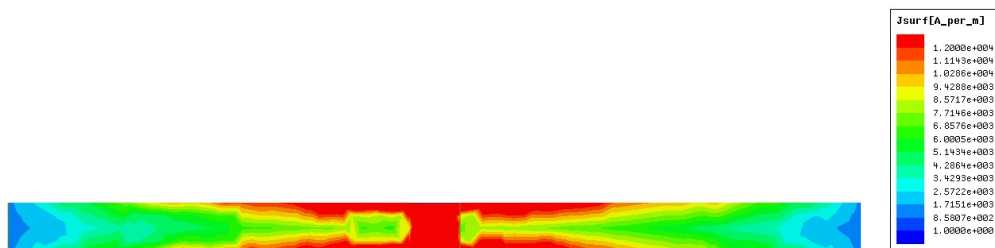
Figure 3.2 Magnitude of the surface current density of the antenna, L=167um

The real part of the input impedance of a dipole antenna is a strong function of the dielectric property of the substrate material which is approximated as [6]:

$$R_{in} \approx \frac{R_o}{\sqrt{\epsilon_{eff}}}$$

(3.3)

where R_0 is the input resistance of the antenna in free space. Resonant input impedance of a half wave dipole antenna is approximately **73 Ω** [11, p. 110]. Hence, the input resistance of the dipole on a GaAs substrate is found to be to **27 Ω** from (3.3). To see what is happening at matched port impedances, we have run simulation by using HFSS [12]. The antenna material is chosen as gold, which is deposited on a GaAs substrate. The antenna was fed with a lumped port through a rectangle plane at the gap as shown in Figure 3.1. The port impedance is taken as **27 Ω** to match port resistance to antenna input resistance, and all modes are renormalized to port impedance.
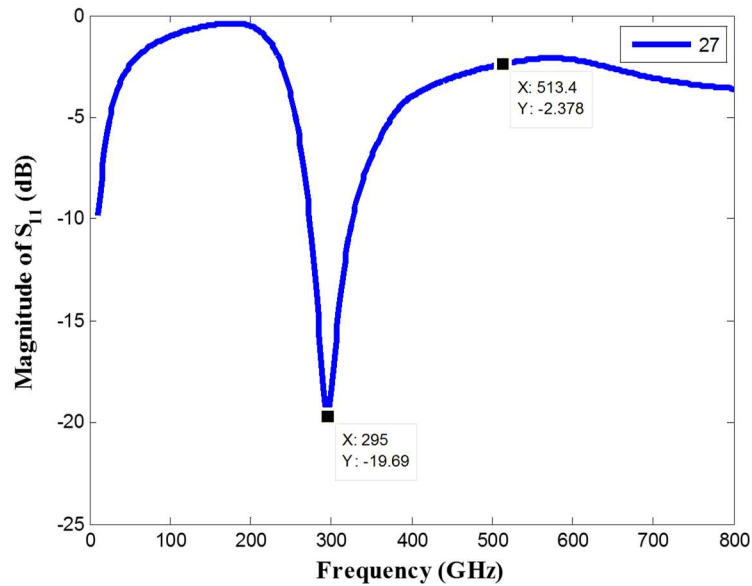
Figure 3.3 Reflection coefficient for matched (27 Ω) port resistance

The plots of the real and imaginary parts of the input impedance of the antenna for matched case are shown in Figure 3.4. These plots gives some valuable results to determine the operation frequency of the antenna:

- First of all, the calculated value for input resistance from the general formula for dipoles on substrate given in (3.3) agrees very well with the simulated input resistance at resonance, which are **27Ω**, and **32Ω**, respectively.
- Secondly, the input reactance is almost zero at the resonance frequency of **295 GHz**.
- Thirdly, we observe another frequency point which is higher than the resonance frequency at which the maximum input resistance occurs and has a zero reactance but with a very high reflection coefficient. The significance of this point lies under the fact that at very high port impedances ($\geq 1K\,\Omega$), it will be constituting our antenna operation frequency as a photomixer as we will see later in this section.
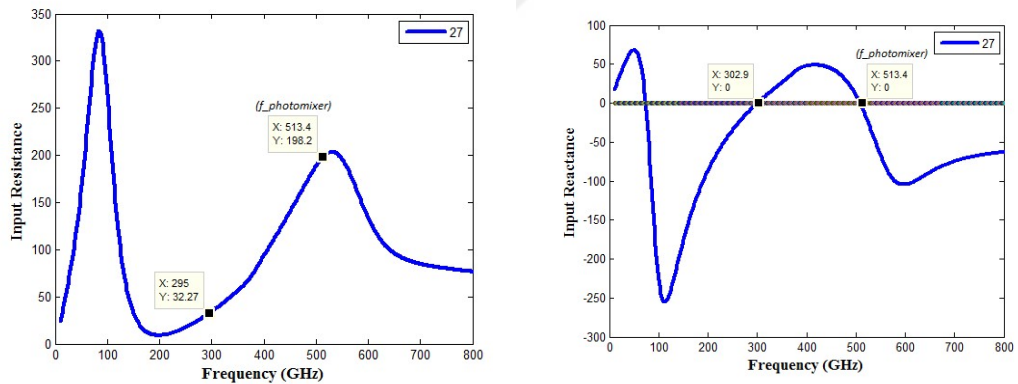
Figure 3.4 Input resistance and input reactance of the matched antenna

3.2 The Antenna Mismatch and Necessity for High Input Impedance

As it is calculated in Chapter 2, the small value of antenna input resistance, **27Ω**, presents a severe mismatch to very high source resistance photomixers. To see the

results of this phenomena, resistance of the port, which corresponds to source resistance in equivalent model is increased gradually from 27 Ω to 10KΩ, and simulated in HFSS [12] for the antenna structure given in Figure 3.1. We can see the results for the reflection coefficient change for each distinct port resistance from 200GHz to 800GHz. For 27Ω, we observe the smallest reflection value at **278 GHz** which is the natural resonance frequency of the antenna.

(a)   (b)
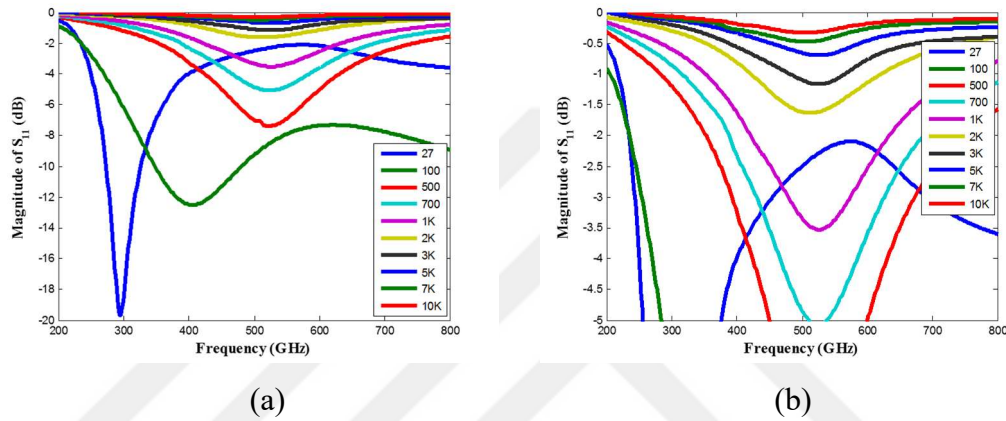
Figure 3.5 (a) Reflection coefficient for the antenna driven by different source resistances starting from 27Ω to 10K Ω. (b) More closed view of the figure in.

As we increased the port resistance, we have observed the following effects. First, the value of the reflection coefficient increased qaudratically, and the dip points for S11 became smoother from 27Ω to 10K Ω port resistances. To be able to observe this effect better, reflection and frequency values for the dip points were tabulated in Table 3.3, and plotted. Secondly, the resonance frequency rose sharply from matched 27Ω to 100Ω port resistance, then fluctuated slightly around the same frequency of 513 GHz which was the point at which the input reactance became zero and input resistance was at its peak. Since, a photomixer type antenna also has a source resistance values in the order of kΩs, we can assume this point as the operation frequency for such antennas.

Table 3.3 Dip values for the reflection coefficient for different port resistances

Port Resistance (Ω)	27 (matched)	100	500	700	1K	2K	3K	5K	7K	10K
Magnitude of S_{11} (dB)	-19.7	-12.5	-7.4	-5	-3.5	-1.6	-1.2	-0.7	-0.4	-0.34
Resonance frequency (GHz)	295 (natural resonance frequency)	405.8	521.4	524.5	526.1	512	526	505	506	504
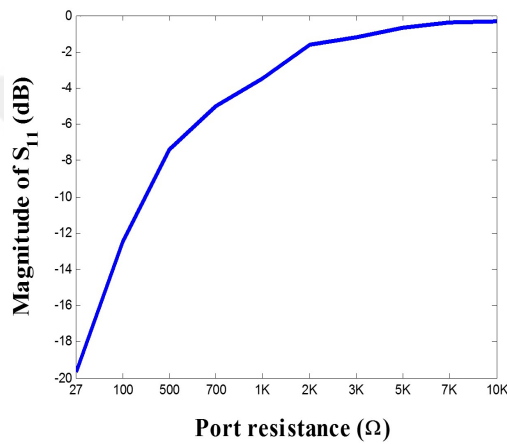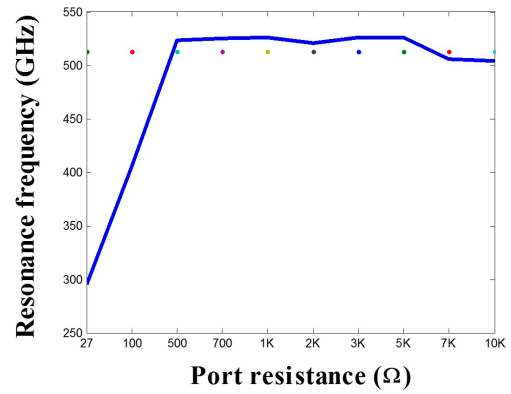
(a)   (b)

Figure 3.6 (a) Reflection coefficient change (b) Resonance frequency change of the antenna driven by different port resistances starting from 27Ω to 10K Ω.

As we can observe in Figure 3.7, since we had no change in the antenna geometry and the substrate dimensions, change in port resistance have made almost no change in the input resistance and reactance values for the antenna.
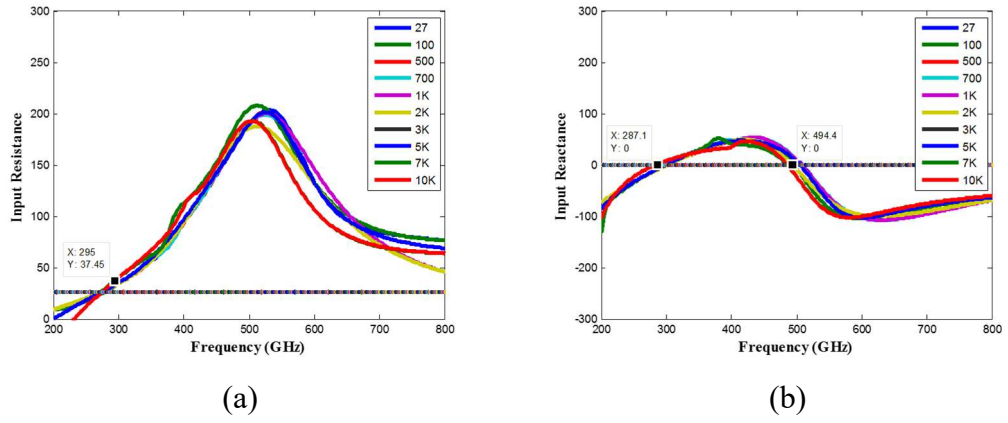
Figure 3.7 (a) Input resistance change (b) Input reactance change of the antenna driven by different port resistances starting from 27Ω to 10K Ω.

We can explain the shift in the smallest S11 frequency, and so the operation frequency, with the following basic relation between the reflection coefficient and antenna input and source resistances:

$$S_{11} = \frac{Z_s - Z_a}{Z_s + Z_a} \tag{3.4}$$

where $Z_a = R_a + jX_a$ is the input impedance of the antenna, $Z_S = R_S + jX_S$ is the source resistance (port resistance) created by the substrate material at the gap region after incidence of the light. Inserting Z_a and Z_S in to (3.4) and simplifying gives:

$$S_{11} = \frac{(R_s^2 - R_a^2 + X_S^2 - X_a^2) + j2(X_s R_a - X_a R_s)}{(R_a + R_s)^2 + (X_a + X_S)^2} \tag{3.5}$$

Taking magnitude of S_{11} we obtain the following expression:

$$|S_{11}| = \left| \frac{Z_{ant} - Z_s}{Z_{ant} + Z_s} \right| = \frac{\sqrt{(R_s^2 - R_a^2 + X_S^2 - X_a^2) + j2(X_s R_a - X_a R_s)}}{(R_a + R_s)^2 + (X_a + X_S)^2} \tag{3.6}$$

64

Since we assumed no port reactance in simulations, we took $X_S = 0$, and we know that $S_{11}(\text{dB}) = 20 \log(|S_{11}|)$. Actually, these results verified the fact that renormalization of a port to an assigned full port impedance in HFSS [12] was nothing but using equation (3.6) and taking reflections back to the port into account.
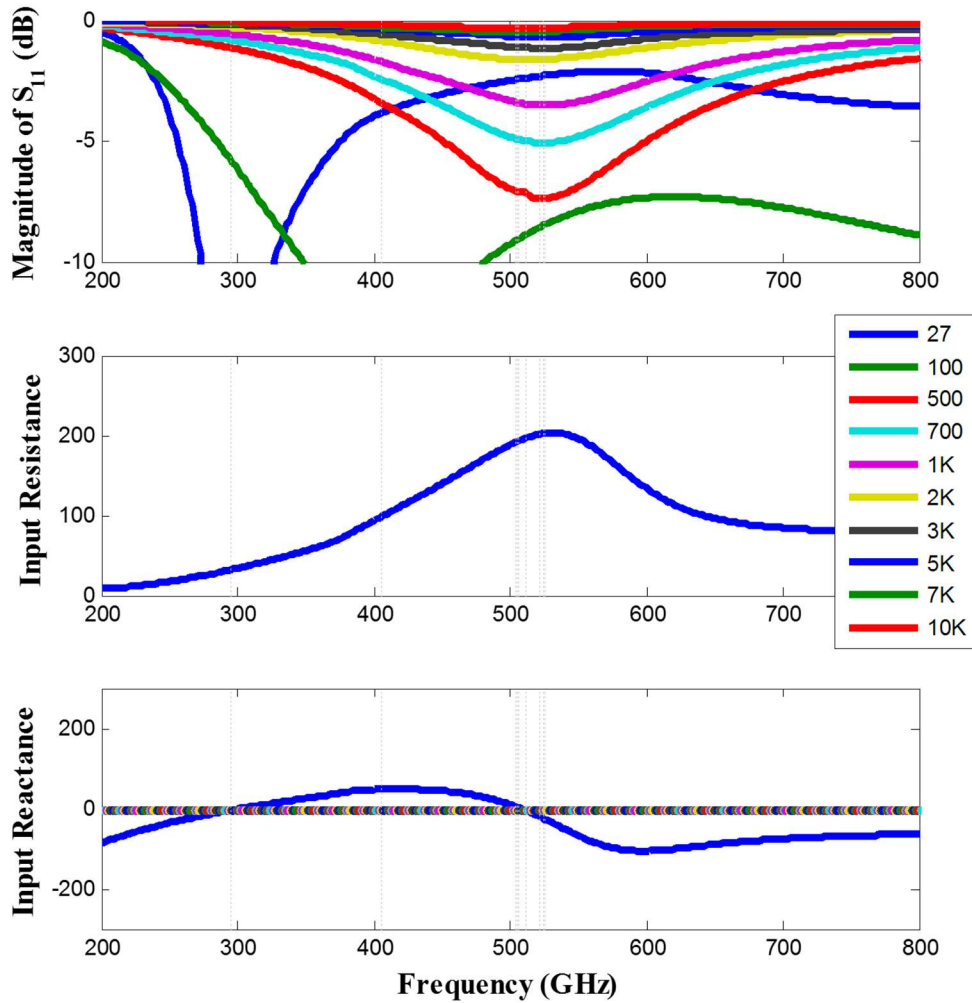
Figure 3.8 Comparison of the S_{11}, input resistance, and input reactance of the photomixer type antenna operating at 513 GHz.

3.3 Accurate Modelling of the Lens Effects for Antenna Simulations

Improving the coupling of THz wave from antenna substrate to the air is a very important step of the antenna design. Because, it is likely that the generated power at the antenna arms can have radiate in any direction other than the intended bottom side of the substrate. While some of the generated power is guided in the substrare (Figure 3.9), some of the power can make a back-scattering which is not a demanded situation. The reason for a guided mode to occur is that for the beams incident onto the bottom of the substrate which have an angle greater that the critical angle of the medium, θ_1 make multiple reflections inside the substrate borders and dissipates without having a chance to radiate.
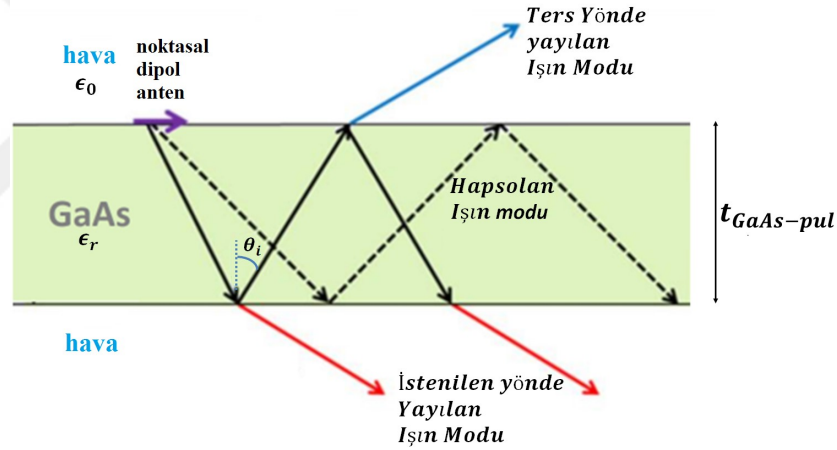
Figure 3.9 Radiated mode (solid line) and guided or surface mode (dash line) of a Hertzian dipole antenna on the semi-infinite substrate [1].

Mounting a silicon lens is a perfect solution in terms of overcoming reflections at the bottom of the antenna and for increasing the directivity of the radiatited pattern by focusing. For this purpose, a commercially available hyperhemispherical lens is mounted at bottom side of the structure with the dimensions given in Figure 3.10, and simulated in time domain in CST as shown in Figure 3.11. The time-domain solution method is preferred due to its relatively faster solution for large volume structures when compared to the frequency-domain solution method.

Photoconductive antenna	substrate	semi-insulating GaAs
	chip area	2 mm x 2 mm
	thickness t	600 µm
Hyperhemispherical lens	material	undoped HRFZ-silicon,
	specific resistance ρ	>10 kΩcm
	refractive index n	3.4
	diameter	12 mm
	height h	7.1 mm
	distance d	7.7 mm
Terahertz beam	collection angle α	57°
	divergence angle ß	15°
	virtual focus length L	26.4 mm
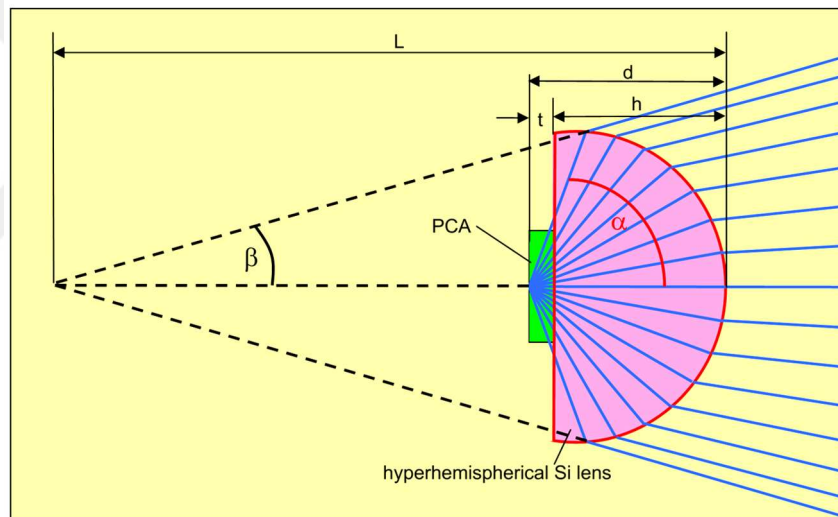
Figure 3.10 The hyperhemispherical lens parameters which is used for focusing the radiated THz signal [13]

One important point is that the mounted lens and the bottom substrate should be close enough so that the transmitted waves from the substrate should have a chance to reach silicon lens without changing its direction due to the remaining air in between. In the literature it is recorded that the gap in between should be 0.03 λ_0 (26 µm @340 GHz) at most [14].

The simulated structure for the antenna mounted on a hyperhemispherical lens and the results of the simulation is shown in Figure 3.11.

(a)

(b)

Type	Farfield
Approximation	enabled (kR >> 1)
Monitor	farfield (f=0.34) [1]
Component	Abs
Output	E-Field(r=1m)
Frequency	0.34
Rad. effic.	-1.598 dB
Tot. effic.	-7.291 dB
Emax	31.89 dBV/m
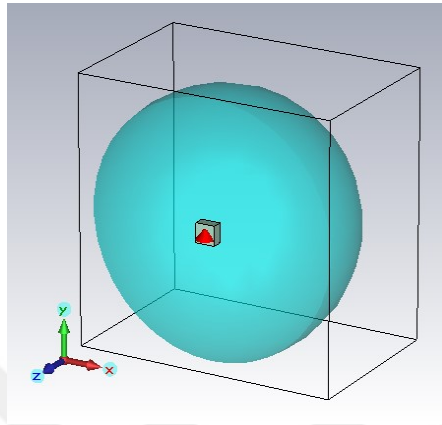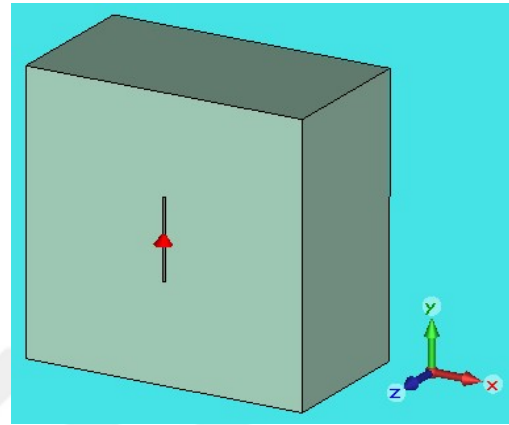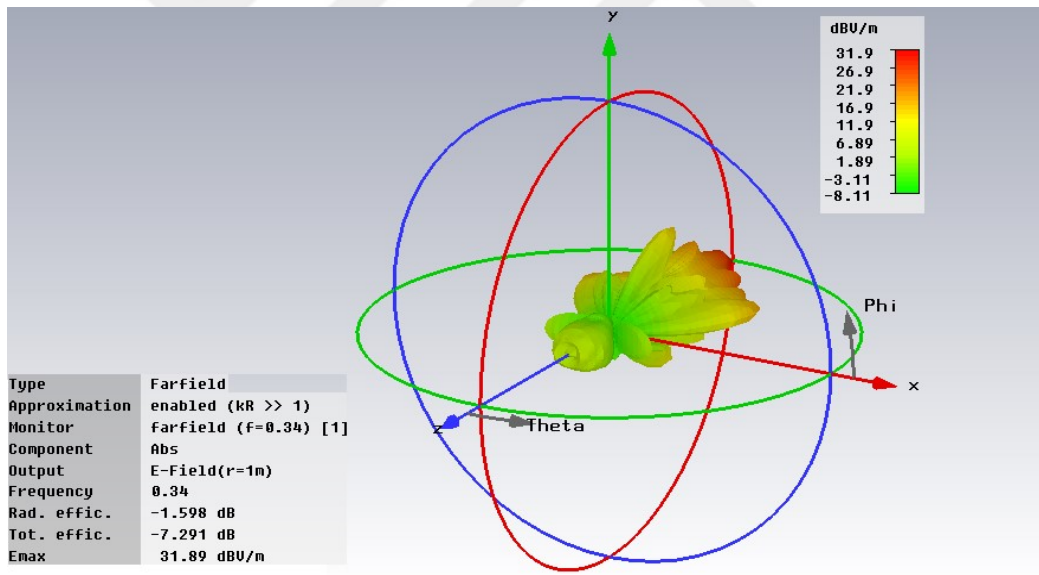
(c)
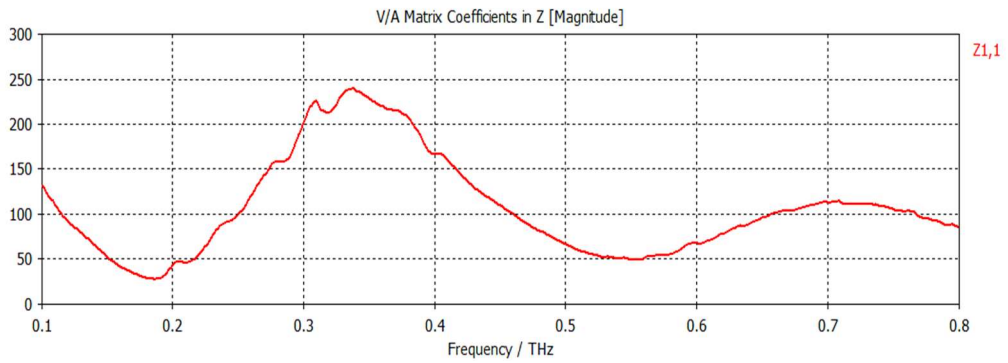
(d)

Figure 3.11 (a) The simulated geometry of a dipole antenna deposited on a GaAs substrate which is mounted on a hyperhemispherical lens (b) Closed view (c) electric field distribution of the of the antenna structure with lens (d) Antenna input impedance as a function of time which makes a peak at 340 GHz.

In the simulation results, it can clearly be seen that the radiation pattern is much more intensive in the direction of the substrate bottom as ecpected. Also, the peak of the input resistance is around 340 GHz. However, simulation of the structure with a lens which has a much larger volume than the antenna itself takes almost a day to complete. Simulating structures without using lens also gives results that is not make any senseat all. Because, without inserting a lense to the antenna, multiple reflections take place at the boundaries makes it impossible to detect operating frequency and to obtain a real antenna pattern as shown in Figure 3.12.

69
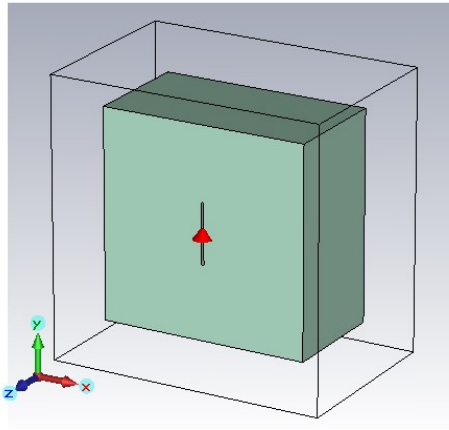
(a)
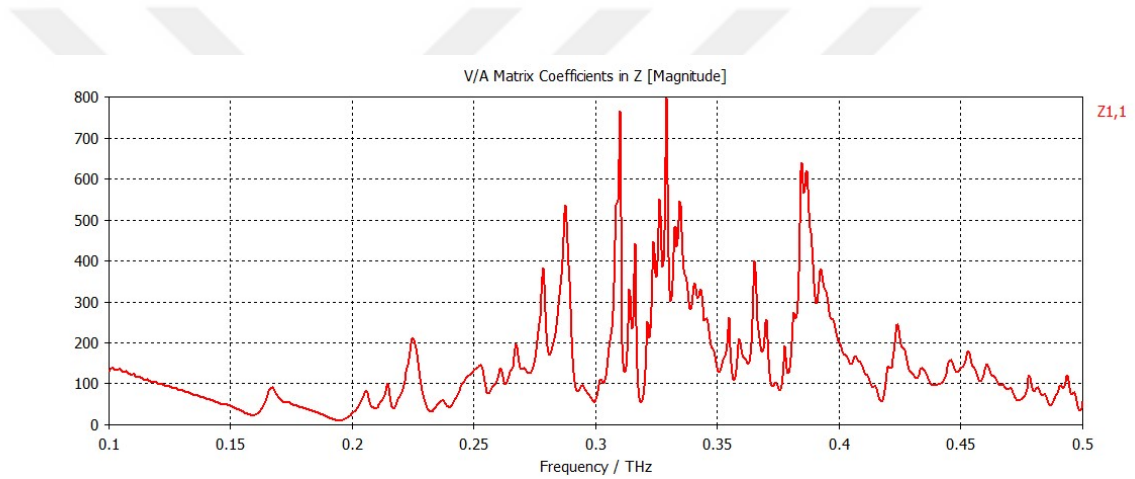
(b)

Figure 3.12 (a) The simualated geometry of the dipole antenna without lens. **(b)** Antenna input impedance as function frequency.

As a solution to the time limitation in large geometry simulations, a new technique is developed which gives a very close results to the simulations which have performed with lens. In this method, PML (perfectly matched layer) boundaries are defined at the bottom of the substrate which absorbs most of the incident field and prevent reflections. Defined PML boundaries are shown in Figure 3.13.

70

(a) antenna without lens

(b) Inclusion of the surrounding air.

(c) PML layer at the bottom

(d) PML layer

(e) infinite air.

(f) infinite air.

(g) infinite air.

(h) infinite air.

(i) infinite air.
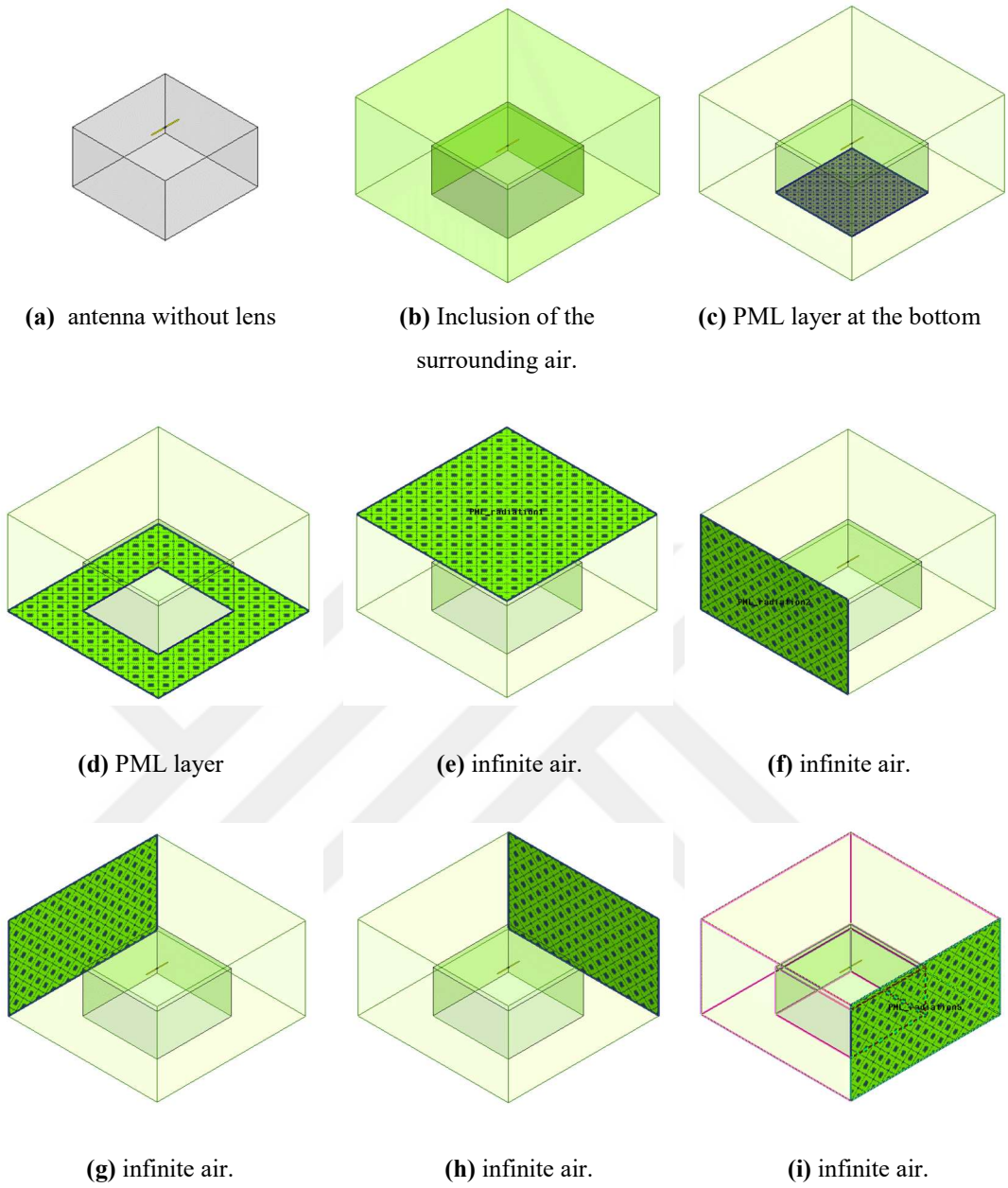
Figure 3.13 (a-i) Inclusion of the lens effect by defining PML layers at the GaAs-Lens boundary.
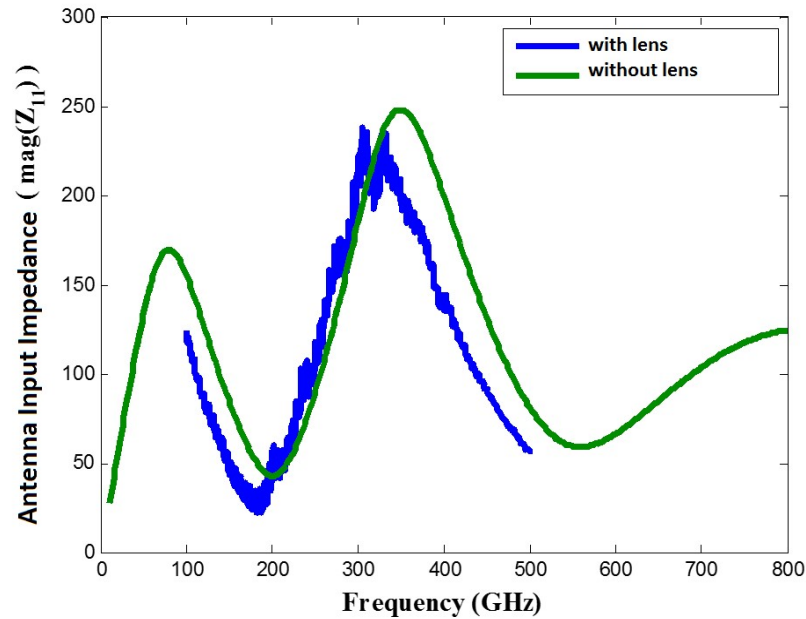
Figure 3.14 Comparison of the simulation results performed with lens in CST and without lens in HFSS with PML layers defined at the boundary.

As it can be seen in Figure 3.14, proper definition of absorbing PML surfaces makes simulations witout lens very similar to the simulations performed with lens. So, the structure with PML boundaries will be used for the following simulations.

3.4 Optimization of the Antenna Length

In this section, antenna geometries for the desired frequencies will be obtained under the illumination of the experiences obtained in the earlier simulations. For this pupose, a photomixer antenna operating at 340 GHz will be designed. As seen in Figure 3.15, the antenna length was increased from 220 µm to 320 µm and the peak values of the antenna input resistances awere observed which gives the operating frequency for the photomixer driven antenna. The value of antenna length which makes a peak at 340 GHz is decided to be as 260 µm.
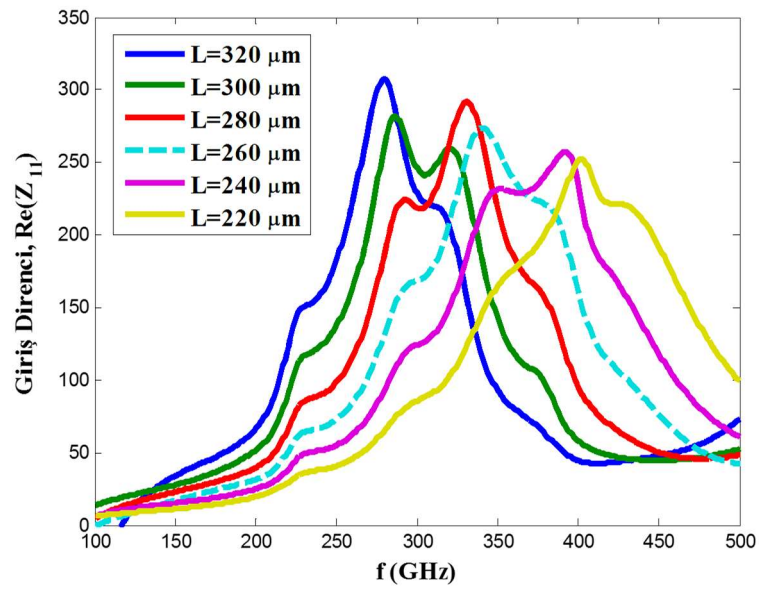
Figure 3.15 Antenna operation frequency optimization by changing the antenna length.

(a)	(b)
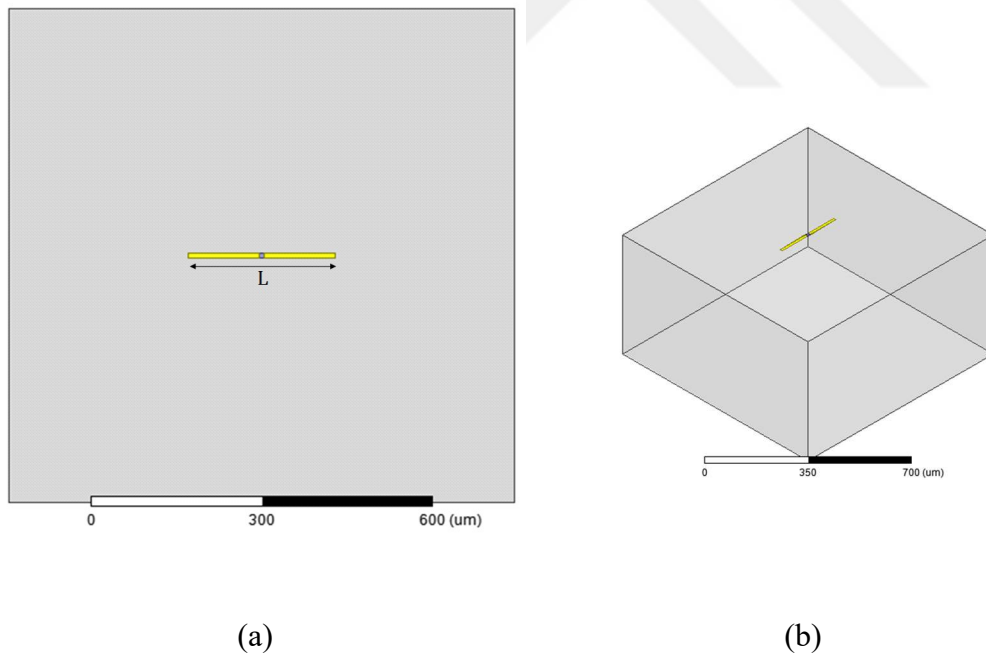
Figure 3.16 (a) top view, (b) side view of the antenna which is optimized to radiate maximum power at at 340 GHz.

3.5 Optimization of the Antenna Bias Line Positions

As the result of the incident mixed laser power onto the antenna gap region, free electron-hole pairs accelerates through the antenna metal arms under a potential difference created by the DC voltage applied on the antenna arms. For a DC voltage source to be applied onto the antenna arms, we need for a position at which the source probes make contacts to the antenna and does not disturb the antenna performance considerably. In this section, positions of the antenna bias lines were investigated. In this optimization, electrodes thinner than (3 μm) the antenna electrode (10 μm) were placed along the antenna electode and compared to the one simulated without bias lines.
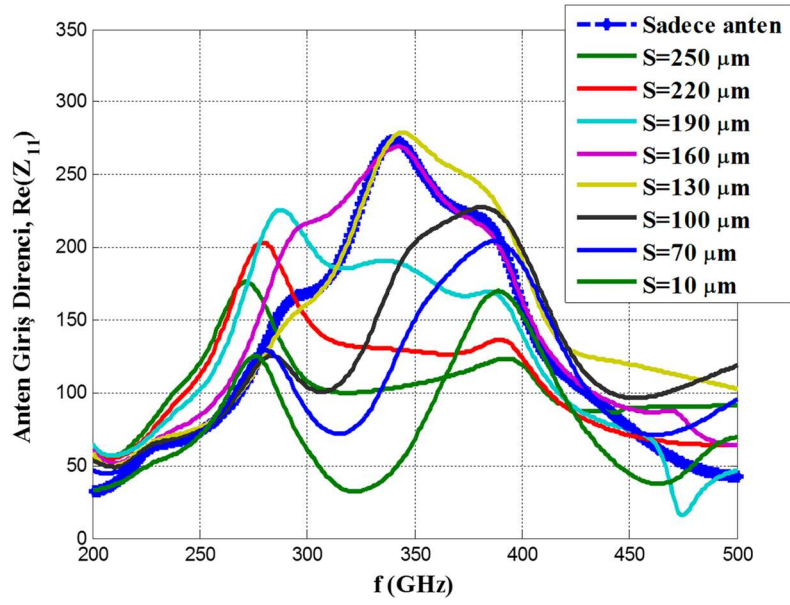
(a)
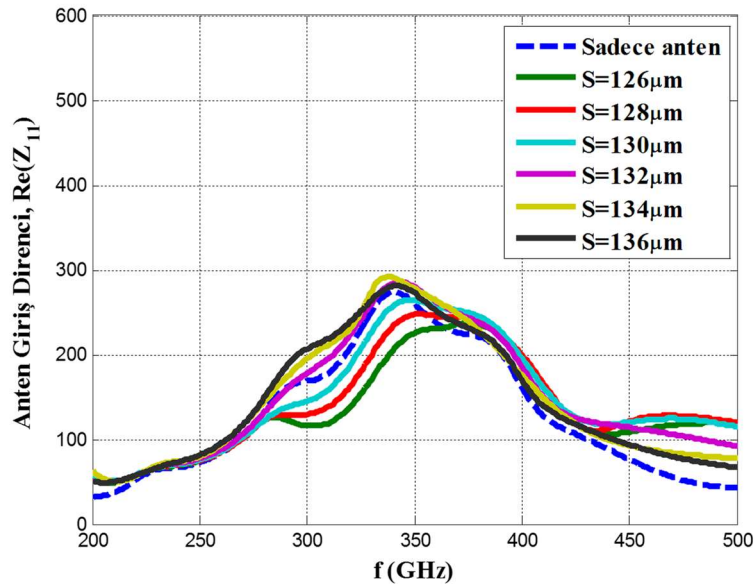
(b)

Figure 3.17 Antenna input resistance change with different distances between the antenna bias lines. (a) First optimization apllied for 30µm steps (b) Fine tuning optimization apllied for 2 µm steps.

After several simulations as shown in Figure 3.17, the distance between the striplines which is to be used as the bias line was decided as 134µm. The optimized distance, S and the final view of the antenna was shown in Figure 3.18.

(a)   (b)
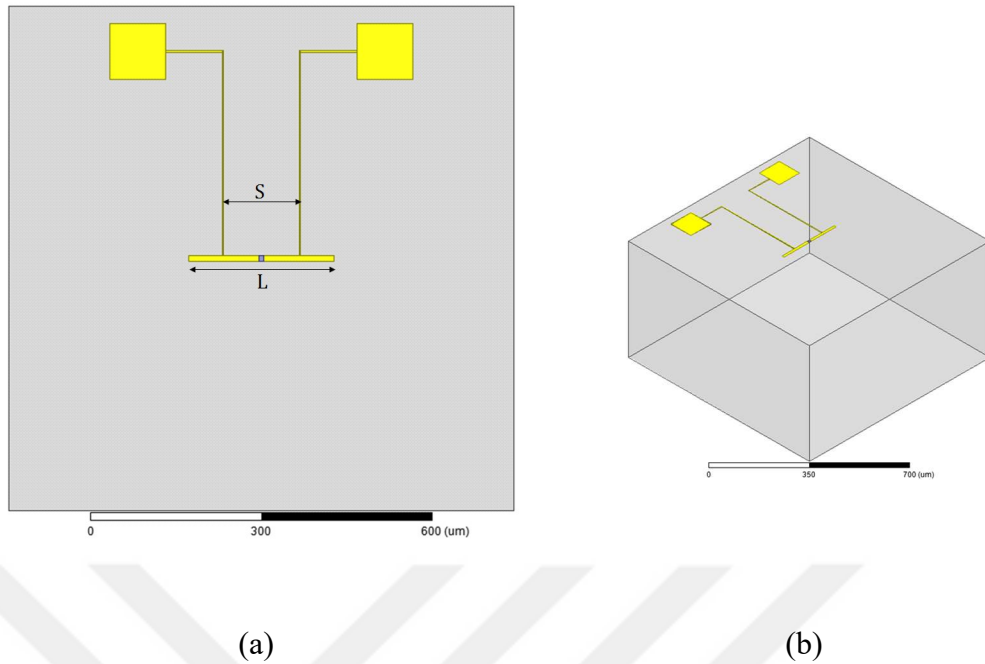
Figure 3.18 (a) Top view, (b) side view of the antenna with optimized bias lines.

The antenna structure given in Figure 3.18 was rebuilt after drawing 2D layouts, by using Coventerware simulation program. All the fabrication processes were defined and the material were chosen and deposited as being very similar to the original one. The 3D view of the rebuilt structure is shown in Figure 3.19. Here, there is an Oxide layer (pink) between the metal parts of the antenna and the GaAs susbtrate (blue). The sky blue region at the antenna gap was defined as lumped port.

(a)   (b)

76

<div align="center">(c)   (d)</div>
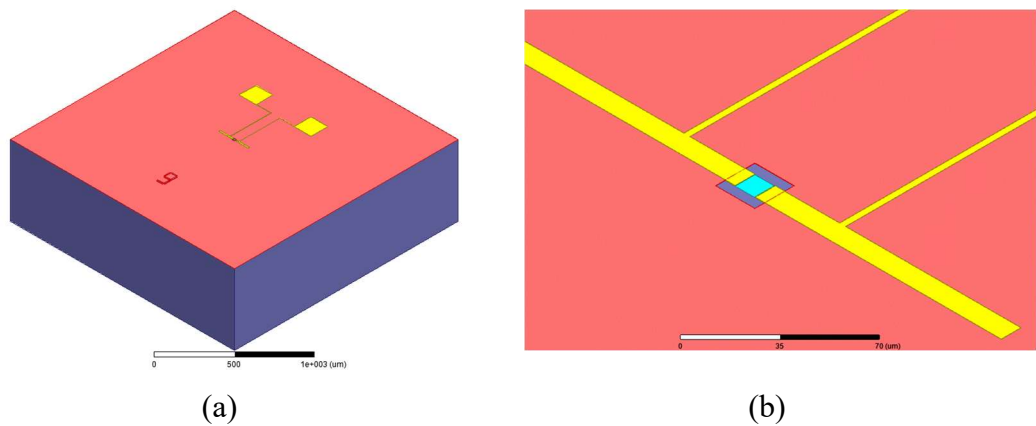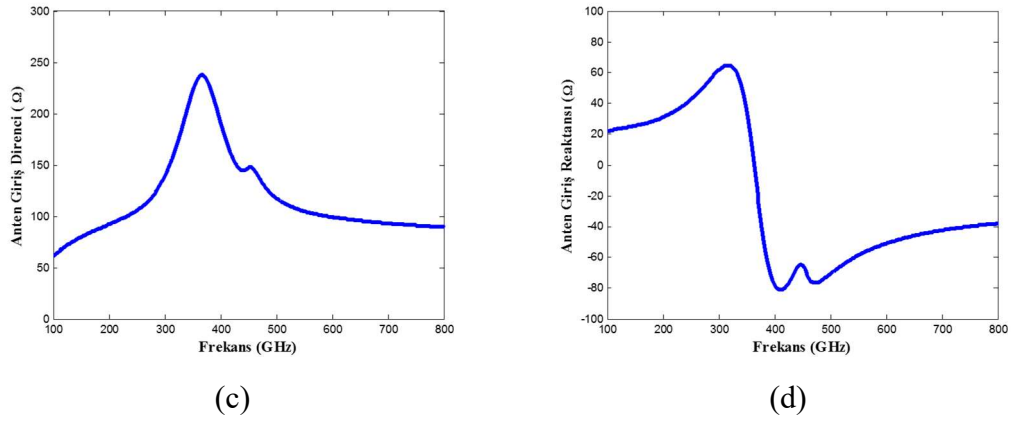
Figure 3.19 3D view of the antenna geometry which is rebuilt from its the 2D layout operating at 340 GHz. (a) side view. (b) Closed view. (c) Antenna input resistance. (d) Antenna input reactance.

Simulation results shows that the resonance frequency was shifte from 340 GHz to 380 GHz by the inclusion of Oxide layer between the antenna metal part and the GaAs layer. So, it is realized that while doing optimization for the resonance frequency, the oxide layer should also be taken into account.

When all the steps so far were repeated for an antenna which have a resonance frequency at 550 GHz, the resultant antenna length was decided as L=158.625 μm, and an optimized distance between the bias lines was found to be as 77 μm. Rebuilding the 3D structure after 2D layout file was given Figure 3.21.
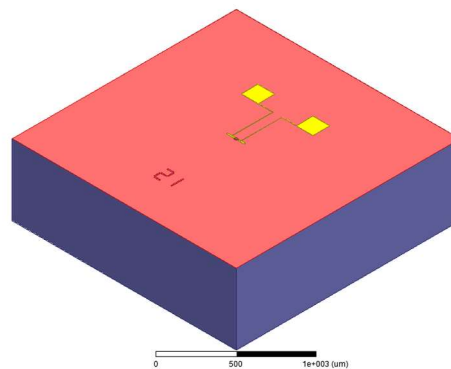
Figure 3.20 3D view of the antenna geometry which is rebuilt from its 2D layout which is operating at 550 GHz.
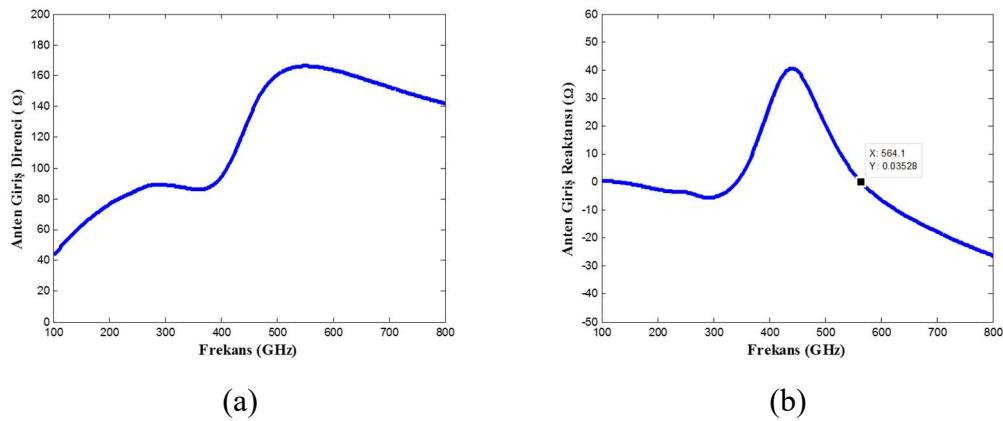
Figure 3.21 (a) Antenna input resistance. (b) Antenna input reactance.

Simulation results given in Figure 3.21 for 550 GHz antenna showed that the antenna has a resonance at 564 GHz.

3.6 Design of the Band-Stop Filter for DC Biasing of Antennas

The RF power circulating on the antenna metal structure should be isolated from the DC bias source for two reasons: First, Dc source shoul be functioning properly without being damaged by the RF power. Secondly, the bias lines should not be a part of radiating element. Because every distict part of metal length resonates at different frequencies other than the resonance frequency which means part of the power was radiated at the undesired frequencies. So, designing filter instead of simple bias lines in extension to the antenna metal parts may be good way of isolating DC source and the antenna.

In this section, theoretical modelling of the coplanar striplines will be derived as being smallest element of the filter structures and then various filters with different orders and center frequencies will be designed.

3.6.1 Theoretical Modelling of Coplanar Stripline

Figure 3.22 shows cross-sectional view of a coplanar stripline. In this figure, s shows the sistance between the lines, w shows width of a single line, t shows the thickness of the deposited metal, h shows the thickness of the GaAs substrate.

78
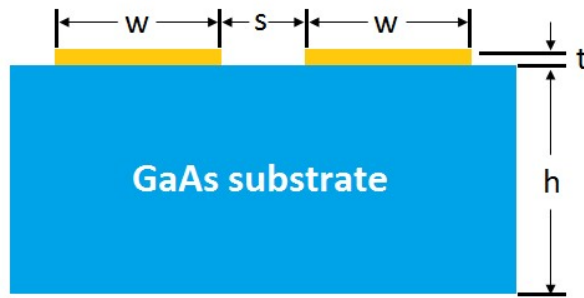
Figure 3.22 Cross-sectional view of a coplanar stripline [15]

Figure 3.23 shows the simplest transmission line model in AWR software. For a transmission line to be modeled completely, we need to know several parameters whih is also shown in the model: $\mathbf{Z_0}$ is the characteristic impedance, $\boldsymbol{\alpha}(\text{Loss})$, is the loss per unit length, $\boldsymbol{\epsilon_{eff}}$ is the effective dielectric constant, and $\mathbf{L}$ is the length of the transmission line.


```
TLINP
ID=TL48
Z0=
L=
Eeff=
Loss=
```
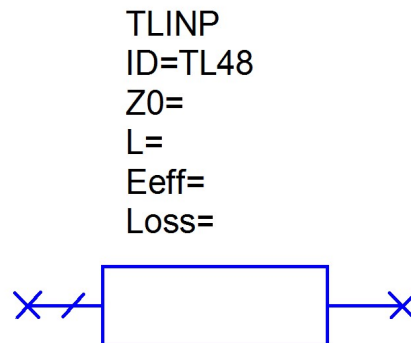
Figure 3.23 The Transmission Line model that was used to model coplanar striplines

The frequency of the first propagating non-TEM mode on the stripline is called TE_1 mode surface wave cut-off frequency and expressed by [10]:

$$f_{TE} = \frac{c}{4h\sqrt{\epsilon_r - 1}} \tag{3.7}$$

79

For small geometries of which their electrod width,w is comparable to the thickness of the electrode, t ($\frac{t}{w} = 0.04 - 0.16$), there is a need for effective value correction on s and w. These corrections are necessary for the accuracy of signal transmission speed and signal attenuation. The effective values of the s and w is expressed by [15]:

$$s = s_0 + \Delta$$
$$w = w_0 + \Delta \tag{3.8}$$

where the correction factor, Δ, is [15]:

$$\Delta = \frac{1.25t}{\pi}\left[1 + \ln\left(\frac{4\pi w}{t}\right)\right] \tag{3.9}$$

Another correction has to be made for effective dielectric constant. When we think the amount of electric field propagating in the air and semiconductor material, the portion of the wave that is propagating in air increases for a stripline with thicker electrots. And this results a decrease in effective dielectric constant of the form:

$$\epsilon'_q = \epsilon_q - \frac{1.4(\epsilon_q - 1)t/s}{\frac{K'(k)}{K(k)} + \frac{1.4t}{5}} \tag{3.10}$$

This correction is valid for $\epsilon_r \geq 9$ and $\frac{t}{w} > 0.1$.

Quasi-static effective dielectric constant for a medium of which half is occupied by the air and the other half is occupied by a dielectric material (GaAs) can be expressed by:

$$\epsilon_q = \frac{\epsilon_r + 1}{2} \tag{3.11}$$

Frequency dependent effective dielectric constant is defined by [15]:

$$\epsilon_{eff}(f) = \left[\sqrt{\epsilon_q'} + \frac{\sqrt{\epsilon_r} - \sqrt{\epsilon_q}}{\left(1 + \alpha \left[\frac{f}{f_{TE}}\right]^{-b}\right)} \right]^2 \tag{3.12}$$

$$\alpha = 10^{u \log_{10}\left(\frac{s}{w}\right) + v}$$
$$u \sim 0.54 - 0.64q + 0.015q^2$$
$$v \sim 0.43 - 0.86q + 0.54q^2 \tag{3.13}$$
$$q = \log_{10}\frac{s}{h}$$
$$b \sim 1.8$$

where

$$\begin{array}{c} K(k) \\ K'(k) \end{array} = \text{Elliptic integrals.}$$

$$K'(k) = \frac{\pi}{\ln\left[2\left(\frac{1 + \sqrt{k}}{1 - \sqrt{k}}\right)\right]} \tag{3.14}$$

$$k = \frac{s}{s + w} \tag{3.15}$$

Frequency dependent characteristic impedance of coplanar stripline is expressed by [10]:

$$Z_0 = Z_{CPS} = \frac{120\pi}{\sqrt{\epsilon_{eff}(f)}} \frac{K(k)}{K'(k)} \qquad \text{(3.16)}$$

The attenuation per unit distance due to the conductance of the electrodes is expressed as [16]:

$$\alpha_C = Re\left[\frac{Z_S}{Z_0}\right] g_2 \quad dB/m \qquad \text{(3.17)}$$

where

$Z_S(f)$ = Complex surface impedance of the conductor [16]

g_2 = Geometrical factor

$$Z_S(f) = \sqrt{\frac{1+j}{\sigma \tan(\delta)}} \coth\left\{\frac{(1+j)t}{\tan(\delta)}\right\} \qquad \text{(3.18)}$$

where

σ = 4.5x10^7 S/m, conductivity of Gold at 20C^0

$\tan(\delta)$ = Loss tangent of GaAs

$$\text{tand}(\delta) = \frac{1}{\sqrt{f\mu\sigma\pi}} \qquad \text{(3.19)}$$

$$g_2 = 17.34 \quad * \quad \left(\frac{P'}{\pi s}\right) * \left(1 + \frac{w}{s}\right)$$

$$\frac{\left(1.25 * \frac{\ln\left(4\pi\frac{w}{t}\right)}{\pi} + 1 + \frac{1.25t}{\pi w}\right)}{\left(1 + 2\frac{w}{s} + \left(\frac{1.25t}{\pi s}\right)\left(1 + \ln\left(4\pi\frac{w}{t}\right)\right)\right)^2} \qquad \text{(3.20)}$$

$$P' = \begin{cases} k\left[\left(1 - \sqrt{1-k^2}\right)(1-k^2)^{\frac{3}{4}}\right]g_1^2 & \text{for } 0 \le k \le 0.707 \\ \left[(1-k)\sqrt{k}\right]^{-1} & \text{for } 0.707 \le k \le 1 \end{cases} \qquad (3.21)$$

$$g_1 = \begin{cases} \pi\left\{\ln\left[2\dfrac{1+\sqrt{k}}{1-\sqrt{k}}\right]\right\}^{-1} & \text{or } 0 \le k \le 0.707 \\ \pi^{-1}\left\{\ln\left[2\dfrac{1+\sqrt{k}}{1-\sqrt{k}}\right]\right\} & \text{for } 0.707 \le k \le 1 \end{cases} \qquad (3.22)$$

The frequency dependent loss due to the undemanded radiation along the coplanar stripline is [15]:

$$\alpha_{rad}(f) = \pi^5 \frac{3 - \sqrt{8}}{2} \frac{\sqrt{\epsilon_{eff}}}{\epsilon_r}\left(1 - \frac{\epsilon_{eff}(f)}{\epsilon_r}\right)^2$$

$$\frac{(s + 2w)^2}{c^3 K'(k)K(k)} f^3 \quad \text{dB/m} \qquad (3.23)$$

Dielectric losses due to the dielectric properties of the GaAs is [16]:

$$\alpha_d = 27.3 \frac{\epsilon_r}{\sqrt{\epsilon_{eff}(f)}} \frac{\epsilon_{eff}(f) - 1}{\epsilon_r - 1} \frac{\tan(\delta)}{\lambda_0} \quad \text{dB/m} \qquad (3.24)$$

where

$$\lambda_0 \quad = \quad \text{Wavelength in the air}$$

The total loss per unit length is calclulated by the summation of conductor losses, radiation losses, and the dielectric losses:

83

$$\alpha_t = \alpha_C + \alpha_r + \alpha_d \qquad (2)$$

The coplanar stripline model whose frequency-dependent parameters are extracted as the formulas so far was used to design a band-stop filter by cascading as seen in Figure 3.24. Each segment has a total witdh of 14 µm and two types of s and w valued transmission lines were used to obtain a capacitive and inductive segments. The stripline model with small s ($3\mu m$) and large w ($10\mu m$) introduces a large capacitance due to the proximity of the lines and an inductance due to the length of the line. And the stripline model with large s ($10\mu m$) and small w ($2\mu m$) behaves more like as an inductive element. Each segment was chosen to have a length of quarter wavelength at the the desired band-stop frequency except the segments at the two ends have lengths of half wavelength. As a result the whole structure behaves like an RLC band-stop filter with an appropriate change in the transmission line lengths.
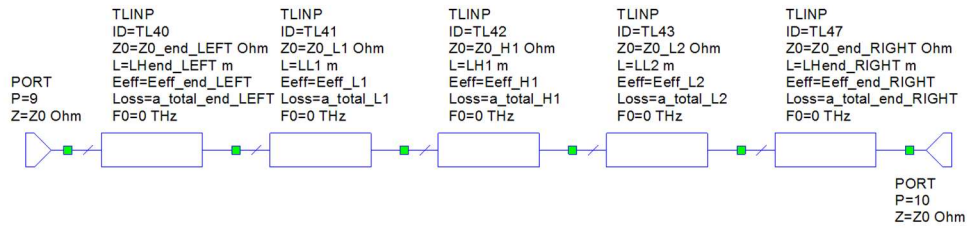
(a)
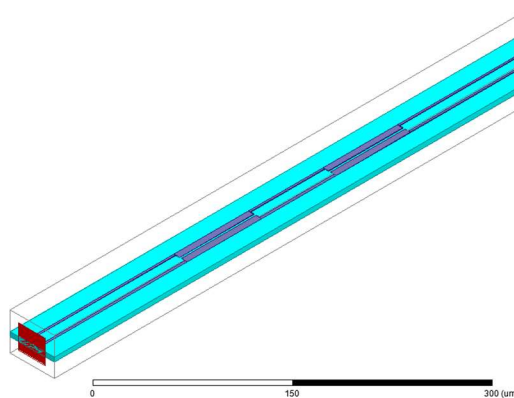
(b)

Figure 3.24 5-segment band-stop filter (a) theoretical modelling in AWR, (b) simulated geometry in HFSS

By using the derived model for CPS, various filters were designed with different number of segments and operating at different cut-off frequencies. The red planes at the ends of the filter shows the waveports. In this simulations, port resistances were chosen as 50Ω per each one. In fact, the port at the DC source side of the filter should be the input impedance of the DC source, and the port impedance at the antenna end should be the input impedance of the antenna seen at the connection point to the filter. For photomixer antennas, the input resistance is about 10KΩ, for pulsed excited photoconductive antennas, the input resistance of the antenna is about 20-30Ω. So, for a designed filter to operate properly for both photomixer and pulsed excited photoconductive antennas, these input resistance variance should also be taken into the consideration and there maybe be a need for re-design of the filters.

3.7 Design of the Band Stop-Filter for DC Biasing at 340 GHz

(a)

(b)

(c)
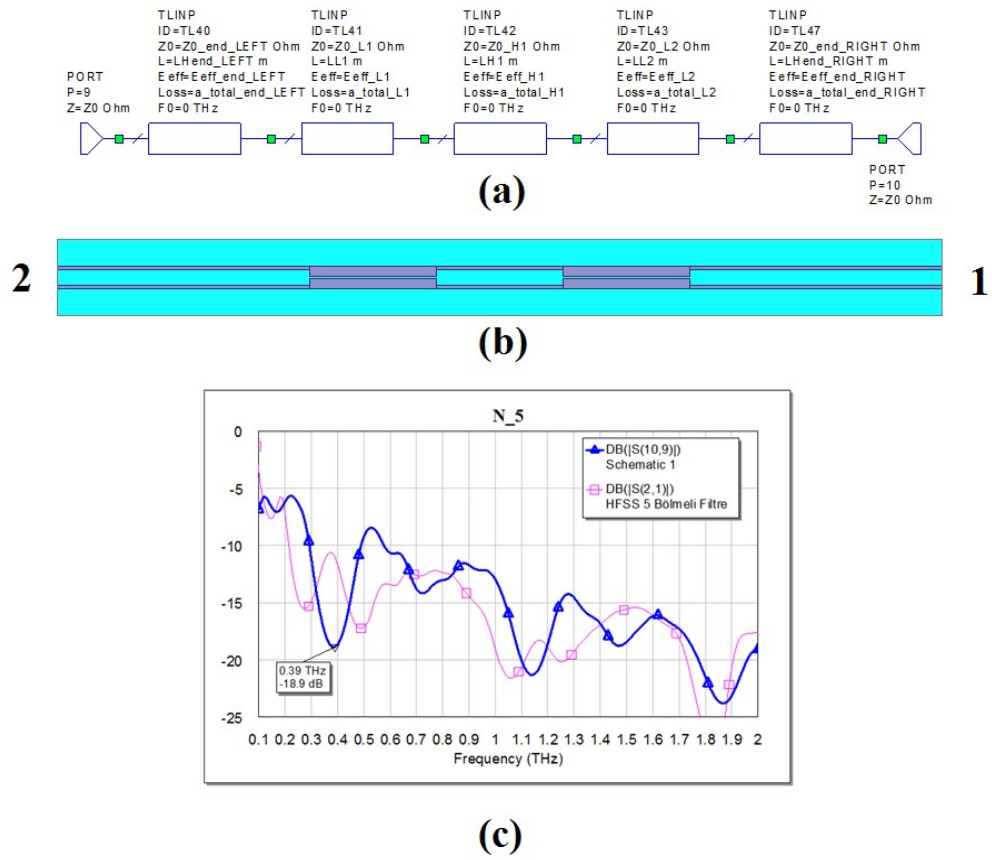
Figure 3.25 5-segment filter operating at 340GHz (a) Schematic view of the theoretically modelled filter design in AWR (b) 3D view of the structure which is used in HFSS simulations. (c) Comparison of the theoretically modelled (blue) and simulated (red) S21 parameters of the antenna.
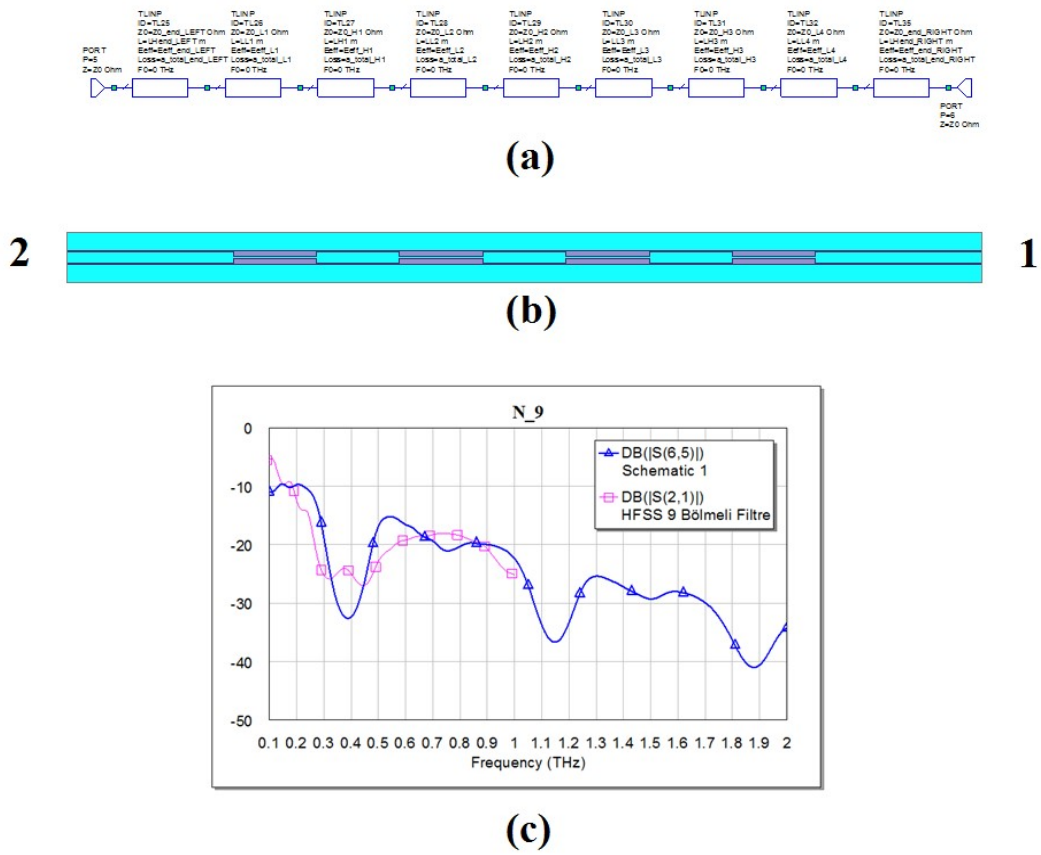
Figure 3.26 9-segment filter operating at 340GHz (a) Schematic view of the theoretically modelled filter design in AWR (b) 3D view of the structure which is used in HFSS simulations. (c) Comparison of the theoretically modelled (blue) and simulated (red) S21 parameters of the antenna.

Figure 3.27 13-segment filter operating at 340GHz (a) Schematic view of the theoretically modelled filter design in AWR (b) 3D view of the structure which is used in HFSS simulations. (c) Comparison of the theoretically modelled (blue) and simulated (red) S21 parameters of the antenna.

Addition of the designed 13–segment filter to the dipole antenna arms is shown in figure Figure 3.28.

(a)

(b)

Figure 3.28 (a) Top view of the dipole antenna derived by a 13-segment filter operating at 340GHz. (b) The antenna input resistance as a function of frequency.

3.8 Design of the Band Stop-Filter for DC Biasing at 550 GHz
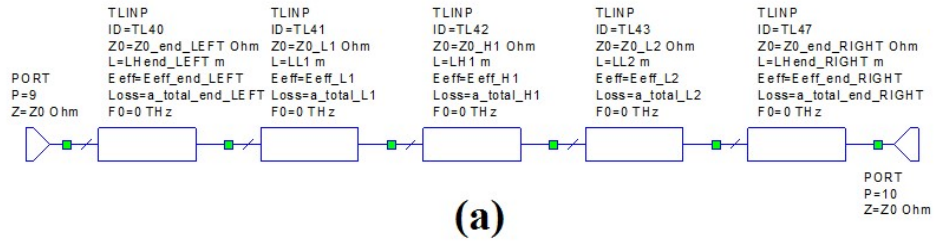
(a)
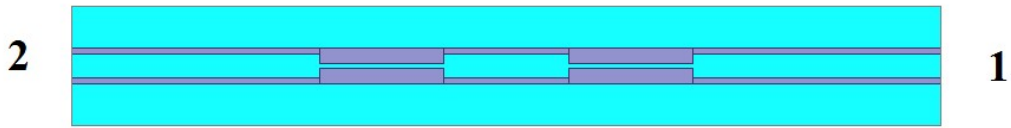
(b)
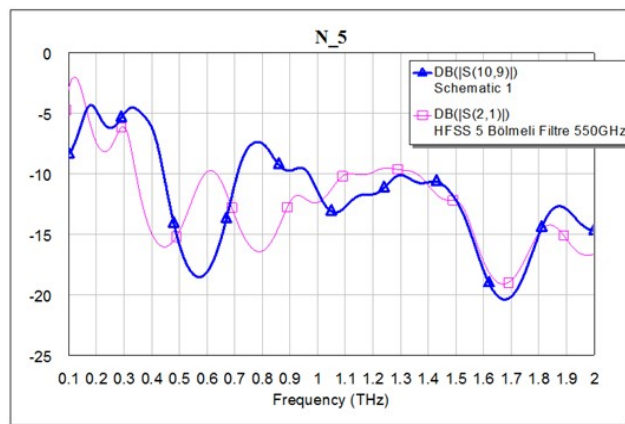
(c)

Figure 3.29 5-segment filter operating at 550GHz (a) Schematic view of the theoretically modelled filter design in AWR (b) 3D view of the structure which is used in HFSS simulations. (c) Comparison of the theoretically modelled (blue) and simulated (red) S21 parameters of the antenna.
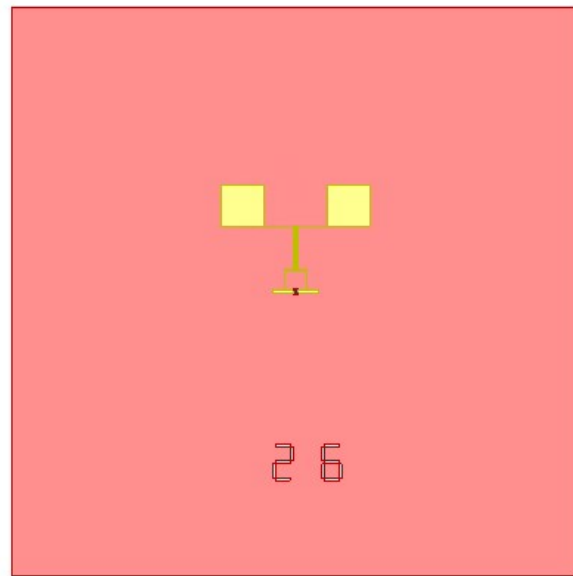
(a)
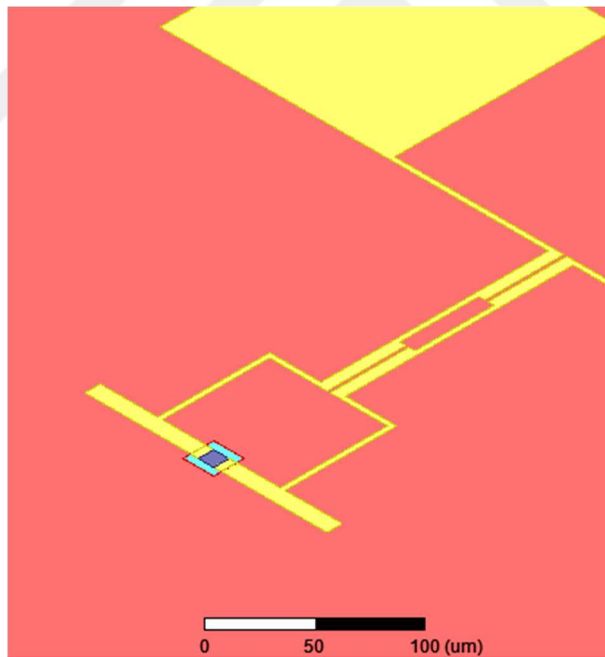
(b)

Figure 3.30 (a) Top view of the dipole antenna derived by a 5-segment filter operating at 550GHz. (b) Closer view of antenna arms.
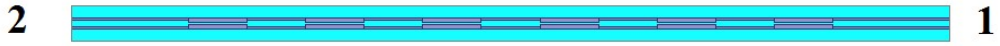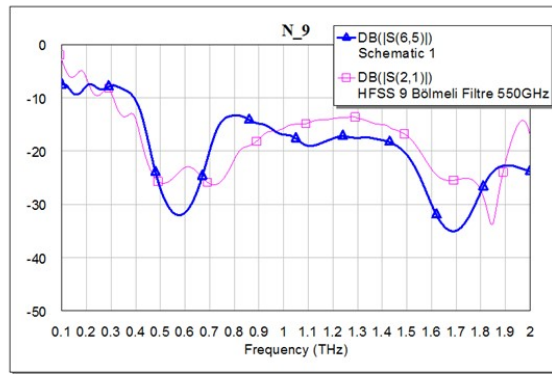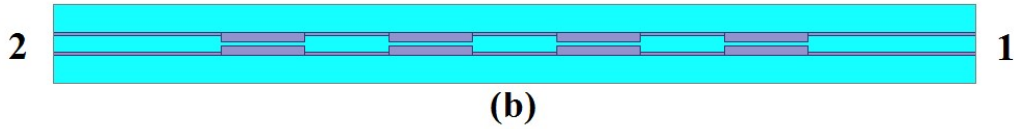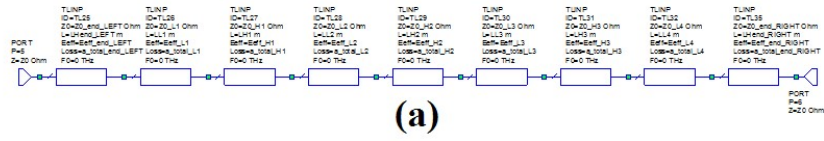
Figure 3.31 9-segment filter operating at 550GHz (a) Schematic view of the theoretically modelled filter design in AWR (b) 3D view of the structure which is used in HFSS simulations. (c) Comparison of the theoretically modelled (blue) and simulated (red) S21 parameters of the antenna.
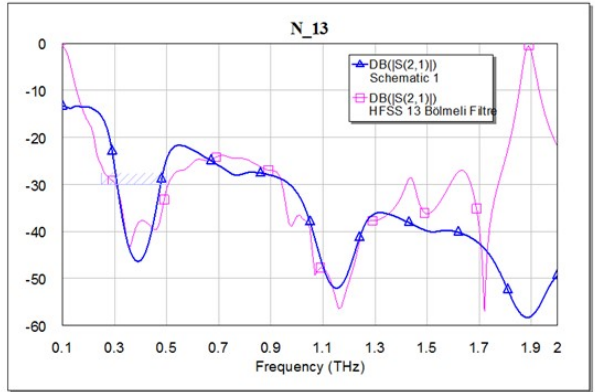
(a)
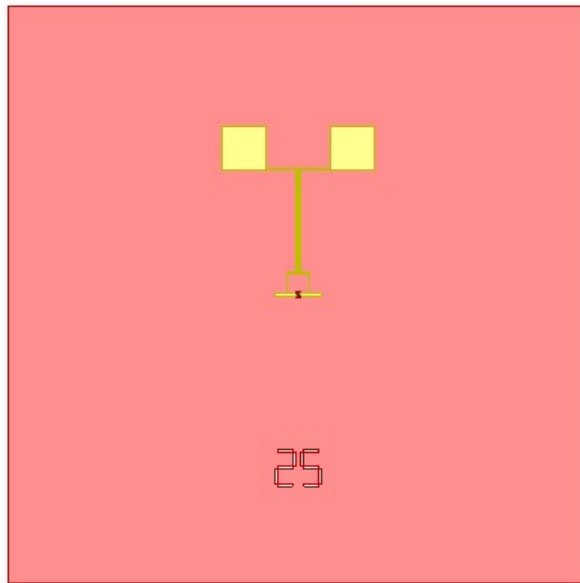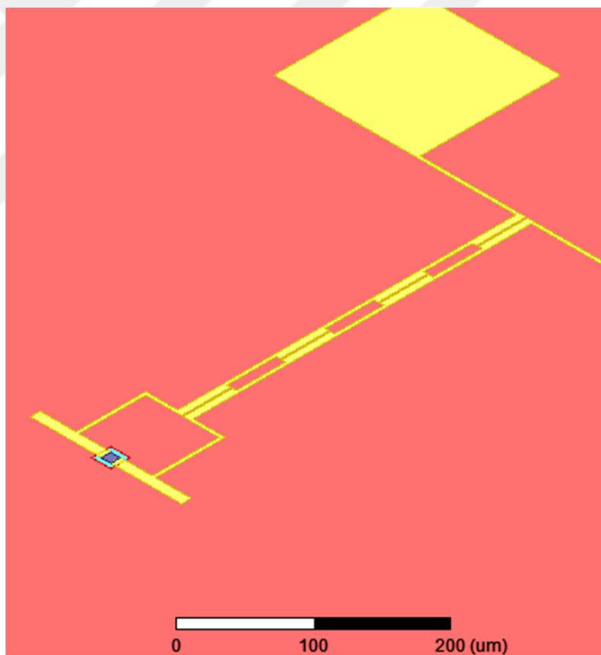
(b)

Figure 3.32 (a) Top view of the dipole antenna derived by a 9-segment filter operating at 550GHz. (b) Closer view of antenna arms.
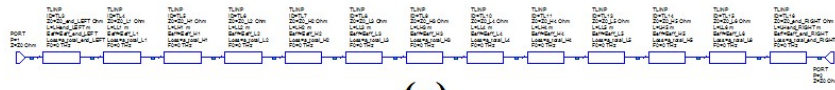
(a)
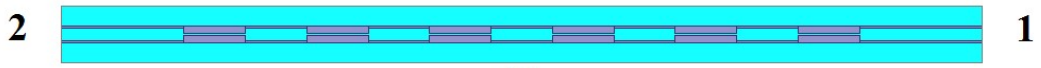
(b)
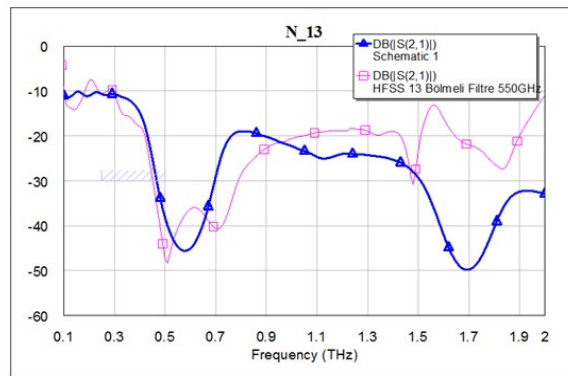
(c)

Figure 3.33 13-segment filter operating at 550GHz (a) Schematic view of the theoretically modelled filter design in AWR (b) 3D view of the structure which is used in HFSS simulations. (c) Comparison of the theoretically modelled (blue) and simulated (red) S21 parameters of the antenna.
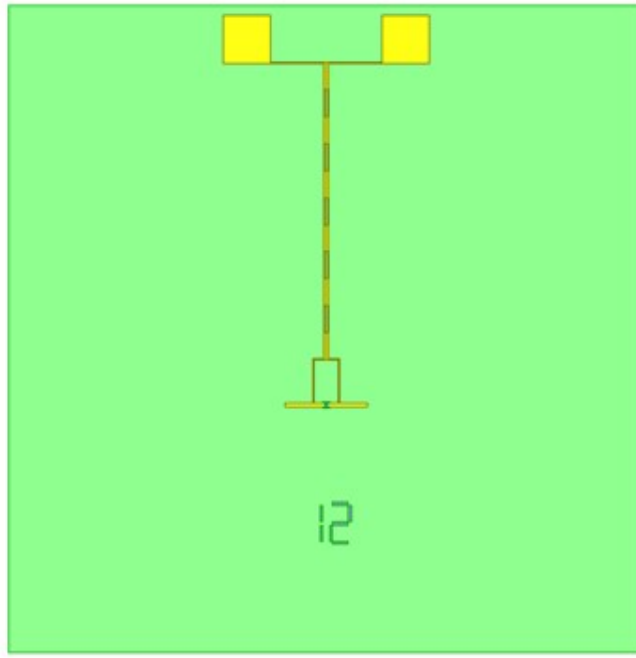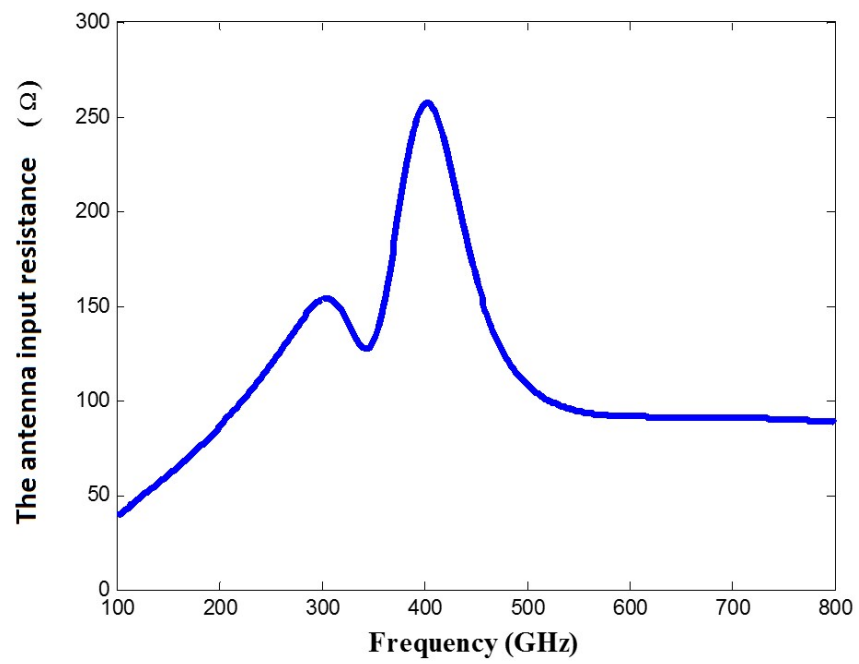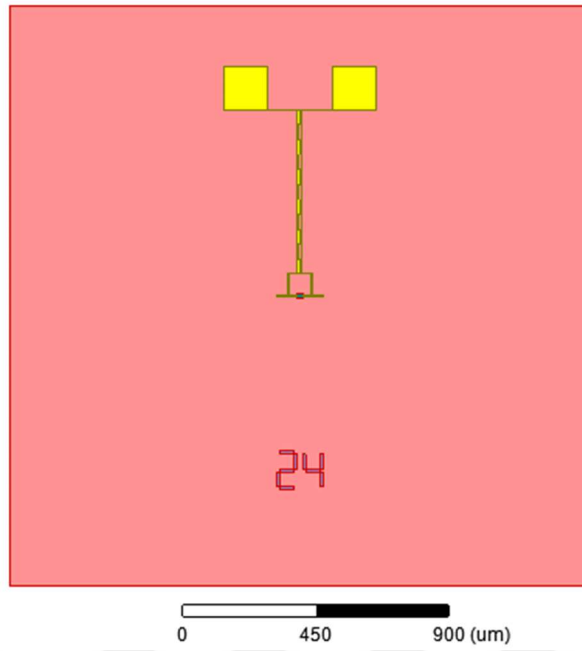
(a)
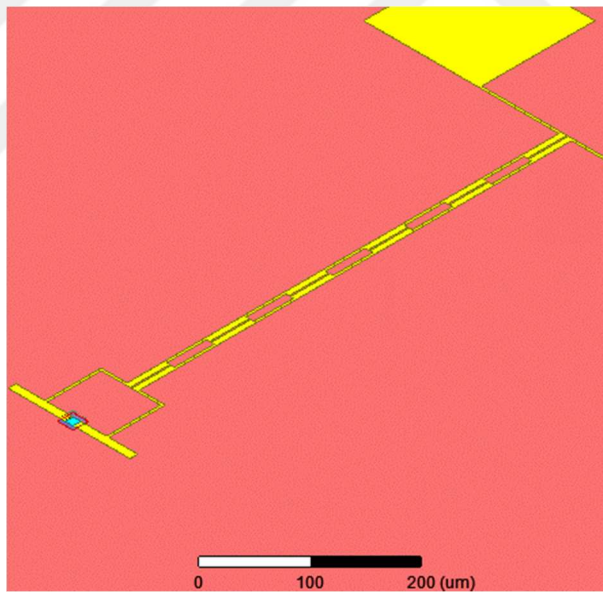
(b)

Figure 3.34 (a) Top view of the dipole antenna derived by a 13-segment filter operating at 550GHz. (b) Closer view of antenna arms.
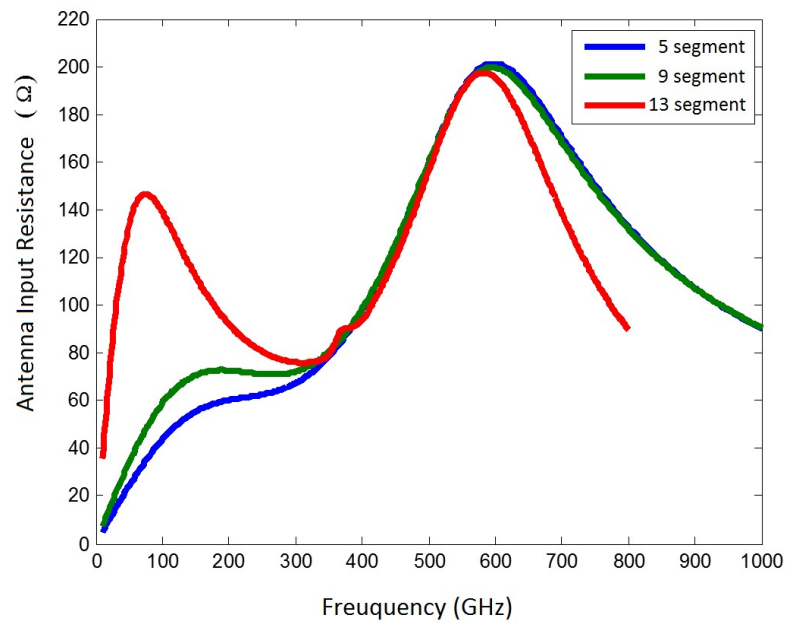
Figure 3.35 Comparison of the antenna input resistances derived by 5,9, and 13-segment filters which are operating at 550GHz.

3.9   Spiral Antenna Design

3.9.1 Spiral Antenna Deriven by the Bias Lines

The spiral antenna design given in Figure 3.36 operates at 420 GHz when it is operated as a photomixer. The input resistance of the spiral antenna is almost two times of a dipole antenna. This result makes the spiral antennas more preferable compared to the dipoles due to their low impedance mismatch between betwee the source resistance and the antenna input.

(a)   (b)

(c)
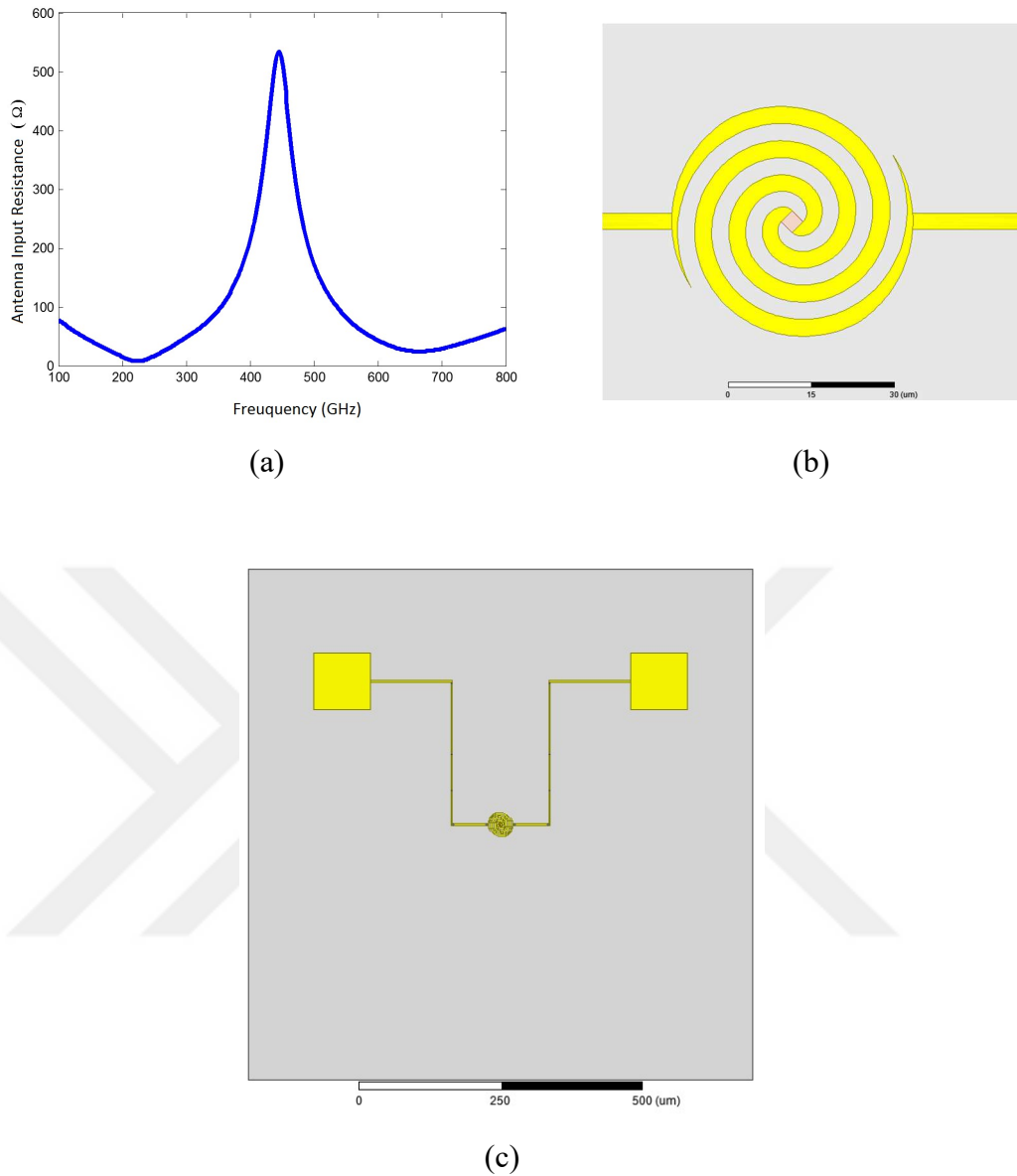
Figure 3.36 (a) Antenna input resistance as a function of frequency (b) Closer view of the spiral antenna arms (c) Top view of the spiral antenna

3.9.2. Spiral Antenna Deriven by the Filter

When the spiral antenna with a filter structure as shown in Figure 3.36 was worked as a photomixer, it made maximum radiation at around 480 GHz. The maximum resistance of the input resistance was observed to be much smaller than the one friven by the bias lines. This property of low resistance makes this antenna not that preferable due to its low mismatch to the source resistance when drived by a photomixer.

<div align="center">(a)   (b)</div>
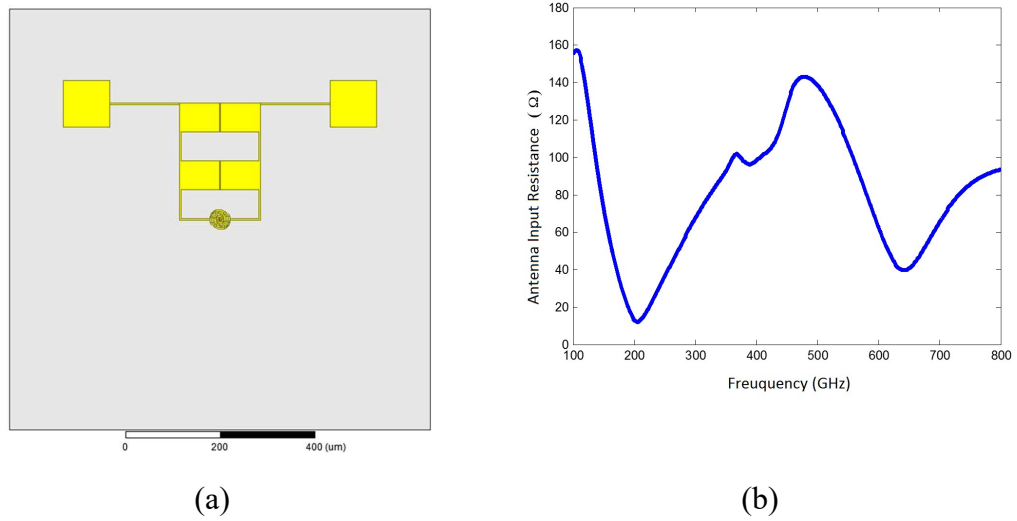
Figure 3.37 (a) Top view of the spiral antenna (b) Antenna input resistance as a function of frequency.

3.10 Design of Spiral Antenna Driven by Resistively Loaded Striplines

3.10.1 Design of Silicon Chrom Resistances

It is recorded that silicon-chrom alloy which was deposited on a substrate showed $700\ \Omega$/square sheet resistance at a thickness of $0.1\ \mu m$. Definition of surface ressitance may be extracted from the derivation by:

$$R = \rho \frac{L}{S} = \rho \frac{L}{tW} = R_s \frac{L}{W} \tag{3.25}$$

where

ρ	=	resistivity $(\Omega. cm)$
L	=	Length of the silicon-chrom layer
W	=	Wifth of the silicon-chrom layer
R_S	=	$700\ \Omega/square$, sheet resistance

With the help of the formulation given in (3.25), simulations may be performed either by using sheet resistance, R_S or bulk resistance, R. Sheet resistance is a measured quantity in the facility of clean room. The resistivity, ρ can be obtained from the sheet resistance with a known thickness of the material as follows:

$$\rho = R_S t \qquad\qquad (3.26)$$

As a result, if $0.1\ \mu m$ thick deposited material has a sheet resistance of $700\ \Omega$/square, the resistivity of the material is found as $7x10^{-5}\ \Omega m$. And this much of a reistivity corresponds to a conductivity of $\sigma = \frac{1}{\rho} = 14285.7$ S/m.

Furthermore, for the deposited materials in the form of a square shape, the sheet resistance is equal to the resistance of the material at any size in the form of a square. If the shape is a rectangle other than a square, following equality may be used to obtain the resistance of the material at that dimensions:

$$R_S = R \text{ x (aspect ratio)} \qquad\qquad (3.27)$$

To decrease the effect of the RF and DC powers on the each others, the above mentioned silicon-chrom resistances were distributed over the bias lines as shown in Figure 3.38. Here, the explanation of introducing resistances through the bias lines is that while the DC voltage source sees an open circuit due the existence of the gap at the center od the antenna, the current due to the RF power continuously flows on the bias lines and makes voltage drops on the resistances with a decreasing voltage going up to the DC source. So, the effect of the AC voltage on the DC source was expected to be very low compared to the voltage flowing on the antenna.
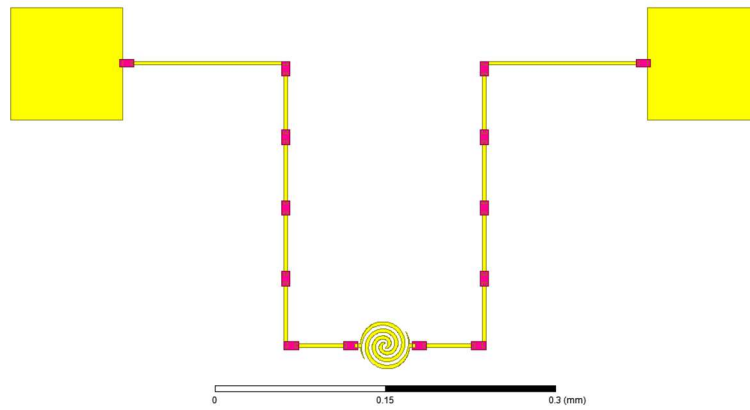
(a)
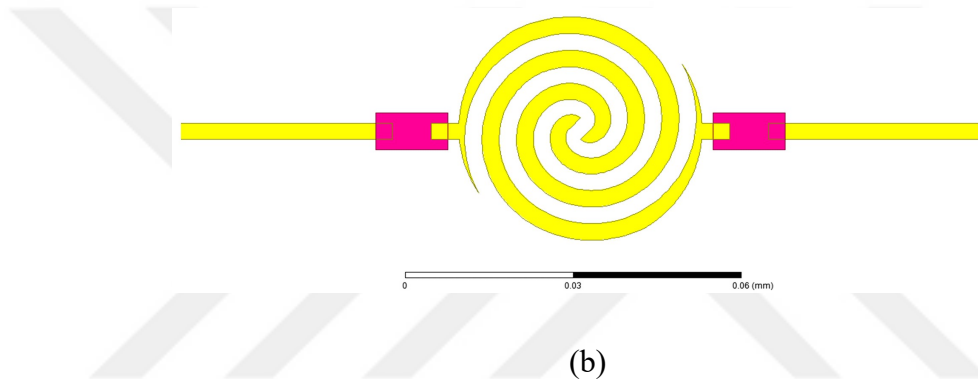
(b)
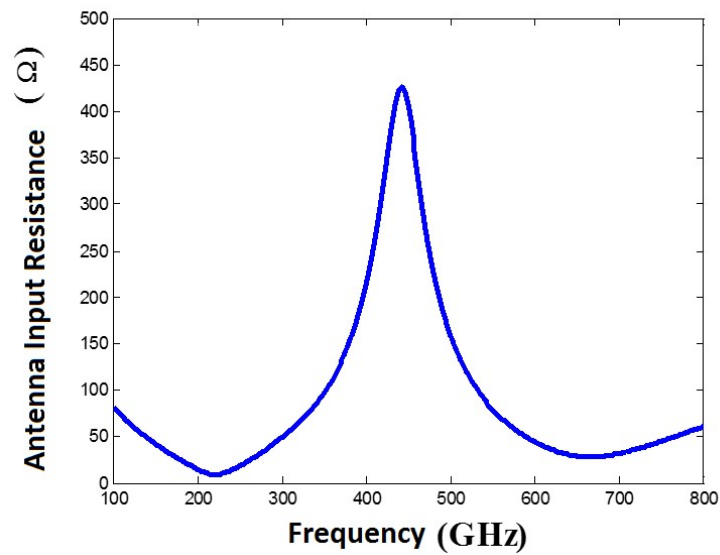
(c)

Figure 3.38 (a) Frequency dependent behaviour of the antenna input resistance. (b) Closer view of the antenna gap. (c) Top view of the spiral antenna with resistively loaded bias line.

The simulation result shows that the the spiral antenna with resistively loaded bias line makes a maximum radiation at around 450 GHz when it is woked as a phtomixer. It is noticed that maxiumum value of the antenna input resistance (440Ω) is lower than the one with bias lines (550Ω), and much higher than the one with filter (150Ω).

CHAPTER 4

RECONFIGURABLE ANTENNA DESIGN

The principle operation of a THz reconfigurable antenna is based on changing the resonance frequency of the antenna by mechanically changing the antenna size with MEMS switches. To accomplish this, two types of antenna shapes were used as reconfigurable antenna. First one is a folded dipole antenna which was designed to operate at three different frequencies by changing the antenna size by using 6 MEMS switches on each dipole arm. The second one is a simple dipole antenna operating at two different frequencies which has a single MEMS switch on each dipole arm. In this section, theoretical explanations, designs, and simulations of the reconfigurable antennas will be explained.

4.1 Design of Reconfigurable Folded Dipole Antenna

Folded dipole antennas may be preferable to simple dipole antennas. Because, they have a much higher input resistance compared to the dipoles. The current passing through the armas of a folded dipole is half of a current that passes through the arms of a simple dipole. Due to this property, if we assume that same amount of power was delivered to the arms of both antennas, the input resistance of the folded dipole should be four times of that of a dipole antenna.

$$P_{accepted} = \left(\frac{I}{2}\right)^2 R_{katlı} = IR_{dipole} \qquad (4.1)$$

(a)   (b)
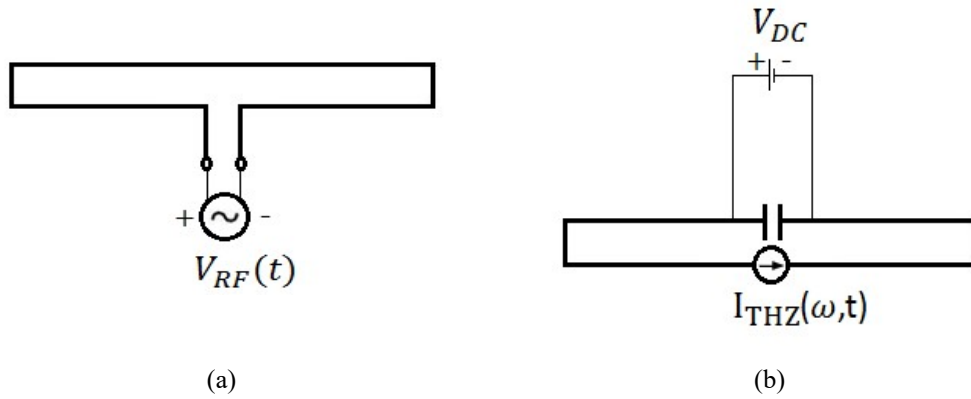
Figure 4.1 A folded dipole antenna model which is used for a classical RF-Microwave system. (b) A novel THz folded dipole antenna.

The novel folded dipole antenna model differs from a classical type dipole antenna in a way that the inclusion of a capacitor was needed to isolate the arms of the DC bias lines as shown in Figure 4.1.

4.1.1 Design of Metal-Insulator-Metal Capacitance

The impedance of the capacitor which is used as DC isolation between the dipole antenna arms should be as small a possible. To accomplish a small impedance of capacitance, the area of the capacitance shoul be large, thickness of the dielectric material between the electrode plates should be small, and a dielectric material of high dielectric constant was needed as seen in equation (4.2). Using the values given in Table 4.1, the magnitude of the capacitor impedance was found as **3.67 Ω.**

$$|Z_C| = \frac{1}{\omega C} = \frac{d}{2\pi f_{THz}\epsilon_{r,oxide}\ WL} \tag{4.2}$$

Table 4.1 Parameters of the MIM capacitor

f_{THz}	W	L	d (Oxide thickness)	ϵ_r (Oxide)	Calculated value of the capacitance	Impedance of the capacitance
340 GHz	18 μm	20 μm	100 nm	4	12.7pF	3.67 Ω

Layers of the Metal-Insulator-Metal capacitor is shown in Figure 4.2.

| (a) | (b) | (c) |
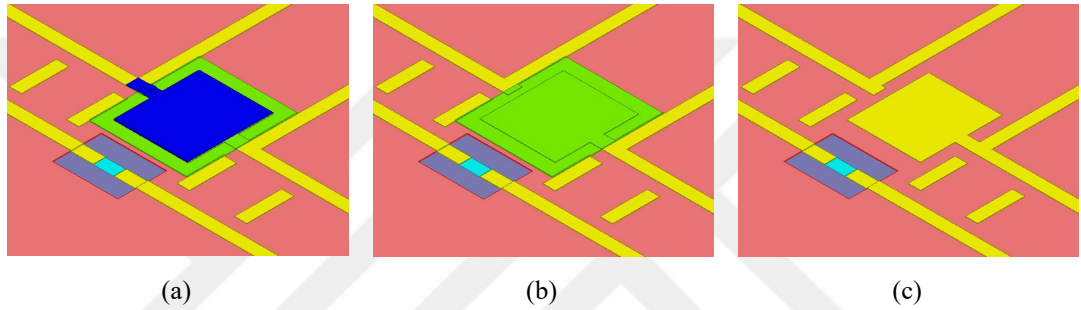
Figure 4.2 The MIM capacitor (a) top view. (b) Top metal layer (blue) was hided. (c) Oxide layer (green) hided.

In Figure 4.3, the length of the folded dipole antenna was assumed to be controlled by the MEMS switches. To pass one frequency mode to the other, a pair of MEMS switches on each arm was actuated to ON position simultaneously, which makes a total simultaneous actuation of 4 switches for each mode change.
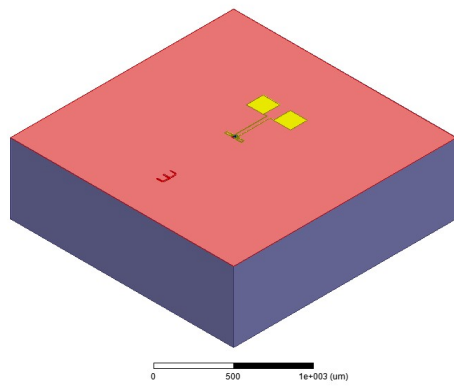
(a)
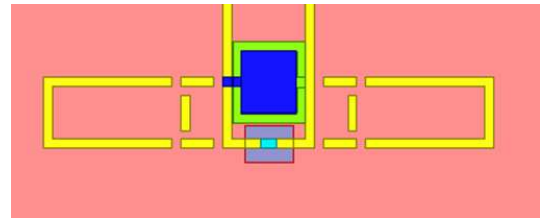
(b)
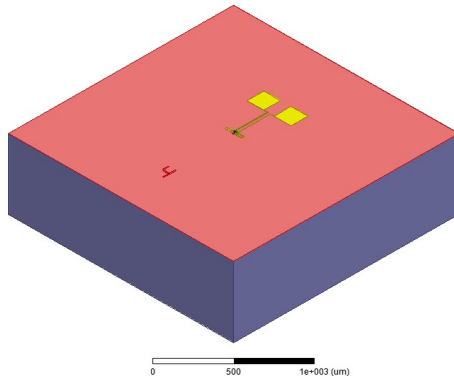
(c)
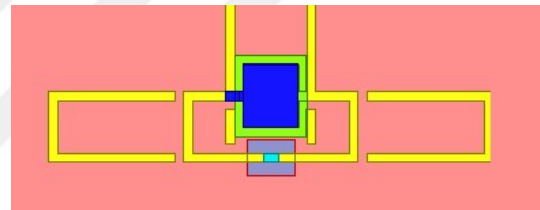
(d)
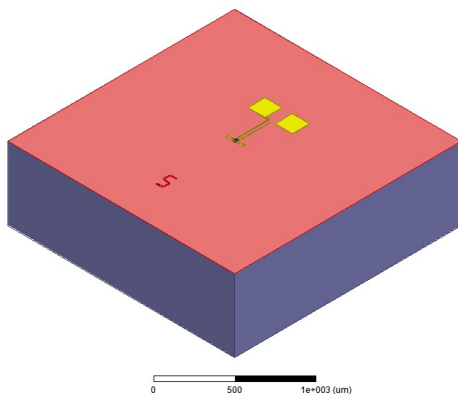
(e)
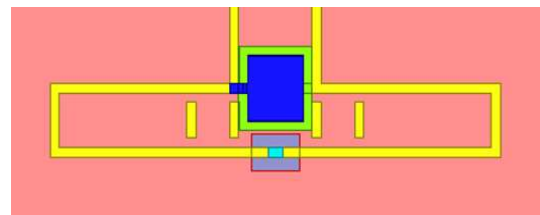
(f)

Figure 4.3 (a-b) 1ˢᵗ operational mode: Inner switch group is ON, others are OFF. (c-d) 2ⁿᵈ operational mode: Middle MEMS switch group is ON, others are OFF. (e-f) 3ʳᵈ operational mode: Outer MEMS switch group is ON, others are OFF.

105
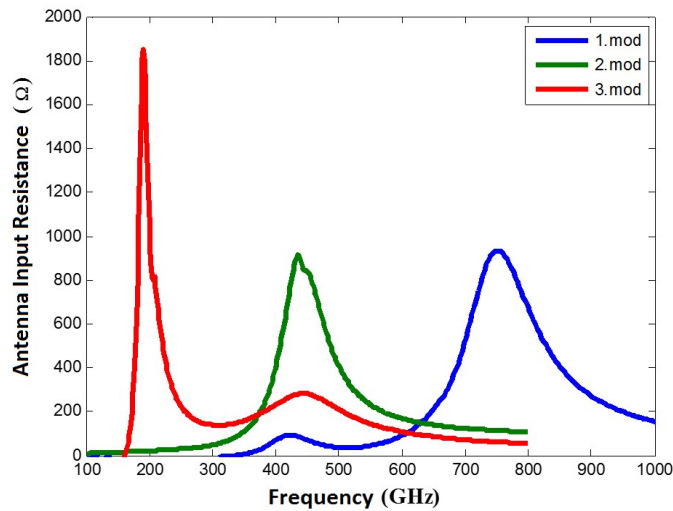
Figure 4.4 Comparison of the simulation results for three different modes of the folded dipole antenna.

Simulations results in Figure 4.4 shows that the folded dipole antenna with different MEMS switches are actuated has three different frequency mode of operations which are 200 GHz, 450 GHz, and 780 GHz. It is also noticed and verified that the resonance input resistance of a folded dipole antenna (900Ω) is almost four times that of a dipole antenna (200Ω).

4.2 Design of Reconfigurable Dipole Antenna

In Figure 4.3, the length of the dipole antenna was assumed to be controlled by the MEMS switches. There are two modes of frequency operation. To pass one frequency mode to the other, a MEMS switch on each arm was actuated to ON position simultaneously.

(a)

(b)
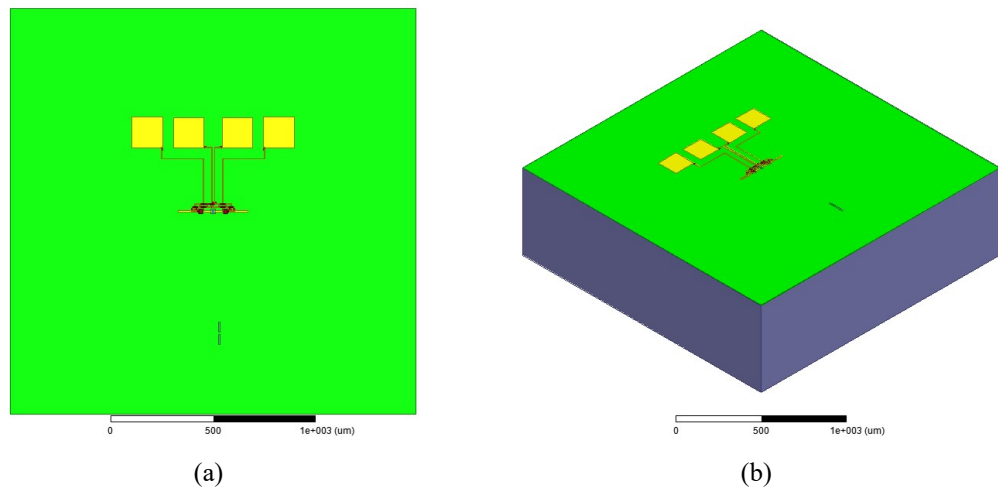
Figure 4.5 Two mode frequency reconfigurable dipole antenna (a) top view (b) side view.

(a)

(b)
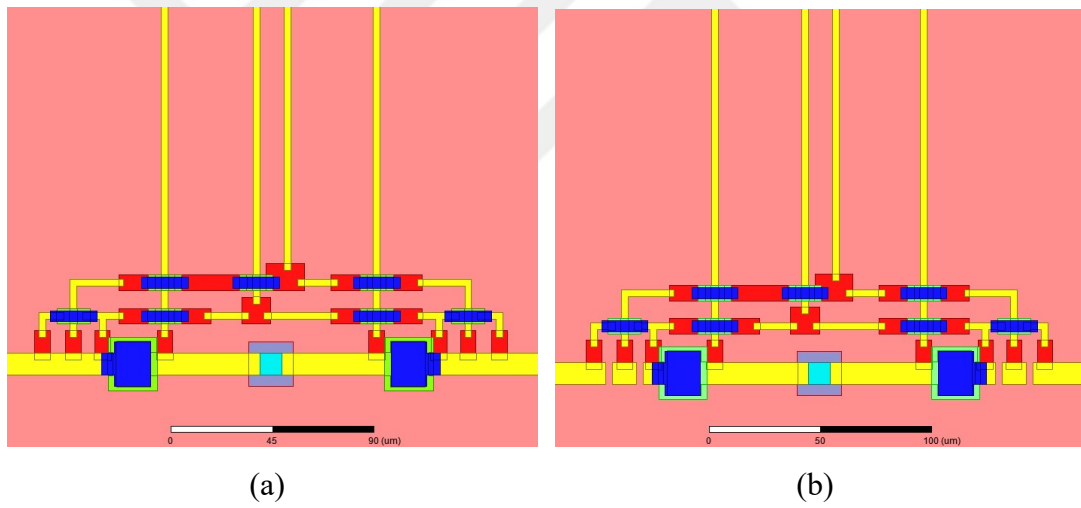
Figure 4.6 (a) 1st operational mode: MEMS swtiches are OFF. (b) 2nd operational mode: MEMS switches are ON.
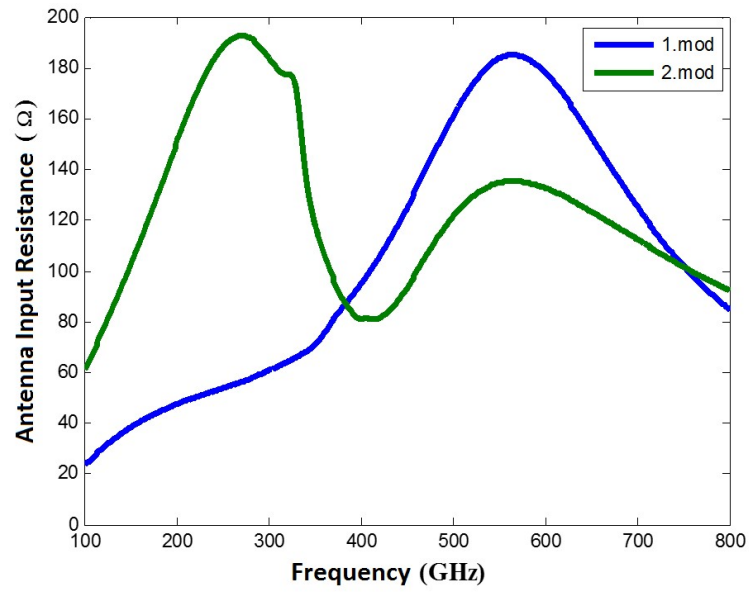
Figure 4.7 Comparison of the simulation results for two different modes of the folded dipole antenna.

Figure 4.7 shows that the reconfigurable dipole antenna has three different frequency mode of operations which are 290 GHz, 550 GHz.

CHAPTER 5

CONCLUSION

In this thesis, the terahertz photoconductive antennas have been modelled and designed for different antenna geometries.

The THz photoconductive antenna system is made up of a LT-GaAs semiconductor substrate, an antenna conductor part which is deposited on the substrate, a laser excitation system, and a DC biasing system.

Principle operation of a photoconductive antenna system is based on the conductance change at the antenna gap region due to the incident laser beam and a varying current under a DC voltage source being applied to the antenna electrodes. This current variation depends on the laser excitation type, namely pulsed or continuous wave.

The effects the various parameters on the antenna operating frequency and average source resistance have been observed.

Modelling of the photoconductive antenna includes the parameter change of laser source, semiconductor material, the antenna gap dimensions, and observing the conductance change in the antenna gap region.

After the terahertz photoconductive antenna was modeled completly, antenna gap voltage equation could have been established. Therefore, antenna gap current waveform has been calculated by using antenna parameters and antenna gap photo-excitation systems.

In the simulation results, it has been realized that the calculation of the antenna length from the wavelength calculation by using the quasi-static approach does not give a true result for the wavelength. So, an optimization should be carried out for a desired operating frequency dor the photomixers.

Finally, recongfigurable photoconductive antennas have been designed for folded dipole, and for a simple dipole antenna. Lengths of the dipole antennas is changed by

assuming MEMS switches were bridged between the two parts of the dipole each dipole arm.

As a future work, designed antennas can be fabricated and measured. Also, the MEMS switches which are responsible by gaining reconfigurability to the antennas can be designed. Then, the experimental results can be used to verify the simulation results for the designed antennas and anlyse the differences between the fabricated antennas and the simulations if any.

REFERENCES

[1] Khiabani, Neda, "*Modelling, Design and Characterisation of Terahertz Photoconductive Antennas*", Liverpool, 2013.

[2] Cheng, David Keun, "*Field and wave electromagnetics*", *New York: Addison-wesley,* cilt 2, 1989.

[3] Wilk, R., Ezdi, K., Mikulics, M., & Koch, M., "*Emission spectra of photoconductive dipole antennas: pulsed vs. photomixing operation*", Joint 31st International Conference on Infrared Millimeter Waves and 14th International Conference on Teraherz Electronics., 2006.

[4] J. Millman, "*Integrated electronics*", 2010.

[5] Khiabani, N., Huang, Y., Shen, Y. C., & Boyes, S., "*Time variant source resistance in the THz photoconductive antenna*", Antennas and Propagation Conference (LAPC), 2011 Loughborough. IEEE, pp. 1-3, 2011.

[6] K. Ezdi, M. N. Islam, Y. A. N. Reddy, C. Jördens, A. Enders, and M. Koch, "*A numerical study of photoconductive dipole antennas: the real emission frequency and an improved antenna design*", Proceeding of SPIE*, cilt 6194, pp. 61940G-61940G, 2006.

[7] Loata, Gabriel C. "*Investigation of low-temperature-grown GaAs photoconductive antennae for continuous-wave and pulsed terahertz generation*" (2007).

[8] Barkana, A., & Akgün, Ö. R., "*Basic programlama ve nümerik hesap*", Eskişehir: Bilim Teknik Yayınevi, 1983.

[9] Itoh, Tatsuo, and Raj Mittra, "*Spectral-domain approach for calculating the dispersion characteristics of microstrip lines (short papers)*», *IEEE Transactions on, 21.7,* pp. 496-499, 1973.

[10] Frankel, M. Y., Gupta, S., Valdmanis, J., & Mourou, G., "*Terahertz attenuation and dispersion characteristics of coplanar transmission lines*", Microwave Theory and Techniques, IEEE Transactions on, 39(6), pp. 910-916, 1991.

[11] C. A. Balanis, "*Antenna Theory: Analysis and Design*", THIRD EDITION, John Wiley & Sons, 2005.

[12]   "*http://www.ansys.com/Products/Simulation+Technology/Electronics/Signal+ Integri ty/ANSYS+HFSS*"

[13]   "*http://www.batop.de/products/terahertz/photoconductive-antenna/ data-sheet/manual_PCA-44-06-10-1030.pdf*"

[14] Nguyen, N. T., Sauleau, R., Perez, C. M., & Ettorre, M., "*Finite-difference time-domain simulations of the effects of air gaps in double-shell extended hemispherical lenses*" IET microwaves, antennas & propagation, 4(1), pp. 35-42, 2010.

[15] Keil, U. D., Dykaar, D. R., Levi, A. F. J., Kopf, R. F., Pfeiffer, L. N., Darack, S. B., & West, K. W. , "*High-speed coplanar transmission lines*", Quantum Electronics, IEEE Journal of, 28(10),, pp. 2333-2342, 1992.

[16] Whitaker, J. F., Sobolewski, R., Dykaar, D. R., Hsiang, T. Y., & Mourou, G., "*Propagation model for ultrafast signals on superconducting dispersive striplines*", Microwave Theory and Techniques, IEEE Transactions on, 36(2), pp. 277-285, 1988.

[17] J. Y. L. W. T. Z. D. &. B. E. R. Suen, Applied Physics Letters 96.14, "*Characterization and modeling of a terahertz photoconductive switch",* p. 141103, 2010.

[18] Y. H. Y.-c. S. a. S. B. Neda Khiabani, "*THz Photoconductive Antennas in Pulsed Systems and CW Systems*", IEEE, pp. 181-184, 2012.7

[19] C. W. a. M. J. Berry, "*Principles of impedance matching in photoconductive antennas*", Journal of Infrared, Millimeter, and Terahertz Waves, no. 33.12, pp. 1182-1189, 2012.

[20] Gonzalez, F. J., Almpanis, G., Lail, B., & Boreman, G. D., "*Wave propagation in planar antennas at THz frequencie*" IEEE, cilt 1, no. Antennas and Propagation Society International Symposium, pp. 113-116, 2004.

[21] Preu, S., Döhler, G. H., Malzer, S., Wang, L. J., & Gossard, A. C., "*Tunable, continuous-wave Terahertz photomixer sources and applications*" Journal of Applied Physics, 109(6), 061301.

[22] Khiabani, N., Huang, Y., Shen, Y. C., & Boyes, S., "*Time Varying Conductance in THz Photoconductive Antennas*" Terahertz Science and Technology, 4(3), pp. 116-122, 2011.

[23] Kiyomi Sakai, "*Terahertz optoelectronics*", Berlin: Springer, 2005.

[24] Ui Whan Kim, Seung Jae Oh, Inhee Maeng, Chul Kang, and Joo-Hiuk Son , "*Terahertz Electrical Characteristics of Heavily Doped n-GaAs Thin Films*" Journal of the Korean Phy sical So cie ty, cilt 50, no. 3, pp. 789-792, 2007.

[25] Georgiou, G., Tyagi, H. K., Mulder, P., Bauhuis, G. J., Schermer, J. J., & Rivas, J. G., "*Photo-generated THz antennas*" Scientific reports, 2014,4.

[26] Ian S. Gregory, Colin Baker, William R. Tribe, Ian V. Bradley, Michael J. Evans, Edmund H. Linfield,A. Giles Davies, and Mohamed Missous, "*Optimization of photomixers and antennas for continuous-wave terahertz emission*", Quantum Electronics, IEEE Journal of 41.5, pp. 717-728, 2005.

[27] Nuss, M. C., & Goossen, K. W., "*Investigation of high-temperature superconductors with terahertz bandwidth electrical pulses*", Quantum Electronics, IEEE Journal of, 25(12), pp. 2596-2607, 1989.

[28] Nguyen, Truong Khang, Haewook Han, and Ikmo Park, "*Highly efficient resonant antennas for terahertz photomixers*", Antenna Technology (iWAT), 2012 IEEE International Workshop on. IEEE, pp. 315-318, 2012.

[29] Jepsen, P. Uhd, Rune Hylsberg Jacobsen, and S. R. Keiding, "*Generation and detection of terahertz pulses from biased semiconductor antennas*", JOSA B 13.11, pp. 2424-2436, 1996.

[30] Nguyen, Truong Khang, Haewook Han, and Ikmo Park, "*Full-wavelength dipole antenna on a hybrid GaAs membrane and Si lens for a terahertz photomixer*", Journal of Infrared, Millimeter, and Terahertz Waves 33.3, pp. 333-347, 2012.

[31] Woo, I., Nguyen, T. K., Han, H., Lim, H., & Park, I. , "*Four-leaf-clover-shaped antenna for a THz photomixer*" Optics express 18.18, pp. 18532-18542, 2010.

[32] Hasnain, G., Whinnery, J. R., & Dienes, A., "*Dispersion of picosecond pulses in coplanar transmission lines"*, IEEE Transactions on Microwave Theory Techniques, 34, pp. 738-741, 1986.

[33] Khiabani, N., Huang, Y., & Shen, Y. C., "*Discussions on the main parameters of THz photoconductive antennas as emitters"* Antennas and Propagation (EUCAP), Proceedings of the 5th European Conference on, IEEE, pp. 462-466).

[34] Liu, L., Xu, H., Percy, R. R., Herald, D. L., Lichtenberger, A. W., Hesler, J. L., & Weikle, R. M., "*Development of integrated terahertz broadband detectors utilizing superconducting hot-electron bolometers"*, Applied Superconductivity, IEEE Transactions on, 19(3), no. 282-286, 2009.

[35] Brown, E. R., F. W. Smith, and K. A. McIntosh, "*Coherent millimeter‐wave generation by heterodyne conversion in low‐temperature‐grown GaAs photoconductors"* Journal of Applied Physics 73.3, pp. 1480-1484, 1993.

[36] Zhang, Jitao, "*Characterization of the terahertz photoconductive antenna by three-dimensional finite-difference time-domain method*", arXiv preprint arXiv:1406.3872 , 2014.

[37] Němec, H., Pashkin, A., Kužel, P., Khazan, M., Schnüll, S., & Wilke, I., "*Carrier dynamics in low-temperature grown GaAs studied by terahertz emission spectroscopy*" Journal of Applied Physics, 90(3), pp. 1303-1306, 2001.

[38] Duffy, S. M., Verghese, S., McIntosh, K. A., Jackson, A., Gossard, A. C., & Matsuura, S., "*Accurate modeling of dual dipole and slot elements used with photomixers for coherent terahertz output power"* Microwave Theory and Techniques, IEEE Transactions on, 49(6), pp. 1032-1038, 2001.

[39] Berry, Christopher William, "*Plasmonic Photoconductors for Higher Performance Terahertz Radiation Sources*", (Doctoral dissertation, University of Michigan, 2013.

CURRICULUM VITAE

Personal Information

Surname, Name	DEMİR, Kazım
Date of birth	01.01.1991
Place of birth	Ankara/TURKEY
Nationality	Turkish (T.C.)
Current Position	*Researcher,* Yıldırım Beyazit University, Ankara, TURKEY
Phone	+090 506 693 0961
Home address	Batı Sitesi Mah. Cengiz Aytmatov Cad. Altın Konut Sitesi No:51 Yenimahalle/ANKARA

Education

2013 - 2016	**M.Sc** Yıldırım Beyazıt University, Electrical and Electronics Engineering, Ankara/TURKEY (GPA: 3.85 / 4)
2008 - 2013	**B.Sc** Gaziantep University, Electrical and Electronics Engineering, Gaziantep/TURKEY (GPA: 2.66 / 4)
2004 – 2008	**HS** Batıkent Foreign Language Intensive High School, Ankara/TURKEY (GPA: 85.04 / 100)

Work Experience

Nov. 2015 -	*Researcher,* UNAM, Bilkent University, Ankara/TURKEY
Apr. 2015 -	*Researcher,* METU MEMS Laboratory, Ankara/TURKEY
Mar. 2013- Jun. 2013	*Intern engineer*, SANKO SÜPER FİLM, Gaziantep/TURKEY

Summer 2012	*Intern*, ASELSAN, Microwave Hybrid Module Production Laboratory
Summer 2011	*Intern,* Turkish Radio and Television Corporation, Headquarters of the TV and Radio Transmitters
Summer 2010	OSTİM Organized Industrial Zone, ELMAKSAN DATA Tasarım Limited company.

Kazım DEMİR

Department of Electrical and Electronics Engineering

2016 ANKARA